REACTION SITES IN AC ELECTRO-SLAG REMELTING

A STUDY OF REACTION SITES IN AC ELECTRO-SLAG REMELTING

by

DEBABRATA S. GHOSH, B.Tech.

A Thesis
Submitted to the School of Graduate Studies
in Partial Fulfilment of the Requirements
for the Degree
Master of Engineering

McMaster University
September, 1972

MASTER OF ENGINEERING (1972)
(Metallurgy and Materials Science)

McMASTER UNIVERSITY
Hamilton, Ontario

TITLE: A Study of Reaction Sites in AC Electro-Slag Remelting

AUTHOR: Debabrata S. Ghosh, B.Tech. (Indian Institute of Technology, Bombay)

SUPERVISOR: Dr. D. A. R. Kay

NUMBER OF PAGES: xii, 149

ABSTRACT

The dominant slag-metal reaction site in AC electro-slag remelting (ESR) has been directly determined by estimating the rate of sulphur transfer at the electrode tip/slag and metal pool/slag interfaces. In this investigation, negligible sulphur transfer has been assumed at the droplet/slag interface, and the basis for such assumption is discussed. Using a 5.825" diameter mould and CaF_2-CaO slags, it has been established that the electrode tip/slag interface is the dominant reaction site. Calculations indicate that the pool sulphur is close to equilibrium with the slag. The importance of all six reaction sites in AC ESR are discussed. The results indicate the importance of the slag/atmosphere interface, especially when using slags of low lime content. Conventional overall sulphur balances have been carried out and the results are in agreement with the rates obtained at the different interfaces, thus indicating internal consistancy of the results.

ACKNOWLEDGEMENTS

The author wishes to express his gratitude to Dr. D.A.R. Kay for his interest and guidance during the course of this study. The author is also grateful to Drs. C. K. Cooper and R. J. Pomfret for many invaluable discussions and suggestions during this project.

Grateful acknowledgements are due to the members of staff and graduate students of the Department of Metallurgy and Materials Science at McMaster University for many helpful suggestions. Special thanks are due to Miss Lydea de Jong for fast and accurate typing of this thesis.

TABLE OF CONTENTS

FIGURES

LIST OF FIGURES

LIST OF TABLES

CHAPTER I

INTRODUCTION

The advent of the aerospace age created a great demand for materials with exceptional mechanical properties and a high degree of reliability under critical service conditions. Conventional melting and casting techniques could guarantee neither the chemical and structural homogeneity of the ingot nor the necessary compositional tolerances. Various special steelmaking techniques, such as vacuum degassing, vacuum arc remelting (VAR), electro-slag remelting (ESR), electron beam remelting and plasma arc remelting were developed to make high quality alloy steels meeting the stringent specifications of the consumers. Of these techniques, ESR is one of the most versatile, since it brings about not only a marked improvement in structure but also a considerable amount of chemical refinement (if required).

Electro-slag refining in its present form, was essentially developed in the U.S.S.R.(1) during the 1950's, although a previous U.S. patent exists(2). It has been many years now since extensive research in the U.S.S.R.(1) proved that ESR is a very efficient and commercially feasible technique for making high quality material. Since then, work elsewhere(3-13) has firmly established the superiority of ESR over most of the other special steelmaking techniques. In fact, ESR ingots have generally been found to exhibit better mechanical properties than ingots remelted by VAR(1,11,13,14), which is extensively used in the U.S . ESR is also found to be economically more favourable than VAR(11,14).

Despite these factors, there has been a great reluctance in the West, especially in North America, in accepting ESR. Duckworth and Hoyle(13) might have put their finger on the right place when they stated that one of the obstacles to the widespread use of ESR is the semantic reluctance of engineers to the acceptance of any process in which the word "slag" is used. To engineers, "slag" generally has the connotation of the word "dirty".

Obviously, the presence of this active slag gives rise to all the differences between VAR and ESR. As pointed out by Duckworth and Wooding(14 a larger number of degrees of freedom are available to ESR as compared to VAR due to this slag. A required amount of refining can be obtained during ESR by an appropriate choice of slag composition, while the electrode composition in VAR must be essentially the same as the desired ingot composition.

Desulphurization is one of the most important reactions in ESR. CaF_2-based ESR slags, containing varying amounts of lime, have been found to be very efficient desulphurizers. In fact, they have better desulphurizing abilities than most of the normal steelmaking slags. This is probably due to the higher activity of lime found in these slags(15,16,17).

Metal desulphurization is obviously taking place at the following three slag-metal interfaces: the electrode/slag, the droplet/slag, and the ingot pool/slag. Sulphur analysis of the ingot gives an idea of the total desulphurization taking place, but gives no indication of where most of the reaction is taking place.

In DC ESR electrolytic sulphur transfer occurs in opposite directions at the electrode tip and metal pool/slag interfaces. Hence, an indication of the dominant reaction site in ESR can be obtained indirectly by comparing the results of the two DC modes of melting. The results of earlier workers(1,18,19,12) from small scale ESR rigs indicated that the metal pool was the dominant site while the results from large scale rigs(20,12) indicated just the opposite. This apparent contradiction in DC ESR has been explained by Holzgruber et al.(12) on the basis of differences in current densities and overpotentials in the two cases.

The main aim of this project is to determine directly the dominant reaction site in ESR. Slags in the binary CaF_2-CaO system have been chosen for this study since the thermochemistry of this system is fairly well established(15,16,17,21,22,23).

CHAPTER II

ESR SLAGS

2.1 Introduction

All the major differences between vacuum arc remelting (VAR) and electro-slag remelting (ESR) can be attributed to the presence of an active slag in ESR. As indicated by Duckworth and Wooding(14) the presence of this slag is the principal reason for a much greater number of degrees of freedom available to ESR, as compared to VAR, in terms of power requirements, type and shape of moulds, ingot properties, etc.

The two most important functions of the slag are: (i) it is the main source of heat, and (ii) it is the principal means of control of chemical composition. The slag also has a number of minor functions. A thin layer of slag freezes on to the mould wall, insulating the ingot electrically and thermally from the mould. This results in a greater degree of axial solidification and shallower metal pools in ESR as compared to VAR. Consequently, superior mechanical properties of the ingot are obtained with ESR. According to some authors,(1,24,25,13) the solidified slag skin also helps to promote a smooth ingot surface. The slag protects the molten metal from direct atmospheric oxidation and provides a heat reservoir above the molten metal which prevents piping and internal shrinkage during the final stages of solidification.

Hence, the prime requirements of fluxes used in ESR are a high electrical conductivity in the molten state, an appropriate chemical reactivity, chemical stability at high temperatures, and a low volatility at operating temperatures. For these reasons, slags in CaF_2-based systems, which also have the desired surface tension and viscosity properties, are generally chosen in the remelting of iron and nickel-based alloys.

Some authors contend that the liquidus of the slag must be below that of the alloy melted(13,24,7); otherwise the electrode would tend to melt back out of the slag. The fact that slag bath temperatures as high as 1800°C are quite common in melting ferrous alloys would indicate fallacies in the above argument. In fact, Russian workers(26) have successfully melted copper through a slag with a liquidus of 1350°C. Hence, this is not a prime requirement for ESR slags, although it has been generally used in industry as a rule of thumb for successful melting.

Therefore, a single slag composition must necessarily be a compromise between the above requirements. Calcium fluoride has been found to be a good base for ESR slags to which oxides such as CaO, MgO, etc., have been added to increase the chemical reactivity, especially desulphurizing ability, of the slag. Alumina has been commonly added to ESR slags to increase its resistivity and to give a good ingot surface finish. Thus, the CaF_2-CaO-Al_2O_3 system is most important one as far as remelting ferrous alloys are concerned.

But, in this investigation the simple binary CaF_2-CaO system was chosen to avoid complicated chemical interactions. Also, as mentioned in the last chapter, the chemistry of this system is better documented

(15,16,17,21,22,23) than most of the other ESR slag systems.

In this chapter, the properties of ESR slags have been reviewed with particular emphasis on the CaF_2-CaO system. However, no extensive or exhaustive literature survey is attempted since fairly good reviews(4,13,27,28) are already available.

2.2 Some Physical Properties of Selected Slags

2.2.1 Electrical Conductivity

The electrical conductivity of ESR slag is a primary factor in determining the process heat generation, although some variations in the distribution of heat generation can be obtained by changes in voltage, current and slag volume. Calcium fluoride was mainly chosen due to its high conductivity and stability at ESR temperatures, although it should be borne in mind that too high a conductivity can lower the efficiency of heat generation in the furnace. For reasons that will become clear later, alumina is a good addition to the slag in such cases.

The conductivities of calcium fluoride based slags with additions of CaO and/or Al_2O_3 have been determined by various authors(29-36). The available results are reviewed by Duckworth(13) and Mitchell(36). Considerable variations in the results of different authors can be seen and the reasons for such discrepancies are indicated by Mitchell(36). However, same trends have been observed by all the authors for lime or alumina additions to CaF_2. Replacement of CaF_2 by lime lowers the conductivity by a small extent while additions of alumina greatly reduce the conductivity of the slag.

Further discussions on slag conductivity are given in Section 5.12, along with the comparison of conductivity values reported in the literature with those obtained from this investigation.

2.2.2 Vapour Pressure

Slag bath temperatures of 1700°C are quite common in ESR and hence the components of the slag must have low vapour pressures at these temperatures.

Vapour pressure data of selected fluorides and oxides are summarized in reference (13). Among the highly conductive fluorides, CaF_2 is found to be the least volatile, and, being the least poisonous fluoride, it is chosen as an ESR flux. Most of the oxides, except those of the alkali metals, have lower vapour pressure than CaF_2 and hence their loss from slags is unimportant compared to that of CaF_2.

At about 1500°C very small weight losses by volatilization from different CaF_2-based ESR slags were observed by various authors(16,23,27). They report around 1% to 3% weight loss from slag melts, larger losses being observed from slags rich in CaF_2(16). At higher temperatures (near 1700°C), much larger slag losses are expected and hence losses between 5% and 10% could be quite common during actual ESR melts.

2.2.3 Viscosity

Some authors(13,38) believe that the viscosity of the slag can affect reaction rates indirectly by influencing parameters such as the velocity of circulating slag flow, the terminal velocity of molten droplet, etc. Indeed, viscosity could be related to the reaction rate through its inter-relation with diffusion rates.

Except for the work of Davies and Wright(38), most of the viscosity determinations of ESR slags are found in the Russian literature(1,39-44). Viscosities in CaF_2-CaO-Al_2O_3 system in the temperature range liquidus-1550°C have been obtained by Davies and Wright(38) by a rotating-crucible method. They found very low viscosity values which lie in the centipoise range. They also observed no significant change in slag viscosity with additions of CaO and Al_2O_3, either singly or in combination. It is thought(13) that viscosity is dependent on the degree of superheat. Although this could be partially true, no such correlation was found by Davies and Wright(38). They tried to determine the liquidus temperature from the changes in the slopes of the log (viscosity) vs. 1/T curves. In the case of the CaF_2-CaO system, their observations are in line with the findings of Kor and Richardson(16) and H. Yuan-Sun et al(15) while they disagree with the phase diagrams of Mukerji(45) and Budnikov et al(46). Their liquidus temperatures were generally higher than given by phase diagrams.

Binary and ternary phase diagrams in the system CaF_2-CaO-Al_2O_3 were also plotted from the viscosity measurements by Zhmoidin(66).

Three ternary eutectics were found in the above system.

2.2.4 Surface and Interfacial Tension

As indicated by Kay and Pomfret(28), the absorption of inclusions by slag is governed by the various interfacial energies between the inclusion, metal and slag. Also, interfacial tensions and the shape of the electrocapillary curve may determine the nature of the electrocapillary vibration during AC ESR. The electrocapillary curve also relates the interfacial tension to the surface excess concentrations of ionic species, which may determine the local rate of transfer at the slag-metal interface.

Unfortunately, very few surface or interfacial tension data for ESR slags are reported in the literature(41,48-53). The surface energy of CaF_2 determined by Kulifeev et al.(51) is given by the relationship:

$$\sigma_{CaF_2} = 303.7 - 0.033\ T \qquad (2.1)$$

Pupynina et al.(53) determined interfacial tensions between molten Armco iron and CaF_2-based slags between 1873 and 2073°K. Interfacial tensions were found to be practically independent of slag composition and changed only slightly with temperature. On the other hand, Evseev(54), measuring surface tension by a maximum bubble pressure method, found that it increased with the addition of CaO while no changes were observed with the addition of Al_2O_3. Further studies are required before a clear picture of interfacial tension of ESR slags can emerge.

2.2.5 Density and Heat Capacity

A large density difference between metal and slag may be desirable in ESR since it enhances phase separation and hence reduces the possibility of slag entrapment in the solidifying metal. Duckworth and Hoyle(13) postulate that the larger the density difference, the smaller the size of metal droplets and hence, probably, the faster the refining rate. No evidence has been given to substantiate the postulated increase in refining rate, and it may be refuted by the argument that very little reaction takes place in the drop during its quick transition through the slag(9). Duckworth and Hoyle also state, however, that larger density differences imply higher terminal drop velocities, resulting in shorter reaction times.

Densities of slags are, however, useful in calculations of slag volume from the weight of slag charged. Such calculations were required during this investigation. An adequate review of the literature is given in reference (13).

The heat capacities of the slag and metal are parameters which determine, inter alia, the heat balance of the process. The heat capacity of the slag also determines its effectiveness as a heat reservoir for hot-topping purposes at the end of the melt. From specific heat, C_p, and latent heat of transformation data, Duckworth and Hoyle(13) calculated the energy required to raise one ton of iron and

0.05 tons of CaF_2 from room temperature (298°K) to 2000°K to be 452.3 kWh ton^{-1}. On commercial ESR plants the average energy consumption is reported as 1200 kWh ton^{-1}, giving a process efficiency of about 38%.

2.3 Phase Equilibria of Selected ESR Slags

2.3.1 CaF_2

In spite of the apparently simple nature of the slag systems based on CaF_2, there exists quite large discrepancies in the literature concerning the phase diagrams in these systems. It is generally believed(16,45,13,28,37,55) that these discrepancies arise from the reaction of CaF_2 with water vapour:

$$(CaF_2) + H_2O_{(g)} = (CaO) + 2HF_{(g)} \tag{2.2}$$

As much as 0.5 - 2% CaO can be formed by the above reaction in pure CaF_2 which can reduce the melting point considerably. In fact, various melting points of "pure" CaF_2 have been reported in the literature:

1386°C	Eitel(56)
1390°C	Budnikov and Tresvyatskii(46)
1402°C	Porter and Brown(57)
1418°C	Kelley(58), Baak(29), Naylor(59)
1419°C	Mukerji(45)
1420°C	Bååk and Ölander(60), Gutt and Osborne(61)
1423°C	Masson et al.(62)

Masson et al's(62) value for the melting point of CaF_2 is accepted as the "best" value since they purified the molten CaF_2 by passing HF through the melt for 2 to 4 hours. From the free energy data of reaction (2.2) they estimated the amount of lime in their final CaF_2 to be approximately 10 ppm on a molar basis.

Hence, the difficulties in the determination of phase diagrams for CaF_2 based slags can be appreciated. CaF_2 is also known to react with SiO_2 giving volatile SiF_4:

$$2(CaF_2) + (SiO_2) = SiF_{4(g)} + 2(CaO) \qquad (2.3)$$

which makes the determination of the CaF_2-SiO_2 system almost impossible(63), although one study of the binary has been reported(64).

2.3.2 CaF_2-CaO

There exists considerable differences in the phase diagrams of this system published by different authors. The earlier work of Eitel(56) indicates a simple eutectic around 18% CaF_2 and 1360°C. However, his reported value of 1386°C as the melting point of CaF_2 would indicate the use of an impure variety of CaF_2. Baak(29) used conductivity measurements to investigate the phase equilibria in this system and reported a miscibility gap between 0.8 mole % and 10 mole % CaO, with a maximum at about 92.5 mole % CaF_2 and 1485°C. The phase diagrams of both Baak and Eitel are shown in Figure 2.1. Budnikov and Tresvyatskii(46) who studied this system both by the method of deformation of cones and by differential thermal analysis, did not find the miscibility gap reported by Baak, although the activity measurements of Yuan Sun et al.(15) agree with Baak's results.

Fairly recent work by Mukerji(45) using differential thermal analysis, and Kojima and Masson(65) using a depression of freezing point method, do not show the presence of the two liquid region indicated above. Their results are shown in Figures 2.2 and 2.3. It can be seen that their results are in good agreement, although the liquidus values of Masson et al.(65) are 4 to 10°C higher than those of Mukerji(45) due to the use of purer CaF_2. Mukerji's(45) eutectic is seen (Figure 2.2) to be at 1360°C and 19.5% CaO.

Hence, the phase diagrams of all the authors do include a eutectic, although the shape of the liquidus on the CaO-rich side is in dispute. Results of Kor and Richardson(16), Davies et al.(22), and Edmunds et al.(17) are in very good agreement and lead to a liquidus composition at 1500°C of 23 wt.% CaO. This gives a value of approximately 27 mole % CaO at 1450°C in good agreement with the results of Yuan-Sun et al(15) and Eitel(56); it contradicts the phase diagrams of Mukerji(45) and Budnikov et al.(46), both of whom found much higher CaO contents at saturation.

Figure 2.1 also includes the CaO-rich liquidus line obtained from the results of Kor and Richardson(16). The presently accepted phase diagram of the CaF_2-CaO system, constructed mainly from the data presented above, is reported by Davies(28) and is shown in Figure 2.4.

2.3.3 CaF_2-Fe_tO and CaF_2-CaO-Fe_tO

These systems are related to the present investigation due to the fact that no attempts were made in this study to prevent air oxidation of the electrode, and therefore the presence of iron oxide in the slags was inevitable.

The phase equilibria of the binary system CaF_2-Fe_tO, where Fe_tO represents total iron in the slag expressed as stoichiometric FeO, was determined by Oelson and Maetz(66) and is given in Figure 2.5. The extensive miscibility gap, shown in the above figure, indicates a large positive deviation from identity in this system. The activities of ferrous oxide $a_{"FeO"}$ referred to the standard state of non-stoichiometric ferrous oxide "FeO" in equilibrium with iron at that temperature were obtained from the above phase diagram at 1450°C(21) and are plotted in Figure 2.6. Hence, it can be seen from Figure 2.6 that even small amounts of iron oxide introduced in the slag during remelting can lead to high oxygen potentials in CaF_2-Fe_tO slags. Since sulphur removal can be considered to take place by an exchange reaction with oxygen (see equation (3. 6), the FeO content of the slag is an important parameter in this study.

Recent investigations(21,67) indicate large activity coefficients for iron oxide in these systems which are found to decrease with addition of CaO. This agrees quite well with the ternary phase diagram of the system CaF_2-CaO-Fe_tO (see Figure 2.7) given by Oelsen and Maetz(66). The size of two liquid region decreases with increasing additions of CaO, 25% CaO being sufficient to close the miscibility gap at 1400°C.

2.3.4 Other Systems of Interest to ESR

Since alumina is a common addition to the slags used in remelting ferrous alloys, the systems CaF_2-Al_2O_3 and CaF_2-CaO-Al_2O_3 are technologically very important. Pascal(68) reports a eutectic in the system CaF_2-Al_2O_3 at 1270°C and 27 wt.% Al_2O_3, while Kuo and Yen(69) found the eutectic composition to be 9 wt.% Al_2O_3, although a very similar eutectic temperature of 1290°C was reported. This disagreement may arise from the presence of unknown amounts of CaO in the system formed by reactions such as (2.2) or by the reaction:

$$3(CaF_2) + (Al_2O_3) = 2AlF_{3(g)} + 3(CaO) \tag{2.4}$$

To resolve this discrepancy Mitchell and Burel(70) determined phase equilibria in this system by obtaining cooling curves for different CaF_2-Al_2O_3 melts. Their results along with those of previous workers(68,69) are shown in Figure 2.8. They obtained a eutectic at 10 wt.% Al_2O_3 and 1368°C. Thus, their eutectic composition essentially agrees with that of Kuo and Yen(69), although their temperature was about 80°C higher. Since Kuo and Yen derived their diagram from the X-ray analysis of quenched melts, this discrepancy is not unexpected.

The only investigation of the important ternary system CaF_2-CaO-Al_2O_3 appears to be that of Eitel(56) who studied the system CaF_2-CaO-$5CaO.3Al_2O_3$. On the basis of this and the pertinent binary diagrams, a tentative ternary diagram in this system is proposed by Duckworth and Hoyle(13). Lack of sufficient data in this system is unfortunate since as indicated in reference (13) most of the industrial slags fall in this class. However, in recent experiments to determine sulphur capacities, Kor and Richardson(16) have delineated the CaO saturation boundary in this system at 1500°C.

The ternary phase diagram of another industrially important system, CaF_2-MgO-Al_2O_3, is tentatively proposed by Duckworth and Hoyle(13) from the different binary diagrams. Lime is sometimes replaced by magnesia in ESR slags to prevent moisture pick up by highly hygroscopic lime, but the high liquidus temperatures of magnesia bearing slags reduce their widespread application.

Silica can be intentionally added to ESR slags, or found as a result of oxidation of silicon from the metal by the slag. According to Ol'shanskii(63) determination of the CaF_2-SiO_2 phase diagram is made impossible by the reaction:

$$2(CaF_2) + (SiO_2) = SiF_{4(g)} + 2(CaO) \qquad (2.3)$$

although one study(64) has been reported without any mention of SiF_4 formation.

Pseudobinaries in the system CaF_2-CaO-SiO_2 have been studied by many authors(45,56,60,66,71) from which ternary phase diagrams have been proposed(45,72,73).

The system CaF_2-Ca may be important if the mechanism of current transport through the slag as proposed by Whittaker(19) were true. Whittaker proposed that during DC ESR the calcium, which is deposited at the cathode, is subsequently transported to the anode for regeneration of calcium fluoride or oxide. Ca has been shown$^{(74)}$ to be completely miscible with CaF_2 above its melting point, indicating the possibility of the above mechanism, although free calcium has never been found in any form in the slag after AC or DC remelting$^{(19,75)}$.

In the present investigation slags were prefused in a graphite crucible before use and hence, phase equilibria in the CaF_2-CaC_2 system may be important. According to Mitchell$^{(76)}$ it is a simple eutectic system with the eutectic at 14 mole % CaC_2 and 1240°C. Positive deviations from ideality were, therefore, observed and Raoultian activity coefficients around 8 - 10 are reported for CaC_2 at 1500°C$^{(76)}$.

2.4 Activities of Components in Selected ESR Slags

2.4.1 CaF_2-CaO

Yuan-Sun et al.$^{(15)}$ studied the activity of lime in CaF_2 melts by equilibrating flowing mixtures of HF and H_2O with slag samples. Knowing the p_{HF}/p_{H_2O} ratios and the standard free energy change for the reaction:

$$(CaF_2) + H_2O_{(g)} = (CaO) + 2HF_{(g)} \tag{2.5}$$

at 1450°C, the ratios a_{CaO}/a_{CaF_2} were obtained. Integration of a modified Gibbs-Duhem equation permitted the calculation of separate activities of lime and calcium fluoride. Their results are given in

Figure 2.9. It contains a flat region corresponding to the miscibility gap proposed by Baak(29) which disagrees with CaF_2-CaO phase diagrams proposed by other workers(45,56,65).

During their sulphur capacity measurements, Kor and Richardson(16) obtained CaO-saturated liquidus lines from the changes in slope of sulphur capacity vs. composition plots. The results are plotted in Figure 2.1.

Assuming that the CaF_2-CaO system behaves in a similar manner to the system PbF_2-PbO, studied by Jeffes and Sridhar(77), Kor and Richardson calculated the CaO activity from their above results, knowing the heat of fusion and the melting point of CaO. The activities of CaO and CaF_2 thus obtained at 1500°C are given in Figure 2.10. It must be noted that the activities reported in Figure 2.10 are relative to pure liquids (and not solids). Results for the PbF_2-PbO system are also included. A slight deviation from Temkin ideality in this system can be seen. In contrast to Yuan-Sun et al.(15) no liquid miscibility gap is predicted.

Recently CaO activities in CaF_2 melts have been determined(17) by studying the equilibrium:

$$(CaO) + 3C_{(s)} = (CaC_2) + CO_{(g)} \tag{2.6}$$

The results of Edmunds and Taylor(17) are given in Figure 2.11. In one respect there is good agreement between the three sets of workers, namely the composition of the lime liquidus at 1500°C. All three place this at between 0.26 and 0.3 mole fraction CaO which differs considerably from the phase diagrams of Mukerji(45) and Budnikov(46). However, their data agrees with the phase diagram reported by Eitel(56).

Figure 2.12 gives the activity plot of the three sets of authors. The data of Yuan-Sun et al is not considered to be very reliable.

2.4.2 CaF_2-Fe_tO and CaF_2-CaO-Fe_tO

Activities of ferrous oxide, $a_{"FeO"}$, referred to the standard state of non-stoichiometric ferrous oxide in equilibrium with iron at that temperature, were obtained in CaF_2-FeO and CaF_2-CaO-FeO melts by Kay et al.(21) and Hawkins and Davies(67). In addition, Hawkins and Davies(67) also investigated the effect of the addition of Al_2O_3 on $a_{"FeO"}$ in the quaternary system CaF_2-CaO-Al_2O_3-"FeO". The activities of ferrous oxide, $a_{"FeO"}$, in both investigations were determined by studying the equilibrium:

$$Fe_{(s)} + CO_{2(g)} = ("FeO") + CO_{(g)} \tag{2.7}$$

in iron crucibles with known CO/CO_2 atmospheres in the temperature range 1410° - 1500°C. Results obtained for both the investigations in the CaF_2-FeO system is shown in Figure 2.13. Large positive deviations from ideal (Temkin) behaviour were observed which is in line with the large miscibility gap of Oelson and Maetz(66) (Figure 2.5). There does exist a discrepancy in the actual values obtained by the two sets of workers (Figure 2.13), those of Kay et al.(21) being somewhat higher than those of Hawkins and Davies(67). The reasons for the discrepancy are not clear, particulary since the same experimental method was used. However, experimental difficulties, such as loss of slag by "creep" from the crucible, separation of metallic iron from the slag, etc., reduce the accuracy of the results.

The large positive deviations from ideal behaviour in this system arise from the differences in interaction energies between the various pairs of ions. When these interaction energies are zero, random mixing takes place and Temkin ideal behaviour is exhibited. Following the model suggested by Flood, Forland and Grjotheim(78), Davies(28) has calculated the activity of ferrous oxide in this system and the results are also included in Figure 2.13. The experimental activities can be seen to be much lower than those predicted by the Flood model. The deviations are probably due to the breakdown of the random mixing assumption.

Activities of FeO in the ternary system CaF_2-CaO-Fe_tO at 1450°C are given in Figure 2.14(67). The CaO-saturated liquidus line was obtained from the changes of slope in a_{FeO} vs. composition plots. Also shown in this figure is the boundary of the two liquid region of Oelsen and Maetz at 1400°C.

2.4.3 Other Systems of Interest to ESR

The CaF_2-MnO system has been studied at 1500° and 1600°C by Smith and Davies(37) who found very large positive deviations from Temkin ideality just as in the case of the CaF_2-FeO system. Their results are shown in Figure 2.15.

Since the FeO-MnO system behaves ideally, the results obtained for the CaF_2-MnO system are similar to those discussed in Section 2.4.2 for CaF_2-FeO systems. Smith and Davies also studied the effect of additions of CaO and Al_2O_3 to CaF_2-MnO slags. An orthogonal plot of the ternary CaF_2-CaO-MnO showing liquidus and a_{MnO} values at 1500°C is given in Figure 2.18(37). The addition of MnO to the CaF_2-Al_2O_3 system creates a large miscibility gap.

Activities in the industrially important CaF_2-CaO-Al_2O_3 system have been recently determined by Edmunds and Taylor(17) by the technique described in Section 2.4.1. Their results are shown as isolime-activity curves in Figure 2.17. Small negative deviations from ideal Raoultian behaviour were observed.

The CaF_2-CaO-SiO_2 system was studied by Yuan-Sun et al.(15) by the method described in Section 2.4.1 above. Their results are not considered very reliable although good agreement with phase diagrams of Baak(73) is obtained. Silica activities in this system were also determined(23) by studying the equilibrium:

$$(SiO_2) + 3C_{(s)} = SiC_{(s)} + 2CO_{(g)} \qquad (2.8)$$

Silica activities obtained from this reaction by Sommerville and Kay(23) at 1450°C did not agree very well with those of Yuan-Sun(15). Lime activities in this system were also calculated using a Gibbs-Duhem relationship for ternary systems.

CHAPTER III

ESR REACTIONS AND REACTION SITES

3.1 ESR Reactions

3.1.1 Introduction

An understanding of slag/metal reactions during ESR is essential to the control of final ingot composition. By a proper choice of slag components, refining reactions such as desulphurization, dephosphorization, oxide inclusion removal, etc., are achieved under laboratory and industrial conditions. During ESR it is quite usual to experience losses of certain essential alloying elements, particularly easily oxidizable elements such as Al, Ti, Si, Mn and Cr. A knowledge of the chemical properties of ESR slags is, therefore, important in minimizing such losses. The most important chemical reactions taking place during ESR are discussed below.

3.1.2 The Oxygen Reaction

Reduction in the oxygen and oxide inclusion content of the ingot especially during AC ESR(1,4,47,79,80,81), is generally achieved through a proper choice of slag and melting conditions. It is believed that oxygen is removed by one or a combination of the following mechanisms:

(i) mechanical flotation of inclusions in the metal pool with subsequent absorption by the slag, (ii) dissolution of inclusions in the molten metal at the electrode tip followed by chemical reaction with the slag, (iii) electrochemical reaction, especially during DC ESR.

A simple flotation mechanism for inclusion removal was proposed in early works(1,82) and in later reviews(7,83). Inclusions which have terminal velocities greater than the velocity of the solidification front are assumed to float out in the metal pool. Using Stoke's Law, the minimum size of alumino-silicate inclusions that can be removed is about 10 μm in diameter(47). Subsequent absorption of an inclusion by the slag depends on the interfacial energies between the inclusion, metal and slag. It has been reported(84) that the majority of inclusions are removed at the electrode tip. Thus, it has been proposed(47,85,86) that, due to high local temperatures, ∿ 1800° - 2000°C, inclusions dissolve at the electrode tip by reactions of the type:

$$(SiO_2)_{incl} = [Si] + 2[O] \tag{3.1}$$

Subsequent removal of oxygen and silicon takes place by the reaction:

$$[Si] + 2[O] = (SiO_2)_{slag} \tag{3.2}$$

Experimental evidence of the above mechanism is presented(47) in the form of photomicrographs of electrode tips. Calculations based on a model show that, at tip temperatures of 2000°C, 20 μm diameter silica and 4 μm diameter alumina inclusions can dissolve completely within one second(47).

Reactive alloying elements can be lost from the metal by oxidation reactions of the type:

$$x\,[M] + y\,[O] = (M_xO_y)_{slag} \tag{3.3}$$

From the Ellingham diagram for oxides, the descending order of reactivity of elements with oxygen at ESR temperatures is:

Al, Mg, Ti, Si, Mn, Cr, Fe, Ni

This is also the observed order of loss of alloying elements(13) during ESR. Equation (3.3) also determines the level of oxygen in the metal. For example, if the activity of an oxide with a small negative free energy of formation, such as FeO or MnO, is high, then the oxygen content of the metal in equilibrium with this oxide will be high too. Thus, for low metal oxygen levels and small losses of alloying elements, only the oxides with equilibrium constants for reaction (3.3) greater than 10^{15} (such as CaO, ZrO_2, Al_2O_3, MgO, TiO_2, etc.) have been found suitable as slag components. The presence of FeO in slag is unavoidable in air melts due to oxidation of the electrode. The large values of the activity coefficient of FeO in CaF_2 melts (see Section 2.4.2) along with the low equilibrium constant for the reaction:

$$[Fe] + [O] = (FeO)_{slag} \tag{3.4}$$

can give rise to large oxygen levels in the metal with consequent losses of alloying elements. This can be reduced by melting under an inert atmosphere such as argon or by addition of a slag deoxidizer such as Al or Ti.

The oxygen content of the ingot has also been found to depend on the type and mode of melting, i.e., AC, DC electrode +ve or DC electrode -ve(1,11,12,19), and on the ingot diameter(12). In DC remelting this suggests that some oxygen is transferred across the slag-metal interface by cathodic reaction:

$$[O] + 2e^- \rightarrow (O^{2-}) \qquad (3.5)$$

the reverse reaction taking place at the anode. These reactions are obviously taking place at different rates resulting in a net increase or decrease of oxygen in the metal.

3.1.3 The Sulphur Reaction

Sulphur, being present in steels in the form of sulphides which are highly soluble in liquid iron, cannot be removed by a simple flotation mechanism. The solution of sulphide inclusions in the electrode tip(87) indicates that sulphur removal in ESR can only take place by the following mechanisms: (i) chemical reactions at the slag-metal interfaces controlled by localized concentrations, temperatures, and the time and extent of contact between the slag and the metal, (ii) electrolytic reactions controlled mainly by the interfacial potential drop.

The effect of slag basicity and oxygen potential on sulphur removal during ESR(1,4,19,79,87) suggests that the transfer takes place by the conventional exchange reaction:

$$[S]_{1\ wt.\%} + (O^{2-}) = (S^{2-}) + [O]_{1\ wt.\%} \tag{3.6}$$

for which the equilibrium constant is given by:

$$K_6 = \frac{a_{(S^{2-})}\ h_{[O]}}{h_{[S]}\ a_{(O^{2-})}} \tag{3.7}$$

thus:

$$\frac{a_{(S^{2-})}}{h_{[S]}} = K_6 \quad \frac{a_{(O^{2-})}}{h_{[O]}} \tag{3.8}$$

Hence, from equation (3.8), it can be predicted that desulphurization will be improved by increasing the basicity of the slag (i.e., $a_{(O^{2-})}$) and by reducing the metal oxygen content, $h_{[O]}$, which is related to the oxygen potential of the slag (see Section 3.1.2). This is exactly the trend found in ESR by the authors referred to above.

Also, just as in the case of oxygen, it is found that desulphurization during DC ESR depends on the polarity of the electrode(1,11,12,18,19), indicating that some sulphur is transferred by the cathodic reaction:

$$[S] + 2e^{-} = (S^{2-}) \tag{3.9}$$

and by the reverse anodic reaction at the other electrode. As each unit volume of the metal goes through both the reaction sites, the net sulphur transfer depends on which of the two sites is the dominant one. A discussion of the dominant reaction sites is given in detail in

Section 5.10 below.

Kor and Richardson(16), and Hawkins et al.(55) studied the equilibrium:

$$(O^{2-}) + 1/2\ S_{2(g)} = (S^{2-}) + 1/2\ O_{2(g)} \tag{3.10}$$

in CaF_2 based slags at 1500°C. The values of (wt.% S) $p_{O_2}^{1/2} / p_{S_2}^{1/2}$, obtained for each slag by equilibrating with varying ratios of $p_{O_2}^{1/2}$ and $p_{S_2}^{1/2}$, are extrapolated back to zero (wt.% S) to give the sulphur capacity, C_s, i.e.,

$$C_s = (\text{wt.\% S})\ (p_{O_2}/p_{S_2})^{1/2}_{(\text{wt.\%S})\to 0} \tag{3.11}$$

Sulphur capacities of various CaF_2 based slags are reported(16,22,55). For reaction (3.10):

$$K_{10} = \frac{a_{(S^{2-})} \cdot p_{O_2}^{1/2}}{a_{(O^{2-})} \cdot p_{S_2}^{1/2}} \tag{3.12}$$

Assuming that dilute solution of sulphur in the slag obey Henry's Law, we have from the above definition of C_s and equation (3.12):

$$C_s = K' \ \cdot a_{(O^{2-})} \tag{3.13}$$

which means that for a particular slag composition (i.e., for particular $a_{(O^{2-})}$) the sulphur capacity of the slag is fixed for any particular temperature. Sulphur capacity values are useful in choosing the proper slag composition for adequate desulphurization. The equilibrium values of metal sulphur concentration can be predicted by knowing the slag sulphur content, the metal oxygen content, and the sulphur capacity of the slag, as shown in Section 5.8.

Different authors(1,11,19, 79, 87,88,89) have suggested that in ESR, sulphur can be oxidized from the slag by the reaction:

$$(S^{2-}) + \frac{3}{2} O_{2(g)} = SO_{2(g)} + (O^{2-}) \tag{3.14}$$

This effect is discussed further in Section 5.10.2.

3.1.4 The Phosphorus Reactions

The classic equation for dephosphorization is written as:

$$2[P] + 5[O] + 3(O^{2-}) = 2(PO_4{}^{3-}) \tag{3.15}$$

for which:

$$K_{15} = \frac{a^2_{(PO_4{}^{3-})}}{a^2_{[P]} \cdot a^5_{[O]} \cdot a^3_{(O^{2-})}} \tag{3.16}$$

and hence the phosphorus partition coefficient can be given by the relationship:

$$\frac{a_{(PO_4{}^{3-})}}{a_{[P]}} = \text{Const.} \times a^{5/2}_{[O]} \times a^{3/2}_{(O^{2-})} \tag{3.17}$$

Hence a high slag oxygen potential and a high basicity are required to promote good dephosphorization. The requirement of a highly oxidizing slag is one of the reasons why dephosphorization is not practiced in ESR since the resulting ingot is found to be "dirty"(3). As much as 25% FeO had to be added to a CaF_2 slag before a reasonable amount of phosphorus(3) could be removed. Consequently, a "dirty" ingot with a high inclusion rating was obtained.

A discharge of complex (PO_4^{3-}) ions at the ingot pool is indicated during DC negative electrode remelting, by the results of Whittaker(19). He obtained better dephosporization with DC electrode +ve than with DC electrode -ve, thus showing the electrolytic aspects of P transfer.

3.1.5 The Carbon Reaction

Except for a slight increase in metal carbon content(13) carbon plays no part during ESR. Carbon is probably picked up from CaC_2 in the slag which is formed by the reaction:

$$(CaO) + 3C_{(s)} \rightarrow (CaC_2) + CO_{(g)} \qquad (3.18)$$

during slag pre-fusion in a graphite crucible.

3.1.6 The Hydrogen Reaction

One of the chief disadvantages of ESR is that unlike the VAR process it does not remove substantial quantities of hydrogen. In fact, unless reasonable precautions are taken, hydrogen can be readily increased resulting in ingot porosity or ingot cracking.

Forno et al.(47) have determined the effects of several melting parameters on the hydrogen reaction in a small-scale ESR rig. When using only calcium fluoride slag with a dry argon atmosphere, only a slight increase in hydrogen is observed during AC remelting. On incorporation of calcium oxide and alumina into the slag, high hydrogen contents in the metal are obtained irrespective of the atmosphere. There seems to be little doubt that the source of hydrogen in the experiments is hydrated calcium oxide. The hydrogen is produced probably by reduction of moisture in the slag by hot metal:

$$[\mathrm{Fe}] + (\mathrm{H_2O}) \rightleftarrows (\mathrm{FeO}) + 2[\mathrm{H}] \qquad (3.19)$$

In order to investigate the electrolytic aspects of the hydrogen reaction, DC melts with different electrode polarities were performed. In general, the hydrogen levels in DC melts were found to be much lower. The lowest hydrogen pick-ups were observed when melting under a dry atmosphere and with ingot-positive polarities.

It was observed that AC remelting following a DC start also gave low hydrogen contents, suggesting that DC starting either removed hydrogen from the slag or produced a "getter" which was subsequently effective in keeping hydrogen at a low level. If the latter were true, subsequent DC remelting may be irrelevant to the low hydrogen levels. Therefore, some runs with AC arc starting followed by DC remelting were made and low hydrogen levels were still obtained, suggesting that it is indeed associated with electrolytic action in the use of DC.

The lasting effect on the hydrogen content of a DC start on subsequent AC remelting suggested that the hydrogen getter was produced during the DC arcing period. Calcium or aluminum metal could be produced but addition of these metals during AC did not lead to low hydrogen contents. Another possibility was that iron oxides were formed in the initial arcing. Additions of ferric oxide during AC remelting lead to low hydrogen contents. In addition, oxides of copper and chromium are very effective, but these elements are picked up in the final ingot. The effect of slag additives is presumably due to reactions of the type:

$$(Fe^{3+}) + [H] \rightleftarrows (Fe^{2+}) + [H^{+}] \tag{3.20}$$

$$(Fe^{2+}) + 2[H] \rightleftarrows [Fe] + 2(H^{+}) \tag{3.21}$$

3.2 ESR Reaction Sites

As stated above, one of the major advantages of ESR over VAR is its ability to impart a considerable amount of chemical refining to the metal, especially desulphurization. Also, as discussed in Section 3.1.2, a considerable reduction and redistribution of oxide inclusions occurs during ESR. Since the revival of interest in ESR during the 1950's in the Soviet Union these reactions have been the subject of extensive investigations (see Section 2.3).

Unfortunately, the analysis of an ingot yields only the resultant or the net sulphur or oxygen transfer and gives no indication of where and how these reactions take place. There are six possible sites or interfaces where reactions can take place. They are:

(i) the electrode-atmosphere interface

(ii) the slag-atmosphere interface

(iii) the electrode tip-slag interface

(iv) the droplet-slag interface

(v) the metal pool-slag interface

(vi) the metal pool-ingot interface

These sites are shown in Figure 3.1. In the case of DC ESR, an indication of the dominant slag-metal reaction site can be obtained by comparing the sulphur or the oxygen level between two ingots melted by the two different modes. The direct experimental determination of the dominant slag-metal reaction site in ESR is the principal object of this study.

3.3 An Apparent Contradiction in the Results of DC ESR

As we have seen in Section 3.1, the extent of sulphur or oxygen refinement during ESR depends very much on the mode of melting, i.e., whether it is AC, DC electrode +ve or DC electrode -ve. Thus a clear dependence of desulphurization and deoxidation on the polarity of DC remelting indicates the importance of electrolytic reactions in ESR.

Further, as the electrolytic reactions always oppose each other at the electrode and at the pool, the determination of the dominant reaction site is possible by the analysis of sulphur and oxygen levels in the ingot.

For example, Medovar et al.(1), working with a small-scale laboratory ESR unit, report good desulphurization and deoxidation with DC electrode +ve, whilst with DC electrode -ve virtually all the sulphur and oxygen was retained in the metal. This would indicate that the metal pool-slag interface is the dominant reaction site, since the polarity determines the ingot sulphur and oxygen levels. This is in agreement with the results obtained by Whittaker(19), Hlineny and Buzek(18,90), Swinden(91), and Holzgruber et al(12) on 3" diameter moulds. All these authors used laboratory ESR rigs with mould diameters between 2 and 5 inches.

On the other hand, the results of Holzgruber et al(12) using a 17" diameter mould are shown in Figure 3.2. As can be seen from this figure, better desulphurization and deoxidation are obtained with DC electrode -ve as compared to DC electrode +ve. Similar results are also obtained by Kusamichi and coworkers(20) using 8" diameter moulds. All the above results are summarized (schematically) in Figure 3.3 (reference 12), which indicates a switch of the dominant reaction site from the metal pool to the electrode tip for ingots greater than about 6" in diameter.

This apparent contradiction of results, between ingots less than 6" diameter and greater than 6" diameter, was explained by Holzgruber et al(12) on the basis of electrochemical reactions at the slag-metal interfaces. In order to drive a slag-metal reaction in the opposite direction to its normal chemical one, there must be a certain minimum overpotential across the boundary. As soon as current is passed across the interface, an overpotential exists and whenever this reaches a certain minimum value, the chemical reaction may be reversed.

In the case of DC ESR in moulds up to about 5" diameter, current densities and hence overpotentials at both the interfaces are beyond this limiting value and hence other factors such as residence time, etc., become important. Thus, the pool-slag interface is the dominant reaction site for ingots up to 5" diameter.

With increasing ingot diameter, current densities at both the interfaces decrease, as shown in Figure 3.4. At a certain point, however, the current density at the pool will be below the limiting value while that at the electrode will still be above this value. In this dual situation only the polarity of the electrode will become important in determining the results obtained in DC ESR.

Eventually, an ingot size will be reached where both the electrode and the pool current densities will be below this limiting value, and from this point on, polarities will have little or no further effect on the results.

3.4 Polarization in ESR

The dependence of melt rate and pool shape on the melting mode can be successfully explained on the basis of ion polarization in ESR. It must be remembered that, in the CaF_2 based slags used in ESR, the cations (Ca^{2+}, Al^{3+}, Fe^{2+}, etc.) are smaller and more mobile than the anions (F^{1-}, S^{2-}, O^{2-}, etc.).

As can be seen from Figure 3.3, for ingots of all diameters the melt rate increases in the order DC electrode -ve, AC and DC electrode +ve. In the case of the DC electrode positive mode, anion polarization occurs at the electrode-slag interface, resulting in a high local resistance at that interface, thus generating more heat at the electrode tip. This results in a high melt rate and a relatively low power consumption. The reverse is true for the DC electrode negative case where anion polarization at the pool-slag interface results in a deeper molten pool and a lower melt rate. Polarization effects also occur in the case of AC ESR using normal line frequencies of 50 or 60 Hz(11), giving rise to intermediate melt rates.

Mitchell and Beynon(75) measured anodic and cathodic overpotentials, resulting from concentration polarization, at different current densities. Because of the large current densities imposed, a transient method had to be used to avoid gross chemical and thermal changes in the system. A galvanostatic pulsing technique, essentially as used by Ghosh and King(92), and as outlined by Delahay(93) was used. It mainly consists of measuring the rise of potential between the working electrode (in this case a molten droplet of pure iron held by surface tension on the end of a solid iron rod) and the reference electrode (graphite) as a current is suddenly passed through the cell. The decay of potential as the power is switched off can also be used. This method also eliminates the large ohmic drop between the working electrode and the reference electrode.

Anodic and cathodic polarization curves obtained for CaF_2-Al_2O_3 and CaF_2-CaO systems are shown in Figure 3.5. It can be seen that, except at very high current densities, the anodic overpotential is much greater than the cathodic overpotential, especially in the slags containing Al_2O_3. This quantitatively substantiates the simple qualitative argument given above on the basis of anionic and cationic diameters. The anionic polarization curves shown in Figure 3.5(a),(c) can be seen to have three distinct regions, A, B and C, as shown in Figure 3.6. The sections A are found to fit the general equation:

$$\eta = \frac{RT}{nF} \ln \frac{i_D - i}{i_D} + C \qquad (3.22)$$

where η is the overpotential, i_D is the limiting current density, i is the current density, and C is any constant. Hence, the presence of a diffusion limited reaction leading to a limiting current density, i_D, is indicated. Mitchell(75) contends that the simplest anodic reaction:

$$Fe_{(\ell)} \rightarrow (Fe^{2+}) + 2e^- \qquad (3.23)$$

should not lead to such a limiting law unless there is a local saturation of Fe^{2+} resulting in the precipitation of an FeO saturated liquid on the anode surface. At this point, the polarization curve enters the section B in Figure 3.6. At higher current densities the rate of electron transfer can only be accommodated by increasing the Fe^{2+}/Fe^{3+} ratio represented by the slope of the plateau region B. At sufficiently high current densities further electron transfer can only take place by gas evolution by the reaction:

$$(O^{2-}) \rightarrow 1/2\ O_{2(g)} + 2e \qquad (3.24)$$

resulting in arcing similar to the "anode effect" in aluminum electrolysis.

Mitchell and Beynon(75) also measured overpotentials during DC ESR and the values agreed well with those predicted from the above small-scale polarization experiments. This indicates that polarization was not affected by the electrode melting and the different hydrodynamic conditions in ESR. The presence of an iron oxide layer on the anodic electrode and in the slag skin of anodic ingots indicates the validity of the above proposal. No such oxide layers were found on the cathodic electrode.

They suggest the deposition of calcium or aluminum ions as the Faradaic mechanism for electron transfer at the cathodic interfaces.

3.5 Theory Behind Direct Experimental Determination of the Dominant Reaction Site

The main purpose of this study is to obtain direct experimental evidence of the dominant reaction site in AC ESR. It is proposed that this can be achieved by obtaining reaction rates at each site from purely mass balance considerations. Obviously, this requires the knowledge of the sulphur concentration of the metal droplet, $[S]_D$, which led to the development of the graphite droplet sampling spoon described in the next chapter. For reasons that will be apparent in the discussion later in Section 5.10, it is assumed that no change in the droplet sulphur concentration takes place during its fall through the slag.

The rate of change of metal sulphur from the initial electrode sulphur concentration, $[S]_E$, to the drop sulphur concentration, $[S]_D$, is equal to the rate of sulphur transfer at the electrode tip-slag interface, ERATE (g/s). Hence:

$$\mathrm{ERATE} = ([S]_E - [S]_D)\,\frac{\dot{m}}{100} \tag{3.25}$$

where $\dot{m}$ is the melt rate (g/s).

Now, if the sulphur balance at the pool is considered, the rate of increase of sulphur in the pool should be equal to the rate of sulphur input into the pool minus the rate of sulphur lost from the pool, i.e.,

$$\frac{d}{dt}\,(M_p[S]_p\ /\ 100) = \dot{m}\,[S]_D/100 - \dot{f}[S]_I/100 - \mathrm{PRATE} \tag{3.26}$$

where PRATE is the rate of sulphur transfer from the pool to the slag (g/s), M_p is the mass of the pool (g), $[S]_p$, $[S]_I$ are pool and ingot sulphur concentrations respectively (in wt.%) and $\dot{f}$ is the freezing rate (g/s).

By simply rearranging equation (3.26) the equation for PRATE can be obtained:

$$\mathrm{PRATE} = \dot{m}[S]_D/100 - \dot{f}[S]_I/100 - \frac{d}{dt}\,(M_p[S]_p/100) \tag{3.27}$$

Finally, the sulphur balance for the slag gives:

$$\text{ARATE} = \text{PRATE} + \text{ERATE} - \frac{d}{dt}[M_{slag}(S)_S/100] - \frac{d}{dt}[M_{skin}(S)_{Sk}/100] \tag{3.28}$$

where ARATE is the rate of sulphur transfer from the slag to atmosphere (g/s), M_{slag}, M_{skin} are the weights of the slag cap and slag skin respectively (g), and $(S)_S$, $(S)_{Sk}$ are the wt.% sulphur in the slag cap and slag skin respectively.

In the above equations, ERATE and PRATE are taken to be positive if the transfer is from the metal to the slag and ARATE is taken to be positive when it is from the slag to atmosphere. The three rates are schematically shown in Figure 3.7. The directions of the arrows show the positive direction of each rate. Thus, all the three rates can be obtained as a function of time from the above equations if the pertinent sulphur concentrations are known.

CHAPTER IV

EXPERIMENTAL APPARATUS AND PROCEDURE

4.1 Equipment

The experimental work was carried out on a 150 KVA electroslag unit which is capable of remelting up to 8 inch (20 cm) diameter ingots, using an AC or DC power supply.

The equipment can be conveniently divided into four major sections:

(1) Transformer and rectifier unit (power source)
(2) Electrode travel and drive mechanism
(3) Base-plate assembly, and
(4) Remelting platform and control console.

4.1.1 Transformer and Rectifier Unit

The power source consists of an air cooled 150 KVA (output) transformer, a rectifying unit for DC output and an automatic control circuit to obtain a constant voltage output which can be preset according to the melter's choice. The input to the transformer is a single phase, 60 Hz, 550 volts AC line with a maximum primary current of 350 A. The maximum AC output specification is 50 V at 3000 A while the DC outputs are slightly lower at 43 V and 2800 A. Rectification is carried out by two sets of four water cooled solid state diodes. A saturable core reactor is incorporated on the primary side of the power transformer as a means of secondary voltage control through the automatic control circuit. The unit can be shut off in any of the following ways: (a) a remote control switch on the control panel, (b) a shunt trip, when the primary current exceeds a certain value, and (c) when the water pressure is outside the required limits. Water is used for cooling the rectifiers and the unit operates in the pressure range 20 - 40 psi. The recommended value is 30 psi, which gives a flow of about 1 gallon/min.

4.1.2 Electrode Travel and Drive Mechanism

The electrode holder consists of a copper block, to which one of the power leads is attached, and a steel clamping plate (see Figure 4.1). It is designed to hold a 3" diameter electrode firmly, supporting the entire weight of the electrode and making a good electrical contact with it. The holder is mounted on a buggy which runs on rails, allowing motion in vertical direction only.

The electrode drive mechanism consists of a 1/5 HP DC servo-motor E-650 MGHS (Motomatic) with a controlled speed range of 0 - 2750 rpm. The set speed is maintained independent of changing load by means of a tacho-generator feedback. This is essential in order to maintain a constant feed rate inspite of the continuous reduction of electrode weight. The circular motion of the motor is converted to the vertical motion of the electrode holder by means of a chain drive. The correct speed and torque is obtained by the use of a gear box, and a variable slipping clutch prevents accidental overloading of the motor.

4.1.3 Base-Plate Assembly

Figure 4.2 is a photograph of the base-plate assembly. It consists of a water-cooled copper base-plate which forms the second terminal of the power input, the water-cooled power cable being bolted to it. The base-plate is insulated from the supporting plate by compressed asbestos. The supporting plate, which is of 1/2" thick aluminum, rests on three ball castors which allow the base-plate to move in the horizontal plane, and which are adjustable in height so that the base-plate can be levelled. Two pneumatic cylinders, at right angles to each other, are used to center the mould about the electrode. The entire assembly is restricted to move in the vertical direction only by the buggy which moves on steel tracks. Vertical motion is obtained by two vertical pneumatic cylinders (not seen in the photograph) each providing about 700 pounds thrust. The cylinders also support the assembly during melting. The starting pad, with the spike welded on it for a cold slag start, can also be seen in the photograph.

4.1.4 Remelting Platform and Control Console

The remelting platform is about 7 ft. x 7 ft. and approximately 7 ft. from the ground. During remelting the mould and its carriage are supported by the baseplate, but during stripping the mould carriage is supported by the platform, while the ingot is withdrawn by lowering the base-plate assembly.

The control console is situated on the platform and it has meters reading the primary current; AC output voltage, current and wattage;

DC output voltage and current. Controls for the following are located on the console: (1) the applied voltage, (2) the electrode movement, (3) the base-plate positioning, in both vertical and horizontal planes, (4) the power shut off. However, operations such as switching on the power, setting various water flows and selecting the mode of power (AC or DC) cannot be done from the working platform.

4.2 Mould

A water-jacketed copper mould was used for this study. The jacket was formed by two co-axial copper tubes sealed at top and bottom by brazed-in copper rings. The water inlet and outlet pipes, consisting of two 1/2" diameter, 6" long copper pipes, were fitted at the bottom and top of the mould respectively.

The mould had an internal diameter of 5.825" and an external diameter of 8.5". The water jacket was thus about 1.12" thick. The mould was exactly 12" long.

The mould was electrically insulated from the base-plate by a pad of asbestos paper.

4.3 Materials

In order to increase the compositional changes occurring during remelting, three-inch diameter bars of high sulphur free-cutting steel (AISI C1117) were used as electrodes. The nominal composition of AISI C1117 is 0.14 - 0.20% C, 1.00 - 1.30% Mn, 0.04% max. P, 0.08 - 0.13% S.

Fresh CaO was made by calcining pure $CaCO_3$ obtained, in powder form, from Fisher Scientific Co. Calcium fluoride was obtained from Eldorado Nuclear Ltd.

4.4 Slag Preparation

As seen in Chapter II, the thermodynamics of the CaF_2-CaO-FeO system(21,67) and the CaF_2-CaO-CaS system(16,22,55) are fairly well established and for this reason it was decided to study the transfer of sulphur in ESR using CaF_2-CaO slags.

It is difficult to obtain pure CaO as it is highly hygroscopic and hence it was decided to make it fresh by calcining calcium carbonate. The required quantity of $CaCO_3$ was calcined at about 1000°C in a graphite crucible in an induction furnace before a weighed amount of CaF_2 was added and the temperature raised to about 1500°C to form a fused homogeneous mass. The molten slag was then poured into a steel mould to solidify quickly and was crushed just before use. To prevent any appreciable amount of moisture pick up, the slag was prepared in this manner only half-an-hour to an hour before the actual remelting. The components were added in the correct proportions to make up the desired slag composition.

4.5 Starting Procedure

The procedure of cold slag starting is shown in Figure 4.3. The electrode is driven down onto a spiked starting pad (5 1/2" diameter), the dimensions of the spike being approximately 4" x 5/8" diameter. About

3 1/2 - 4 kg. of crushed slag are poured into the mould. The electrode is then raised a few millimeters, and the power turned on, thus striking an arc between the electrode and the spike. The starting spike burns back, melting the slag surrounding it and the electrode is driven down until the stable remelting conditions are established.

The control of electrode movement during a cold slag start was found to be quite critical. If the electrode was driven down too fast, it would weld on to the spike or the starting pad and short the power supply. If the electrode was not driven down fast enough, solid slag would fall in between the electrode and the pad and prevent any further electrical contact.

4.6 Sampling

From Section 3.5, it can be seen that the sulphur concentrations in the pool, droplet, slag and ingot must be known as a function of time before rates at all the three interfaces can be calculated. Hence, the following samples were taken at convenient intervals during the run.

4.6.1 Pool Samples

Initially, attempts were made to obtain clean, slag-free pool samples using evacuated and sealed silica tubes. However, the tubes would soften and bend excessively before sampling was completed due to the high slag temperatures. The normal suction samples using silica tubes and a rubber aspirator bulb proved quite adequate, although at times small amounts of slag were found along with the sample. By and large, the pool samples were sound in the middle with the ends slightly oxidized and hollow. The unsound portions were cut off from the sample and the sample cleaned on a belt grinder before analysis.

It was also found that the quality of the samples improved on deoxidation with aluminum foil. In addition, slag could be prevented from entering the sampling tube by pressing the aspirator bulb while pushing the tube through the slag layer.

4.6.2 Droplet Samples

As explained in the last chapter, droplet samples were absolutely essential to the determination of the amounts of sulphur transferred to the slag at the electrode and pool site. Droplets were caught by the special samplers shown in Figure 4.4. The sampler consisted of a graphite spoon, hollowed out of a section of an annular graphite ring, which screwed on to a 1/4" diameter graphite rod about 10" long. As shown in the figure, this rod was attached to a metal handle by an allen screw so that it could be quickly replaced for the next sample. The spoon was inserted into the annulus between the mould and the electrode, then rotated under the electrode tip to collect a droplet. The sampler was removed in the reverse manner and quickly quenched in water. The lower portion of Figure 4.4 shows the position of graphite spoon as it enters the mould and during sampling (as seen from top), while the upper portion shows the side view during sampling. As the samples were taken out and quenched immediately, reaction during sampling is minimized. The very slight increase in current during sampling (25A) due to the presence of a more conductive graphite sampler in the slag bath, is not expected to affect the result to any great extent.

It was generally found that a small portion of slag was contained below the top surface of the droplet sample. This is most probably due to the sudden contraction during solidification as the droplet was being quenched. However, another explanation, based on the surface tension arguments, has been given by Lu(98). Each droplet, therefore, had to be annealed, cut and carefully cleaned before analysis.

4.6.3 Slag Samples

Dip slag samples were very easily taken by quenching them on a 1/2" diameter 3" long copper rod, which was screwed on to a 12" long asbestos bar.

4.7 Experimental Measurements

4.7.1 Measurements and Analyses Before a Run

Drillings were taken at various points along the diameter of the electrode and analysed for sulphur. It was found that the mid-radius sulphur concentration was higher than the rest of the electrode. It was assumed that this segregation pattern would not change appreciably along the length of the electrode. The mean sulphur concentration in the electrode is then given by the weighted mean of the sulphur distribution along the diameter. This could be easily obtained in practice by turning the electrode off on the lathe along the diameter and mixing the chips well before analysis.

The spike was welded on the starting pad and the weight of the starting pad and spike was noted. This was done in order to obtain the accurate weight of the ingot by subtracting this weight from the weight of ingot and starting pad at the end of the melt. The weight of slag charged was also noted.

4.7.2 Measurements During a Run

After the initial instability, power characteristics settle down to values which primarily depend on the slag conductivity and electrode descent rate. In these experiments, a constant voltage (30 V) was preset and the electrode descent rate was adjusted to give currents around 2500 A. Generally the current and voltage remained stable throughout the melt and these values were noted.

The electrode positions at various times during the melt were noted and from these values the electrode descent rate was calculated.

Sampling was started somewhere half-way through the melt, assuming that effects of the initial cold start had died out and that stable melting conditions had been established. In order to synchronize the ingot sulphur analyses with the other samples taken during the melt, a few grams of fine tungsten powder were dropped into the pool at the start of the sampling period. This served not only to mark the position of solidification front at the beginning of sampling period, but also to outline the pool profile from which pool volumes were estimated. The end of the sampling period coincided with the end of the melt and tungsten was again used to mark the pool. The time at which various samples were taken were noted.

4.7.3 Measurements and Analyses After a Run

After a run, the individual weights of the slag cap and slag skin were noted, the sum of these weights plus the weight of slag lost with droplet samples giving the weight of slag charged. The slag cap and skin were separately crushed and ground and their average sulphur contents were determined.

The ingot and starting pad were weighed and then the starting pad was cut off for use in a subsequent experiment. The ingot was sectioned longitudinally and from one half, drillings were taken between the two tungsten marks along the ingot axis. These samples were analyzed for sulphur and oxygen. The other half of the ingot was surface ground, polished and then etched with amonium per sulphate solution to reveal clearly the tungsten trace of the solidification profiles and the macrostructure.

4.8 Chemical Analysis

All the metal samples were analysed for sulphur by the standard Leco technique which consists of direct combustion of the sample in an oxygen atmosphere and estimating the evolved SO_2 by absorbing it in acidified starch iodide solution, while titrating continuously with potassium iodate. The analysis was standardized using NBS metal standards. The accuracy of this method is reported to be within ± 3%.

The oxygen in the metal samples were analysed by the inert gas fusion method.

The sulphur in the slag was analysed by the same method as used for metal except that high purity iron powder was used as the base. Slag analyses were checked by a standard gravimetric method(94) which is reported in Appendix I.

4.9 Calculations

4.9.1 Melt Rate from Ingot Weight and Electrode Descent Rate

An accurate ingot weight was obtained by subtracting the weight of the starting pad from the weight of ingot plus starting pad at the end of the melt. The melt rate was simply found by dividing this ingot weight by the total time of melting.

Electrode positions were plotted against time and the slope of this graph gave the electrode descent rate, R_E, from which melt rate can be estimated by the formula:

$$\dot{m} = R_E \left(\frac{D_I^2 + D_E^2}{D_I^2} \right) \frac{\pi}{4} D_E^2 \rho_{Fe} \qquad (4.1)$$

where $\dot{m}$ is the melt rate, g/s,

R_E is the electrode descent rate, cm/s,

D_I is the ingot diameter, cm,

D_E is the electrode diameter, cm, and

ρ_{Fe} is the density of steel, g/cm^3

4.9.2 Pool Volume from Pool Profile

It was found that pools were not quite symmetrical about the ingot axis and so the left and the right hand sides of the pools were separately mapped every half a centimeter along the pool axis (X-direction) (see Figure 5.4). Fourth order curves were fitted by computer to each half tungsten pool profile by a least square technique. The volume of each half was numerically computed by dividing the profile into 100 equal parts of thickness ΔX and using the formula:

$$\text{Volume} = \sum_{i=1}^{1000} \pi Y_i^2 \Delta X \tag{4.2}$$

Thus the tungsten pool volumes of each half were independently obtained and added to the excess pool volumes to obtain the total pool volumes (see Figure 5.4). As shown in Figure 5.4, excess pool volumes are the volumes of the cylindrical portions of the pools above the tungsten pool profiles, which are calculated from the levels of the pools at that time. Average pool volumes were taken as the average of left and right hand pool volumes.

4.9.3 Sulphur Concentration as a Function of Time

The data giving the variation of sulphur content with time were treated by linear regression. The intercept and the slope of the least square line were obtained using a standard technique (Appendix IIA). The 95% confidence intervals were calculated from the variance of the points about this line, using the formula given in Appendix IIA. Appendix IIA also provides the formula used for calculation of correlation coefficient which was then compared with the critical correlation coefficient given in reference (95), as a test of significance.

4.9.4 Rate Calculations

For the calculations of rates at the three interfaces, the following data were required:

(i) the intercepts and slopes of all the four least square lines representing the drop, ingot, pool and slag concentrations as a function of time,

(ii) the total time between the two tungsten marks, TIME-S,

(iii) the average sulphur in the electrode, $[S]_E$-wt.%,

(iv) the initial and final average pool volumes, VOL1 and VOL2 respectively, cm^3,

(v) rate of slag skin formation, SKINRT - g/s,

(vi) average sulphur in the skin, SSKIN - wt.%,

(vii) initial weight of the slag charged, WSLAG - g,

(viii) the times at which the drop samples were taken - s, and

(ix) the melt rate, $\dot{m}$ - g/s.

The weight of the slag pool at any time, WSLAG, was calculated by subtracting from the initial slag weight the weight of slag skin formed and an average of 20 gms of slag for each drop sample taken.

The inequality of initial and final pool volumes suggest a variation in freezing rate, the melting rate being constant. It has been assumed that the process is tending towards stability and hence the final freezing rate is equal to the constant melting rate. It was also assumed that change in freezing rate from the initial to the final value is linear so that the initial freezing rate is given by:

$$\dot{m} + \text{VOLINC} \text{ where } \text{VOLINC} = 7\ \left(\frac{\text{VOL2-VOLI}}{\text{TIME}} \right)$$

Thus, the freezing rate at any time "t" is given by:

$$\text{FREZ} = \dot{m} + \text{VOLINC} + \text{FREZIN} * t \tag{4.3}$$

where
$$\text{FREZIN} = - \frac{\text{VOLINC}}{\text{TIME}}$$

The pool size at any time was calculated from:

$$\text{VOL} = \text{VOLI} + \text{VOLINC} * t \tag{4.4}$$

The three rates, ERATE, PRATE and ARATE were calculated using the formulae derived in Section 3.5. They were calculated at one second intervals using a CDC 6400 computer and were printed out at 50-second intervals. ERATE was simply calculated using equation (3.25):

$$\mathrm{ERATE} = \frac{\dot{m}}{100}\left([S]_{E,t} - [S]_{D,t}\right) \tag{4.5}$$

where the second subscript "t" is used to denote the sulphur concentration at time "t". The last term in equation (3.27) was calculated as:

$$(M_p[S]_p/100) = \mathrm{DELSP} = (\mathrm{VOL}-\mathrm{VOLINC}) * [S]_{p,t-1} - \mathrm{VOL}*[S]_{p,t} \tag{4.6}$$

and hence, PRATE was obtained from the relationship:

$$\mathrm{PRATE} = (\dot{m}[S]_{D,t} - \mathrm{FREZ} * [S]_{I,t} + \mathrm{DELSP})/100 \tag{4.7}$$

A transformed form of equation (3.28) was used to obtain ARATE:

$$\begin{aligned} \mathrm{ARATE} = {} & \mathrm{ERATE} + \mathrm{PRATE} - \mathrm{SKINRT} * \mathrm{SSKIN}/100 \\ & - \mathrm{CORR(I)} * (S)_{S,t}/100 + \mathrm{WSLAG} * (S)_{S,t-1}/100 \\ & - [\mathrm{WSLAG} - \mathrm{SKINRT} - \mathrm{CORR(I)}]\,(S)_{S,t}/100 \end{aligned} \tag{4.8}$$

where CORR(I) represents the average correction for slag lost during droplet sampling. CORR(I) took the value of 20 g or zero depending on whether a droplet sample was taken at time "t". The correction for the sulphur lost with the slag during droplet sampling is the extra term added to equation (3.28).

4.9.5 Electrode Tip Surface Area

In order to determine the curved surface area of the electrode tip, it was mapped in the same way as the metal pool (see Figure 5.4). As in the case of the metal pool, the left and the right hand side were mapped separately due to the lack of symmetry about the tip axis. Second or third order curves were fitted to the profiles using least square techniques. The area was numerically computed by dividing the profile into 1000 equal parts of thickness Δx and using the formula:

$$\text{Area} = \sum_{i=1}^{1000} \frac{2\pi y_i \; \Delta x}{[1+(dy/dx)_i^2]^{1/2}} \qquad (4.9)$$

where the denominator represents the correction factor to obtain the curved electrode tip area. An average between the left hand and the right hand side areas was computed and added to the area of the cylindrical portion of electrode immersed in the slag to obtain the total surface area of the immersed electrode.

4.9.6 Slag Conductivity

An estimate of slag conductivity can be obtained once the voltage, current, electrode areas and distance between electrodes is known.

The density of the appropriate slag at 1700°C was estimated by extrapolating the data given in reference (13) and, knowing the slag weight, the slag volume at that temperature was calculated. The height of the slag bath was obtained from the slag volume and the average distance between electrodes, L, was estimated from the relationship:

$$L = h_S - \left(\frac{h_1 + h_2}{2} \right) \tag{4.10}$$

where h_S is the estimated height of slag bath, h_1 is the height of cylindrical portion of electrode immersed in the slag and h_2 is the average height of the curved electrode. These distances along with the average electrode tip-pool distance (L) are shown in Figure 4.5. The resistance was simply calculated by dividing the voltage by the current, while the average area of the electrode and the ingot was taken as the effective area. The conductivty (χ) was calculated using the relationship:

$$\chi = L/RA \tag{4.11}$$

where R is the resistance of slag bath in ohms and A is the effective area of electrode in cm^2.

4.9.7 Approximate Overall Sulphur Balance

An approximate distribution of the total sulphur input into the system can be obtained by doing a sulphur balance. Assuming that no sulphur is present in slag initially, sulphur input can be obtained from the average electrode sulphur and the weight of electrode melted (= ingot weight). This sulphur is distributed between the ingot, the slag cap, the slag skin and the atmosphere.

The total sulphur in the ingot can be calculated if it is assumed that the regression line representing the distribution of sulphur during the sampling period can be taken to represent the sulphur distribution along the whole length of the ingot. With this assumption, the total sulphur in the ingot, $[TS]_{Ingot}$, is given by:

$$[TS]_{Ingot} = \int_0^T \frac{\dot{f}_{av}}{100} [a+bt] \, dt + \frac{[S]_{P,T} \times VOL2 \times 7}{100} \tag{4.12}$$

where $\dot{f}_{av}$ is the average freezing rate,

a and b are the intercept and the slope of least square ingot sulphur line,

$[S]_{P,T}$ is the pool sulphur concentration at the end of the melt, and

VOL2 is the final pool volume.

Equation (4.12) can be simply integrated to yield:

$$[TS]_{Ingot} = \frac{\dot{f}_{av}}{100} [aT + \frac{bT^2}{2}] + \frac{[S]_{P,T} * VOL2}{100} \times 7 \tag{4.13}$$

The average freezing rate, $\dot{f}_{av}$, is obtained by dividing the difference between the ingot weight and final pool weight by melt time. Note that a is not the intercept at the start of sampling but at the start of the melt.

The sulphur in the slag cap and slag skin can be estimated from their final and average sulphur concentrations and their respective weights.

The difference between the sulphur input from the electrode and the total sulphur in the ingot, slag pool and slag skin must be lost to the atmosphere from which an average ARATE can be calculated.

CHAPTER V

RESULTS AND DISCUSSIONS

5.1 Introduction

General information concerning the successful melts are given in Table 5.1. Calcium fluoride-based slags containing 5, 10 and 20 wt.% CaO were used in this study to melt 3" diameter, high sulphur AISI 1117 grade steel electrodes into a 5.825" diameter water cooled copper mould. The melting current and voltage along with total melt time, weight of ingot melted, weight of slag charged and melt rate are reported in Table 5.1. This table also gives the total time of sampling, which is the time between the tungsten additions. As explained in Section 4.7.2, the end of sampling coincided with the end of the melt.

Some trial melts were performed in order to ascertain optimum melting characteristics with different slags and to try out various sampling techniques. The techniques described in Section 4.6 were finally chosen.

5.2 Melt Rate

As explained in Section 4.9.1, the melt rate was found by dividing the ingot weight by the melt time. The results are given in Table 5.2. It can be seen that the melt rate increases with increasing lime content of the slag, although the power input in the three cases were not very different (82.5 KVA in Melt 24 compared to 75 KVA for the other two). This is consistent with the observed increase in slag resistivity with increasing addition of CaO in CaF_2-based slags(29-31) (see also the slag resistivity calculation in Section 5.12).

Operating at constant current and voltage, the higher the slag resistivity the shorter the electrode-ingot distance, so that the same amount of heat is liberated in a smaller zone leading to a higher rate of electrode burn-off. This is borne out by the calculations in Section 5.12. As shown in Table 5.43, the average distance between the electrode and the ingot pool decreased with increasing lime content in the slag, resulting in an increase in melt rate.

Tables 5.3, 5.4 and 5.5 give the electrode positions at various times during the melt for melt numbers 21, 24 and 25 respectively. These data are plotted in Figures 5.1, 5.2 and 5.3. The linearity of these plots, especially after half-way through the melt, suggest uniformity in melting conditions, at least during the sampling period. The slopes of these plots give the average electrode descent rate, R_E, for each melt and they are reported in Table 5.6. Using equation (4.1) and these values of electrode descent rate, melt rates were calculated and are also reported in Table 5.6. The pertinent values of ingot diameter, D_I, the electrode diameter, D_E, and the metal density, ρ_{Fe}, used in the calculations are given in Table 5.6.

The melt rates calculated in this way do not agree with the actual melt rate obtained from ingot weight, but in all the cases, they were within 10% of the actual value. This diasgreement is probably due to the use of inaccurate values of R_E arising from errors in electrode position measurement. A part of this discrepancy may also be due to assumptions involved in the derivation of equation (4.1). Equation (4.1) assumes that negligible volume changes take place during solidification and the cooling of the ingot; that the solidification rate is constant and equal to melting rate; and that the ingot has no flaws, such as blowholes. Only the last assumption may be valid during the melt, though in the final pool blowholes were observed.

The ratio of actual melt rate to the electrode descent rate is almost identical for melts 21 and 24, while it is somewhat different -- although closer to the theoretical ratio -- for melt 25. These discrepancies may be due to variations in melting conditions and ingot diameters.

5.3 Ingot Pool Profile and Pool Volume

After the ingot was sectioned, surface ground, polished and etched with amonium per sulfate solution, the left and the right hand tungsten pool profiles were separately mapped. At intervals of half-centimeters on the X-axis, Y values were read off as shown in Figure 5.4. These pairs of values of X and Y are reported separately for each half of both the initial and final pool profiles in Tables 5.9 and 5.10 for melts 24 and 25 respectively. In the case of melt 21, the ingot was unfortunately sectioned at a distance Z = 1.11 cm away from the centre axis of the ingot. The tungsten profile on this section was mapped at 1/4" intervals as shown in Table 5.7; the pool volume could not be calculated directly from this profile using the technique described in Section 4.9.2 since that technique is only valid for sections passing through the ingot axis. An estimate of the value of Y at centre section, Y_{CORR}, was obtained from the value of Y at a section Z = 1.11 cm away from the centre using the relationship:

$$Y_{CORR} = \sqrt{Y^2 + Z^2} \tag{5.1}$$

Values of X were simply corrected by adding the extra distance by which the origin of the centre section was estimated to be below that of the offset section. The corrected pool profiles of Ingot 21 are given in Table 5.8.

Following the method outlined in Section 4.9.2, the initial tungsten pool volumes were calculated and are given in Table 5.11. This table also gives the coefficients of the fourth order curves fitted to each half of the tungsten pool profile together with the weighted sum of squares of residuals. These curves fitted the profiles very well away from the origin, but near the origin some deviations existed. The errors in volumes arising from these deviations were estimated to be very small and were neglected. The excess pool volumes were calculated by multiplying the pool area with the height of the cylindrical portion of the pool as shown in Figure 5.4. The average pool volume was obtained by taking the average of the left hand and right hand total pool volumes. Similarly, final pool volumes were calculated and are reported in Table 5.12.

From Tables 5.11 and 5.12, it can be seen that initial and final pool volumes of all the three melts are substantially different. As mentioned in the last chapter, this would indicate changes in freezing rate during the sampling period if the melting rate was constant during that period. As discussed in Section 5.2, the linearity of electrode position vs. time plots (Figures 5.1, 5.2 and 5.3) during the sampling period show that the melt rates did not change significantly. Thus, a change in freezing rate is implied. The direction of this change depends on whether the pool volume is increasing or decreasing. An increase in pool volume, as in the cases of melts 21 and 25, implies reduction in freezing rate while the reverse is true for melt 24.

In this study, in the absence of any other information, it was assumed that the rate of change of freezing rate was constant. On the basis that the process would tend towards a steady-state, it was further assumed that the freezing rate tends to the melting rate at the end of the melt. With these assumptions, the freezing rate at any time is given by equation (4.3).

Except in the case of melt 25, it was observed that the pool shape changed considerably. The initial pool shape was flatter than the final pool shape. This may be explained by considering the geometry of heat extraction from the ingot. As the ingot builds up, the heat extracted axially by the base-plate is reduced while more heat is extracted by the mould. This results in a greater degree of radial solidification as compared to axial solidification as the melt proceeds and hence the rounder the final pool.

5.4 Drop, Ingot, Pool and Slag Sulphur Concentrations as a Function of Time

Tables 5.13 to 5.16 give the results of the sulphur analyses for the drop, ingot, pool and slag samples taken at the times indicated. It must be noted that the time shown in the first column in every table is measured from the beginning of the sampling period, i.e., from the first addition of tungsten powder to the pool.

Relatively few successful drop samples were obtained and it was found that their sulphur concentration values were scattered considerably. Hence duplicate analyses were made where the sample size permitted.

Following the techniques suggested in Section 4.9.3, least square lines were fitted to the raw data. The variances of the populations about these lines were calculated and 95% confidence intervals were obtained. These are reported in the above tables together with the regressional estimate of the sulphur concentration. Table 5.17 summarizes the results of the regression analyses for melt 21. The table also includes values of the critical correlation coefficients for 95% confidence levels. If the correlation coefficient is greater than this critical correlation coefficient, then the regression line is supposed to be significant at the 95% confidence level. A value of the critical correlation coefficient was read off Table 12.10 in reference (95) for a particular sample size and confidence level. Thus Table 5.17 indicates that all four regression lines are significant at the 95% confidence level.

Similarly, Tables 5.18 to 5.21 give raw and processed data for melt 24 while Table 5.22 summarizes the results of the least square analyses. Again, it can be seen that all data are significant at the 95% confidence level. The results for melt 25 are reported in Tables 5.23 to 5.27.

It can be seen that all the regression lines except the one for slag sulphur, are significant at the 95% confidence level. The small correlation coefficient obtained for the slag sulphur line may be due to its very small slope ($\approx 2.5 \times 10^{-7}$ wt.%/s). In other words, the slag sulphur is almost independent of time, resulting in a low correlation coefficient.

Sulphur contents as a function of time are plotted in Figures 5.5 to 5.13 for all three melts. The least square lines and the 95% confidence intervals are also plotted in these figures.

The drop sulphur concentrations can be observed to exhibit a considerable amount of scatter resulting in wider confidence limits. All the sulphur concentrations, except the drop sulphur in melt 25, are found to increase with time.

5.5 Electrode Sulphur

As explained in Section 4.7.1, the turnings off the electrodes were thoroughly mixed and four random one-gram samples taken for analysis. The results are reported in Table 5.28, the same electrode material being used for both melts 24 and 25. The average of these four readings were used as the electrode sulphur concentration in the rate equations. The variance about this mean was calculated and used in the determination of standard errors of PRATE, ERATE and ARATE.

5.6 Rates at the Three Interfaces

Using the parameters calculated up to now and the method described in Section 4.9.4, the three rates, ERATE, PRATE and ARATE at the electrode tip-slag, metal pool-slag and slag-atmosphere interfaces, respectively, can be calculated. The standard errors of the three rates were computed at 50-second intervals using the formulae derived in Appendix IIB. The rates and their standard errors are given in Tables 5.29 to 5.31 for melts 21, 24 and 25 respectively. ERATE can be seen to be always larger than PRATE indicating that amongst the slag-metal sites maximum desulphurization takes place at electrode tip-slag interface thus making it the dominant reaction rate. In fact, in melts 24 and 25 and early in melt 21, resulphurization seems to be taking place as indicated by the negative values of PRATE.

Considerable amounts of sulphur seem to be lost to the atmosphere in all the melts as can be seen from the values of ARATE obtained. In fact, in melt 25 ARATE is found to be comparable to ERATE indicating that most of the sulphur lost from the metal is lost to the atmosphere.

The accuracy of ARATE depends on the accuracy of both ERATE and PRATE and the accuracy of slag sulphur analysis. Thus, as expected, the standard error of ARATE can be seen to be larger than that of either ERATE or PRATE.

The comparison of rates between the melts is made difficult by various factors. Firstly, there was no standardized reference or starting point. Sampling was started arbitrarily, sometime half way through the melt and hence zero time did not necessarily correspond to identical remelting conditions for all melts. Secondly, since the melt rates were different, the rates of sulphur input to the system must be different. In addition, it was almost impossible to obtain two electrodes with identical sulphur contents.

The first two problems could be overcome but it is very difficult to correct for difference in electrode sulphur content. However, a particular weight of electrode melted can be conveniently used as a reference or starting point. Rates are then plotted as a function of the weight of electrode melted from the reference point. This technique accounts for differences in melt rate, since the amount of sulphur input at any weight will be the same for electrodes with identical sulphur contents.

The 95% confidence intervals for the rates cannot be obtained from the standard error since the multiplying factor "t"$_{n-2,0.975}$ can only be obtained if the number of degrees of freedom, n, is known. From Table F (p. 466) in reference (95), it can be seen that for a 95% confidence level "t" varies from 2.571 to 1.960 for $n = 5$ to ∞. Hence two times the standard error is a good estimate for a 90 to 95% confidence interval. It was decided, therefore, to use 2 as an approximate value of "t"$_{n-2,0.975}$.

Tables 5.32 to 5.34 give the three rates and their approximate 95% confidence levels as a function of weight of electrode melted for melts 21, 24 and 25, respectively. The rates and their approximate confidence levels are also plotted in Figures 5.14 to 5.16 for the three melts. In the tables and figures given above, all the rates correspond to the ingot formed in the range 15 - 20 kg.

A further discussion on the three rates can be found in Section 5.10.

5.7 The Rate of Sulphur Transfer at the Ingot-Metal Pool Interface

The final refining of the metal is obtained at the ingot-pool interface due to solute distribution between the ingot and liquid metal pool. This is very similar to a zone refining effect. Thus, this interface could become important for those alloying elements which have equilibrium distribution coefficients much smaller than unity, such as sulphur and oxygen. Hence, the rate of sulphur transfer at this interface from ingot to metal pool has been calculated at 15 kg and 20 kg ingot weights for the three melts. The results are given in Table 5.35.

Calculations were carried out as follows. The estimates of the pool sulphur, $[S]_P$, and the ingot sulphur, $[S]_I$, at any particular time were obtained from the regression lines. The $\Delta[S]$ term reported in Table 5.35 is simply the difference between the above sulphur concentrations. The instantaneous freezing rate, $\dot{f}$, was calculated using equation (4.3) after which the sulphur transfer rate at the ingot-pool interface was obtained from the relationship:

$$\text{Rate at I/P interface} = \frac{\Delta[S]}{100} * \dot{f} \qquad (5.2)$$

Thus, it can be seen that except in the case of melt 24 where the sulphur level in the pool is already quite low, the rate of refining at this interface is considerable. Unless the sulphur rejected from this interface into the pool is removed from the pool by the slag, the excessive sulphur accumulation in the final pool may result in a top discard giving a loss of yield. Hence, this is not necessarily a beneficial effect.

5.8 Equilibrium Pool Sulphur Calculations

As indicated in Section 3.1.3, the equilibrium metal sulphur concentration can be estimated from slag-metal equilibrium data(16,22,55) knowing the metal oxygen and slag sulphur concentrations. Hence, the electrode and ingot oxygen concentrations were determined by inert gas fusion and are given in Table 5.36. Samples were taken at the top, middle and the bottom of the ingot but as the variations in oxygen concentrations were found to be quite small and random, it was decided to take an average of all the readings to represent the overall ingot oxygen content.

Under equilibrium conditions, the values of the function:

$$C_S^! = (\text{wt.\%S})\ (P_{O_2}/P_{S_2})^{1/2} \tag{5.3}$$

can be related to those of the function:

$$C_S^* = (\text{wt.\% S})\ [h_O] / [h_S] \tag{5.4}$$

by the expression:

$$C_S^! = K_7 \cdot C_S^* \tag{5.5}$$

where K_7 is the equilibrium constant:

$$K_7 = (P_{O_2} / P_{S_2})^{1/2} [h_S/h_O] \qquad (5.6)$$

for the reaction:

$$[O]_{1\ wt.\%} + 1/2\ S_{2(g)} = [S]_{1\ wt.\%} + 1/2\ O_{2(g)} \qquad (5.7)$$

In the above expressions, $[h_O]$ and $[h_S]$ are the Henrian activities of oxygen and sulphur in the metal respectively, and (wt.% S) is the corresponding slag sulphur concentration. The value of K_7 at 1500° and 1700°C, calculated from available thermodynamic data(97), are 0.135 and 0.181, respectively.

Table 5.37 gives the values of C_S' determined by Davies et al.(22) at 1500°C. Extrapolation of these values to 1700°C was obtained using the relationship:

$$C_S' \ (1973^\circ K) = C_S' \ (1773^\circ K) \ . \ K_9 \ (1973^\circ K)/K_9 \ (1773^\circ K) \qquad (5.8)$$

as given by Cooper and Kay(87), where K_9 is the equilibrium constant for the reaction:

$$(CaO) + 1/2\ S_2(g) = (CaS) + 1/2\ O_{2(g)} \qquad (5.9)$$

From thermodynamic data(97) a value of 1.81 for the ratio of equilibrium constants in equation (5.8) is also obtained.

From the calculations of the Henrian activity coefficients f_S and f_O of sulphur and oxygen respectively, as shown in Appendix III, it was decided that, within 6% error, it would be accurate to use weight percent concentrations in place of the Henrian activities of sulphur and oxygen.

Thus, referring to Table 5.37, values of C_S^* were obtained from those of C_S' using equation (5.5). The slag sulphur concentration half way through the sampling period and the average metal oxygen content are also reported. From these values and equation (5.4), equilibrium metal sulphur concentrations were obtained and are given in Table 5.37 along with the actual pool sulphur concentrations.

As can be seen from Table 5.37, the actual pool sulphur concentrations are very close to the equilibrium sulphur concentration values indicating a nearly equilibrium situation at the pool-slag interface. This is in agreement with the observations of Cooper and Kay(87) in a small scale laboratory electroslag unit (1.59 cm diameter ingots).

At 1500°C the value of the actual pool sulphur concentration can be seen to be slightly greater than the equilibrium pool sulphur concentration for melt 21 (10% CaO) while the reverse is true for melt 24 (20% CaO). This is incidentally in line with the small positive and negative PRATE obtained for melts 21 and 24 respectively (see Tables 5.32 and 5.33). On the other hand, at 1700°C the equilibrium pool sulphur content is greater than the actual value for melt 21, indicating that pool is closer to 1500°C and 1700°C. This is in agreement with the conclusions of Cooper and Kay(87). The agreement between the experimental and calculated pool sulphur values at 1500°C is dependent on the accuracy of C_S' values given in the literature which are known to vary to some extent$^{(16,22,55)}$. Inaccuracies of sulphur and oxygen analysis are also involved, but it can be safely concluded that the pool-slag interface is very close to equilibrium.

5.9 Overall Sulphur Balance and ARATE

A conventional overall sulphur balance was also done using the method described in Section 4.9.7 and the results are given in Table 5.38. The total sulphur contained in the ingot, the slag cap and the slag skin are shown in this table and the difference between the sum of all the above quantities and the total sulphur input from the electrode is lost from the system. If it is assumed that this sulphur loss is only to the atmosphere, an average ARATE over the entire melting range can be found by dividing the sulphur loss by the total melting time. It is to be noted that this calculation yields a time average ARATE over the whole melting period while the ARATES given in Tables 5.32 to 5.34 are instantaneous values at that time. Since ARATES at the beginning of the melts are expected to be low or negligible, the instantaneous values at the end of the melts should be somewhat larger than the average values. This is found to be true for both the 5% and 20% CaO slags but in the case of melt 21 (10% CaO) a high value of the average ARATE is obtained from the macro balance. In any case, all the average ARATES fall within the error bounds of the ARATES shown in Figures 5.14 to 5.16.

Another useful quantity that can be calculated from the overall balance is the average rate of metal desulphurization, or in other words, the average ERATE + PRATE. This quantity was simply calculated by dividing the difference between the sulphur input and total ingot sulphur by the total melt time. These values of the average rate of metal desulphurization for the three melts are also reported in Table 5.38. It is well known that in ESR the initial rate of metal desulphurization is generally very large leading to almost sulphur free metal at the ingot bottom. Hence, the instantaneous values of the rate of metal desulphurization at the end of the melt should be generally slightly lower than the average values shown in Table 5.38. This is borne out in practice as can be seen from Table 5.39 which summarizes all the rates and expresses them as a percent of rate of sulphur input. The agreements are quite good indicating the internal consistency between these two approaches.

As indicated in Sections 3.2 and 3.5, it is apparent now that the total rate of sulphur removal from the metal could not be separated into the rate of sulphur transfer at the electrode (ERATE) and at the pool (PRATE) from overall sulphur balances alone. The intermediate droplet composition has to be known in order to separately obtain the two rates. Since the main aim of this project was to determine the relative importance of these two slag-metal reaction sites, the development of the graphite droplet sampler was one factor of major importance.

Finally, the overall sulphur balance calculations give a clear indication of how the total sulphur input is distributed. For example, Table 5.38 shows that 14.8, 16.6 and 21.7 percent of the total sulphur input is retained in the final ingot in the melts with 20%, 10% and 5% CaO slags, respectively. This appears anomalous in view of the fact that the sulphur capacities of these slags vary widely, especially for the 5% CaO slag which retained less than half the sulphur input compared with the 10% slag. The answer to this anomaly lies in the 49.1% sulphur loss to the atmosphere in melt 25 (5% CaO) as compared to the 18.1% and 21.7% atmosphere sulphur losses for melts 24 (20% CaO) and 21 (10% CaO) respectively. Thus, an overall sulphur balance gives a good indication of what is happening in each melt and forms a good basis for a simple comparison of different melts.

5.10 Discussion of ESR Reaction Sites

From the results obtained in this investigation and by other workers in this field, the relative importance of the six possible reaction sites in ESR, enumerated in Section 3.2, can be discussed. Further, due to the variation of electrode sulphur concentrations it was realized that a better comparison of the rates could be made if they were expressed as percentages of the rate of sulphur input. Hence, Table 5.39 was constructed. The rate of sulphur input was obtained from the melt rate and the electrode sulphur concentration. The total rate of metal desulphurization was obtained by adding ERATE and PRATE.

5.10.1 Site One: Electrode-Atmosphere Interface

The electrode is heated in a number of ways: (i) resistance heating, resulting from the passage of electric current through the electrode, (ii) conduction from the region immersed in the heated slag and, (iii) radiation from the hot slag. Most of this heat is used in melting the electrode while some is lost to the atmosphere by radiation and convection. Temperature profiles along the electrode axis have been measured by Elliott and Maulvault(99) in a small laboratory rig, using a thermocouple placed in the electrode. Their data reveal that electrode temperatures just above the slag level could be anywhere in the range 800° - 1200°C. They also calculated the temperature distribution in an industrial ESR unit (electrode diameter 37.5 cm) and found that, near slag level, electrode temperatures as high as 1000°C are possible. At these temperatures the oxidation of the electrode by the atmosphere could be substantial and hence an appreciable build up of oxides such as FeO, MnO could be expected. The high values of the activity coefficients of these oxides in CaF_2-based slags (see Section 2.4) does not, in any way, help the situation. Thus, especially for alloys of low oxidation resistance, the oxygen introduced into the system from this site can be excessive and can lead to an intolerable loss of alloying elements. Hence, in melting such alloys neutral or reducing atmospheres are preferred. Industrially, high purity argon or CO/CO_2 gas mixtures can be used.

5.10.2 Site Two: Slag-Atmosphere Interface

Apart from slag loss by volatilization, two important reactions take place at the slag-atmosphere interface: (i) the loss of sulphur to the atmosphere, and (ii) oxygen transfer into the slag by multivalent cations such as Fe^{2+}/Fe^{3+}.

Sulphur is known to be lost from the slag by oxidation (1,11,19,79,87-90) by the reaction:

$$(S^{2-}) + 3/2\ O_{2(g)} = SO_{2(g)} + (O^{2-}) \qquad (5.10)$$

although, in principle, it can also be lost in the form of other volatile compounds such as SF_6(1), H_2S(19), etc. Whittaker(19) analyzed the gases evolved during ESR using a mass spectrometer and found most of the sulphur in the gas in the form of SO_2 whilst only minor quantities of H_2S were detected. No sulphur fluorine compounds were detected.

His experimental results show that very little of the total sulphur transferred to the slag is lost to the atmosphere. However, other authors report that substantial quantities of sulphur are transferred from the slag to the atmosphere, indicating that this interface is an important reaction site as far as overall desulphurization is concerned.

For example, Holzgruber et al.(11) find that, during air remelting, as much as 80% of the total sulphur input is lost from the system to the atmosphere with certain slags. In this investigation, the maximum sulphur lost to the atmosphere was about 49% of the input, when melting with a 5% CaO slag (Table 5.38). Even in the other melts, about 20% of the sulphur input was still lost to the atmosphere. In terms of the instantaneous rates measured between the 15 - 20 kg remelted levels, melt 25 (5% CaO) was losing sulphur at an average rate of 67% of the rate of sulphur input, melt 24 (20% CaO) 27%, and melt 21 (10% CaO) surprisingly only 5.5% (see Table 5.39). The low value of ARATE obtained in melt 21 (10% CaO) cannot be satisfactorily explained especially when the quite large value of the overall loss of sulphur from the system in that melt is considered (see Table 5.38).

Thus, the results of this investigation quite conclusively demonstrate the importance of the slag-atmosphere site for sulphur removal in ESR. The evidence of oxidation of sulphur in the slag by a reaction such as equation (5.10) comes principally from two considerations. It has been observed by Holzgruber and Plockinger(79) and Kasin(88) that the loss of sulphur from the slag decreases with increasing slag basicity. Although the average ARATES in Table 5.38 do not show the same trend, the sulphur losses to the atmosphere, expressed as percentages of the sulphur inputs, confirms the observations of the above authors. Table 5.38 shows that about 49%, 22% and 18% of sulphur input is lost to the atmosphere for slags containing 5%, 10% and 20% CaO respectively. This observation is easy to understand from equation (5.10) knowing that the oxygen ion activity in the slag increases with the CaO content of the slag.

Cooper and Kay(87) also report substantial sulphur loss to the atmosphere when remelting in air. However, they observe increasing sulphur losses with increasing slag basicity, which they explain in terms of the kinetics of the above reaction. They suggest that in atmospheres of high oxygen potential sulphur oxidation is controlled by the rate of sulphide ion arrival at the slag-gas interface, high slag sulphur contents being obtained with slags of high basicity.

Another evidence of the validity of equation (5.10) comes from the observations of various authors(1,79,88) that desulphurization is greatly reduced when remelting under argon. Cooper and Kay(87) also report negligible sulphur loss when remelting in a $CO/CO_2 = 99:1$ atmosphere, but they find little difference between remelting in argon and remelting in air, contrary to the results of the other authors(1,79,88). This may be probably due to the use of commercial purity argon ($P_{O_2} \sim 0.1\ kNm^{-2}$) by Cooper and Kay.

Although no work was done during this investigation to evaluate the other important reaction at this interface, viz., the oxygen transfer by multivalent cations, some discussion of the same is included here for completeness and to demonstrate the conflicting requirements for sulphur removal in ESR. The oxidation of multivalent cations in the slag at the slag-atmosphere interface and their subsequent reduction at the slag-metal interfaces tends to "pump" oxygen into the metal thus reducing the desulphurization and cleanliness of the metal. An example of such a pair of cyclic reactions is:

$$2(Fe^{2+}) + 1/2\ O_{2(g)} = 2(Fe^{3+}) + (O^{2-}) \qquad (5.11)$$

$$2(Fe^{3+}) + (O^{2-}) = 2(Fe^{2+}) + [O] \qquad (5.12)$$

Other transition elements with variable valancy such as Mn, Cr, Ti, etc., could also take part in similar reactions. This can be reduced by either minimizing the amounts of such oxides present in the slag or by reducing the oxygen partial pressure in the gas phase. The second alternative can be seen to be in conflict with the previous consideration of sulphur oxidation from the slag. Thus, good desulphurization without a sacrifice of cleanliness can be obtained generally by melting with highly basic slags under neutral or reducing atmospheres.

5.10.3 Site Three: The Electrode Tip-Slag Interface

As mentioned in Section 5.6 and as can be seen from Table 5.39, the electrode tip-slag interface is the dominant slag-metal reaction site during AC ESR. Table 5.39 shows that the major portion of the sulphur input into the system, at any moment, is removed from the metal into the slag at this interface. The maximum value of ERATE, expressed as percent of rate of sulphur input, during this investigation was about 89% in melt 24 (20% CaO) while the minimum was at least 50.5% at the end of the melt 21 (10% CaO). These values were much larger than the corresponding values of PRATE obtained. In fact, except for melt 21, resulphurization took place at the pool between the 15 - 20 kg remelted ingot level. Thus, the results of this investigation clearly establish the electrode tip-slag interface as the most important slag-metal reaction site for desulphurization in ESR, in contrast to the earlier belief that the pool-slag interface was the dominant reaction site(1,19).

The extent of slag-metal reactions taking place at any site depends mainly on two factors: the reaction rate and the residence time of molten metal at that site. The reaction rate depends on the chemical (or electrochemical) potential difference, the temperature and the geometry, such as, surface area to volume ratio, etc.

At the electrode tip a very thin layer of liquid metal is in contact with the slag, giving a large slag-metal surface area to volume ratio and short diffusion distances. As the current density is higher, the interfacial potential drop at the electrode tip would be expected to be larger than that at the pool-slag interface, resulting in greater heat generation at the electrode tip. This, coupled with the fact that heat conduction away from the pool may be greater, would indicate the existence of higher (local) temperatures at the electrode tip than at the pool-slag interface. Finally, the sulphur concentration of the electrode is generally larger than that of the pool and hence a greater driving force, in terms of a chemical potential difference, exists at the electrode tip. All these factors favour much higher reaction rates at the electrode tip-slag interface.

An appreciable residence time is expected at the electrode tip from the calculation of Holzgruber et al.(11). Assuming a liquid metal layer thickness of approximately 1 mm, Holzgruber et al. estimated the residence time of liquid metal at the electrode tip to be between 3 and 7 seconds for 12" - 32" ingots, depending on electrode diameter and melt rate. Therefore, most of the desulphurization and deoxidation can be expected to take place at the electrode tip-slag interface in the case of AC ESR. As discussed in Section 3.3 under certain conditions in DC ESR the reverse may be true.

As can be seen from Figures 5.14 to 5.16 or Table 5.39, ERATES decrease with time except for melt 25 (5% CaO). This can be easily understood from the sulphur-oxygen exchange reaction given by equation (3.6):

$$[S]_{1\ wt.\%} + (O^{2-}) = (S^{2-}) + [O]_{1\ wt.\%} \qquad (3.6)$$

As more and more sulphur accumulates in the slag (Figures 5.7 and 5.10), the activity of sulphide ion increases while that of oxide ion decreases due to depletion of the initial CaO in the slag. Also as the melt progresses more and more electrode scale dissolves in the slag with a corresponding increase in the oxygen level of the metal as given by equation (3.4). Thus, the driving force for the above exchange reaction reduces with time, resulting in a drop in ERATE with time.

The reverse effect shown in melt 25 (5% CaO) may be partly explained by the large values of ARATE found for that melt. As the sulphur in melt 25 is lost to the atmosphere at almost the same rate as the sulphur input to the slag, the slag sulphur remains almost constant (see Figure 5.13) and CaO is regenerated by reaction (5.10). Hence, ERATE should at least remain constant with time; however, the experimentally observed increase with time cannot be satisfactorily explained.

5.10.4 Site Four: The Droplet-Slag Interface

It is estimated that the metal droplet after being detached from the electrode tip passes through the slag within 0.01 - 0.1 of a second in ESR(11). Hence, it is thought that the residence time is too short for any chemical reaction to take place to any great extent. Whittaker(34) comes to the same conclusion in his DC melts.

Thus, the droplet-slag interface is not considered an important reaction site and, as stated in Section 3.5, it has been assumed that the metal composition remains unchanged during the droplet's fall through the slag bath. It has also been assumed that there is little desulphurization taking place during droplet sampling; this is confirmed by the analysis of a well-formed droplet which was present on the electrode tip at the end of melt 21. Analysis of material from this solid sessile droplet gave 0.069 wt.% S, a value consistent with the sulphur contents of the droplet samples given in Figure 5.6.

5.10.5 Site Five: The Metal Pool-Slag Interface

On the basis of small scale laboratory DC results, it was believed(1,19) that the metal pool-slag interface was the dominant reaction site in ESR. It was argued that the molten metal residence time in the pool was much greater than at the electrode tip and hence most of the desulphurization and deoxidation took place there. However, Holzgruber et al.(11) pointed out that although the liquid metal residence time in the pool can be estimated as between 10 and 60 minutes for ingots up to 32 inches in diameter, slag-metal reactions occur at this site only to a limited extent. This is based on the argument that the reaction rate at this interface can be expected to be much smaller for these following reasons:

(a) The metal pool temperature is appreciably lower than the electrode tip temperature (see Section 5.10.3). In fact, Holzgruber et al.(11) contend that the metal pool temperatures do not significantly exceed the liquidus temperature of the metal. Thus, in melting ferrous alloys, pool temperatures around 1500°C are expected. This is in agreement with the conclusions of Cooper and Kay(87).

(b) If sulphur is removed at the electrode tip, the driving force, and hence the rate of that reaction is correspondingly reduced at the metal pool-slag interface.

(c) Geometrical factors, such as surface area per unit volume, etc., are not favourable at this site.

For the AISI C 1117 grade of steel used, the liquidus temperature is expected to be around 1520° - 1522°C. From Section 5.8 it can be seen that pool temperatures close to 1500°C are in good agreement with the data. As also indicated in that section, small values for PRATE are obtained because of the proximity to equilibrium at that interface. The negative values of PRATE are difficult to explain when the values of ERATE are positive, unless the difference in temperature a at the two sites are taken into consideration. It can be seen from Table 5.37 that at the lower temperature the equilibrium metal sulphur concentration is higher and hence a reversion can take place.

With the exception of melt 25 (5% CaO), the values of PRATE can be seen to increase with time. This is expected from the increasing rate of sulphur input to the metal pool from the droplets as the values of ERATE decrease with time. The sulphur in the pool also increases by rejection at the ingot-pool interface. As can be seen from Table 5.39, this quantity could become quite large in some melts. Hence, the values of PRATE increase with time, and at the end of melt 21 it can be seen to be as large as 20% of the rate of sulphur input. In melt 25, PRATE can be seen to decrease with time corresponding to a reduction in the rate of sulphur input to the pool as indicated by an increasing ERATE.

In any case, the rate of sulphur transfer at this interface is quite small compared to that at the electrode tip-slag interface and hence this interface is not considered important as far as desulphurization in AC ESR is concerned. In fact the resulphurization taking place in melts 24 and 25 is seen to appreciably reduce the total desulphurization.

5.10.6 Site Six: The Metal Pool-Ingot Interface

From Tables 5.35 and 5.39 it can be seen that this interface is quite important as far as sulphur transfer in ESR is concerned. Except in melt 24 (20% CaO) the rate of sulphur transfer at this interface is appreciable. For example, in melt 21 (10% CaO) it is as high as 26% of the rate of sulphur input. In the case of melt 24, because of the low level of pool sulphur obtained and because of the high solidification rate the rate of sulphur rejected from this interface is low.

The refinement of the metal taking place at this interface is very similar to zone refining. In general, this can be an important site expecially for those alloying elements which have equilibrium distribution coefficients, K_x^*, much smaller than unity, e.g., sulphur, oxygen, etc. The effective distribution coefficient, K_x, which is the ratio of concentration of solute x in the solid to the concentration of the same solute in the liquid at a finite velocity of solidification, u, is given by:

$$K_x = \frac{K_x^*}{K_x^* + (1-K_x^*)\, e^{-u\delta/D_x}} \qquad (5.13)$$

where D_x is the diffusion coefficient of the alloying element x and δ is the thickness of the diffusion layer. Equation (5.13) is obtained for planar unidirectional solidification under steady-state conditions(100). From equation (5.13) it can be seen that for quench solidification, $u = \infty$, K_x equals unity, i.e., there is no segregation. However, at an infinitely slow rate of solidification ($u = 0$), i.e., under equilibrium conditions, $K_x = K_x^*$. The results of Nakagawa et al.(100) in the Fe-S system are given in Figure 5.17, as a plot of effective distribution coefficient K_S vs. solidification rate, u. There seems to be considerable scatter in their results but the points are contained within the curves calculated from equation (5.13) using $\delta/D_S = 1.6 \times 10^3$ and 3.8×10^3 s/cm. A value of 0.05 for K_S^* was used in these calculations. The dotted line with $\delta/D_S = 1.2 \times 10^3$ is reported to be used by Fischer et al.(10).

The estimated value of ingot sulphur, $[S]_I$, has been divided by that of pool, $[S]_P$, to obtain the effective distribution coefficient K_S at every 100 seconds, in Table 5.40. The average effective distribution coefficient and the solidification rate calculated by dividing the distance between two tungsten marks by the sampling time are also given in Table 5.40. It is obvious that the trend predicted by equation (5.13) is followed, i.e., the effective distribution coefficient increases with the velocity of solidification. However, the values of K_S obtained in this investigation can be seen to be much lower than those observed by Nakagawa et al.(100). This means that the δ/D_S value for the present experimental conditions is much smaller than those obtained by Nakagawa et al.(100) and Fischer et al.(101). This is not very surprising considering the vigorous stirring conditions existing in ESR, resulting in a much smaller value of δ compared to those of the above authors.

The rate of sulphur rejected at this interface depends not only on the value of the effective distribution coefficient, K_S, which is determined by the solidification rate but also on the actual level of sulphur in the pool. Thus, as the pool sulphur increases with time, the rate of transfer at this interface would increase, if the effective distribution coefficient remained approximately constant or decreased. As these conditions were satisfied in all the melts, the rate of sulphur rejected at this interface can be seen to increase with time in each case (see Table 5.35 and 5.39). Also, the lowest transfer rates are obtained for melt 24 (20% CaO) since it has the highest solidification rate and the lowest pool sulphur values. Quite the opposite is true for melt 21 (10% CaO).

5.11 Electrode Tip Profiles and Surface Areas

Table 5.41 gives the left and the right hand side electrode tip profiles for all the melts. The co-ordinate system used before in mapping pool profiles (see Figure 5.4) has been used again for tip profile measurements. The orders of the curves fitted to the profiles using a least square technique, are given in Table 5.42. The areas of the curved surfaces have been calculated from the tip profiles by the method described in Section 4.9.5 and are given in Table 5.42. The numbers in the third row are the average of the left and the right hand side surface areas. The depth of the cylindrical part of the electrode immersed in the slag has been found from the slag marks on the electrode after the melt. The areas of this portion are reported in Table 5.42. Total areas have been calculated by adding the average curved surface areas to the area of the cylindrical portion of the electrode immersed in the slag.

As can be seen from Table 5.42, the electrode tip surface areas do not vary very widely. There is a slight increase in area with increasing percentage of CaO in the slag and this trend can be explained on the basis of decreasing slag conductivity with increasing CaO content.

5.12 Slag Conductivity

One of the main reasons for the selection of CaF_2 as the major component of ESR slags is its high electrical conductivity. As almost the entire heat requirement of the process is supplied by the resistance heating of the slag bath, the conductivity of the slag is an important property.

For example, if the conductivity is so high that the slag bath resistance is of the same order as the rest of the circuit (i.e., power leads, electrode, etc.), the electrical efficiency would be very low since about half the power would be lost outside the furnace. On the other hand, if the conductivity is very low, not enough power can be generated at a reasonable voltage.

A discussion on the importance of slag conductivity in determining a melt rate at any particular power level is given in Section 5.2 above. At any particular current and voltage, the electrode to ingot gap and hence the power (or heat) distribution is determine by the slag conductivity. The heat distribution affects the melt rate, the pool size, the mode and direction of ingot solidification, surface finish, etc.

The conductivities of calcium fluoride based slags used in ESR have been determined by various authors$^{(29-36)}$. Fairly good reviews of published data on CaF_2-CaO-Al_2O_3 systems have been given by Duckworth et al.$^{(13)}$ and Mitchell et al.$^{(36)}$. To reduce the error due to polarization, AC bridges at high frequencies were used to determine the slag conductivities. For example, Mitchell et al.$^{(36)}$ found no detectable frequency dependence of cell resistance between 0.8 and 20 kHz and hence chose to use a 1 kHz bridge.

Figure 5.18 gives the plot of the logarithm of specific electrical conductivity, χ, vs. the reciprocal of absolute temperature for slags in the system CaF_2-CaO-Al_2O_3. The linearity of the $\log\chi$

against I/T plot probably indicates monoionic conduction. A sudden change in the slope of log χ vs. I/T plots occurs at the melting point (CaF_2 in Figure 5.18). This is probably due to a change in the mode of conduction. However, this effect has been used by Baak(29) and by Baak and Olander(60) to determine phase diagrams in the systems CaF_2-CaO and CaF_2-CaO-SiO_2 respectively. In these slags, the smaller and more mobile cations must be carrying the change and hence at constant temperature, the conductivity would depend on the concentration and mobility of these ions.

Duckworth and Hoyle(13) argue that the stronger the cation/anion affinity, the lower their mobility, and although oxygen and fluorine have similar ionic radii, oxygen ions carry a double charge and hence are attracted more strongly to the calcium ions than are the fluorine ions. Thus, the addition of lime reduces the mobility of the calcium ions and hence the electrical conductivity, as can be seen from Figure 5.18 and reference (36).

Figure 5.18 and reference (36) also show that the addition of Al_2O_3 markedly reduces the conductivity. This is due to the replacement of the more mobile Ca^{2+} ions by Al^{3+} ions. Also, Mitchell et al.(36) contend that the reduction in concentration of charge, carrying ions due to complex formation by the reaction:

$$Al_2O_3 + 4F^- \rightarrow AlO_2F_2^{3-} + AlOF_2^{1-} \quad (5.14)$$

is the cause for the substantial decrease in conductivity of CaF_2 slags on addition of Al_2O_3. Alumina containing slags are widely used in remelting high melting point ferrous alloys.

On comparison of published data(13,36) it becomes clear that considerable disagreement in the conductivity values exists even in the binary systems. The reasons for such disagreements are enumerated by Mitchell et al.(36).

The method of calculating slag conductivity at the line frequency of 60 Hz from the melt data given in Table 5.43 is described in Section 4.9.6. The densities at 1700°C for 10 and 20% CaO slags were estimated from the densities measured for those slags at 1450°C (see Table 3.4 of reference 13) and by applying an average temperature correction of 1×10^{-3} g/cm^3 - °C. An average density between pure CaF_2 and the 10% CaO-CaF_2 slag has been used for the 5% CaO slag. As indicated before, the slag conductivity has been calculated using the formulae (4.10) and (4.11). The various distances h_1, h_2 and L are shown in Figure 4.5.

The results are also given in Table 5.43. The resistivities of the slags from the literature are also quoted. It must be remembered that the experimental and literature values cannot be in agreement because of polarization effects at 60 Hz. The resistivity at 60 Hz is expected to be larger than the true resistivity at very high frequencies. From Table 5.43 this can be seen to be true, but the agreement is very good considering the approximations involved in the calculations.

Finally, it must be noted that in the above calculations it is assumed that the current paths are uniformly distributed in the slag phase. As the mould was insulated from the base-plate (see Section 4.2), no short circuit path via the mould to the base-plate is possible.

However, current paths from the slag, through the mould and back to the slag at a lower level, are possible. These paths would reduce the resistance of the slag bath but this effect is considered negligible because the solidified slag skin acts as an electrical insulator.

TABLE 5.1

General Information Concerning the Successful Melts

Melt No.	Wt.% CaO in Slag	Preset AC Voltage, V	AC Current A	Total Melt Time, S	Total Sampling Time, S	Weight of Ingot Melted kg	Weight of Slag Charged kg	Melt Rate g/s
21	10	30	2500	1800	870	20.879	3.760	11.6
24	20	30	2750	1500	600	20.550	3.580	13.7
25	5	30	2500	1955	665	21.115	3.700	10.8

Electrode Diameter (for all melts) = 7.62 cm.

Mould Diameter (for all melts) = 14.80 cm.

Electrode Material - AISI 1117 Carbon Steel

TABLE 5.2

Calculations of Actual Melt Rate from Weight of Ingot Melted and Melt Time

Melt No.	Weight of Starting Pad kg	Total Weight of Starting Pad + Ingot kg	Weight of Ingot kg	Total Time of Melt secs	Melt Rate g/s
21 (10% CaO)	5.221	26.100	20.879	1800	11.6
24 (20% CaO)	6.720	27.270	20.550	1500	13.7
25 (5% CaO)	6.260	27.375	21.115	1955	10.8

TABLE 5.3

Electrode Position as a Function of Time, Melt 21

Time, s	Electrode Position inches
0	31.8
255	29.0
545	26.0
688	25.0
790	24.0
905	23.0
1152	21.0
1260	20.0
1584	16.9
1674	16.0
1770	15.0

TABLE 5.4

Electrode Position as a Function of Time, Melt 24

Time, s	Electrode Position inches
0	58.2
225	56.0
338	54.0
467	53.0
778	49.0
865	48.0
900	47.6
955	47.0
1049	46.0
1142	45.0
1245	43.9
1433	41.9
1500	41.2

TABLE 5.5

Electrode Position as a Function of Time, Melt 25

Time, s	Electrode Position inches
0	35.8
425	32.0
538	31.0
767	29.0
1015	26.6
1178	25.5
1284	24.0
1400	23.0
1508	22.0
1620	21.0
1718	20.0
1815	19.0
1955	17.5

TABLE 5.6

Calculations of the Melt Rate from Electrode Descent Rate and Comparison With the Actual Melt Rate

elt. No.	Average Electrode Descent Rate, $R_E \times 10^2$ cm/s	Average Ingot Diameter D_I, cm	Melt Rate (Calculated from equation 4.1) g/s	Actual Melt Rate (from Ingot weight) g/s	Ratio of Actual Melt Rate to Electrode Descent Rate	Theoretical Ratio $\frac{\dot{m}}{R_E} = \frac{(D_I^2+D_E^2)}{D_I^2} \frac{\pi}{4} D_E^2 \rho_{Fe}$
21	2.294	14.25	10.59	11.6	5.06×10^2	4.615×10^2
24	2.74	14.26	12.65	13.7	5.0×10^2	4.615×10^2
25	2.401	14.29	11.07	10.8	4.5×10^2	4.612×10^2

Electrode Diameter (in all melts), D_E = 7.62 cm

Density of Metal, ρ_{Fe} = 7.87 (at 20°C)

TABLE 5.7

(a)

Initial Pool Profile Ingot 21 at 1.11 cm from the Centre

L.H.S.		R.H.S.	
X, inches	Y, cms	X, inches	Y, cms
0.0	0.0	0.0	0.0
0.25	4.29	0.25	3.81
0.50	5.24	0.50	4.29
0.75	6.03	0.75	5.08
1.0	6.35	1.0	5.56
1.25	6.51	1.25	5.87
1.5	6.99	1.50	6.67
		1.75	6.83
		1.875	6.69

TABLE 5.7

(b)

Final Pool Profile Ingot 21 at 1.11 cm from the Centre

L.H.S.		R.H.S.	
X, inches	Y, cms	X, inches	Y, cms
0.0	0.0	0.0	0.0
0.25	2.65	0.25	2.1
0.50	3.50	0.50	3.05
0.75	4.20	0.75	3.75
1.0	4.85	1.0	4.3
1.25	5.4	1.25	4.8
1.50	5.9	1.5	5.3
1.75	6.4	1.75	5.7
2.0	6.85	2.0	6.2
2.063	7.0	2.25	6.6
		2.5	7.06

TABLE 5.8

Tungsten Pool Profiles of Ingot 21 (corrected)

Initial Pool				Final Pool			
L.H.S.		R.H.S.		L.H.S.		R.H.S.	
X, cms	Y, cms	X, cms	Y, cms	X, cms	Y, cms	X, cms	Y, cms
0.0	0.0	0.0	0.0	0.0	0.0	0.0	0.0
0.01	1.11	0.01	1.11	0.02	1.11	0.02	1.11
0.645	4.431	0.645	3.968	0.655	2.873	0.655	2.375
1.28	5.356	1.28	4.431	1.29	3.672	1.29	3.246
1.915	6.131	1.915	5.2	1.925	4.344	1.925	3.911
2.55	6.446	2.55	5.67	2.56	4.975	2.56	4.441
3.185	6.604	3.185	5.974	3.195	5.513	3.195	4.927
3.82	7.078	3.82	6.762	3.83	6.004	3.83	5.415
		4.455	6.92	4.465	6.496	4.465	5.807
		4.773	7.078	5.1	6.939	5.1	6.299
				5.26	7.087	5.735	6.693
						6.370	7.147

TABLE 5.9

Tungsten Pool Profiles of Ingot 24

Initial Pool				Final Pool			
L.H.S.		R.H.S.		L.H.S.		R.H.S.	
X, cms	Y, cms	X, cms	Y, cms	X, cms	Y, cms	X, cms	Y, cms
0.0	0.0	0.0	0.0	0.0	0.0	0.0	0.0
0.5	3.2	0.5	2.25	0.5	2.05	0.5	2.05
1.0	3.95	1.0	3.3	1.0	3.0	1.0	3.4
1.5	4.75	1.5	4.15	1.5	3.75	1.5	4.35
2.0	5.05	2.0	4.85	2.0	4.45	2.0	4.95
2.5	5.4	2.5	5.4	2.5	4.95	2.5	5.45
3.0	5.85	3.0	5.75	3.0	5.35	3.0	5.7
3.5	6.3	3.5	6.1	3.5	5.7	3.5	6.2
4.0	6.6	4.0	6.45	4.0	6.1	4.0	6.4
4.5	6.95	4.5	6.8	4.5	6.4	4.5	6.7
4.8	7.06	5.0	7.06	5.0	6.6	5.0	6.85
				5.5	6.8	5.5	7.05
				6.0	6.95	6.0	7.15

TABLE 5.10

Tungsten Pool Profiles of Ingot 25

Initial Pool				Final Pool			
L.H.S.		R.H.S.		L.H.S.		R.H.S.	
X, cms	Y, cms	X, cms	Y, cms	X, cms	Y, cms	X, cms	Y, cms
0.0	0.0	0.0	0.0	0.0	0.0	0.0	0.0
0.5	1.9	0.5	2.8	0.5	2.1	0.5	3.2
1.0	2.9	1.0	4.1	1.0	3.4	1.0	3.9
1.5	3.6	1.5	4.8	1.5	4.3	1.5	4.4
2.0	4.3	2.0	5.5	2.0	4.9	2.0	4.9
2.5	4.8	2.5	5.8	2.5	5.3	2.5	5.3
3.0	5.3	3.0	6.1	3.0	5.7	3.0	5.6
3.5	5.7	3.5	6.3	3.5	6.0	3.5	5.9
4.0	6.2	4.0	6.45	4.0	6.4	4.0	6.2
4.5	6.6	4.5	6.7	4.5	6.7	4.5	6.6
5.0	7.1	5.0	7.0	5.0	7.1	5.0	6.8
		5.2	7.1			5.3	7.1

TABLE 5.11

Calculations of Average Initial Pool Volumes

Melt No. Description		21 (10% CaO)	24 (20% CaO)	25 (5% CaO)
Coefficients of 4th order curve fitted to tungsten pool profile (in ascending order of powers of x)	L.H.S.	1.1464 7.0501 -3.9460 1.0201 -0.09535	0.14024 7.0713 -3.9310 0.99411 -0.087567	0.71791 2.6615 -0.58749 0.080114 -0.003611
	R.H.S.	0.56208 6.9624 -4.0492 1.0591 -0.09585	0.073497 4.7823 -1.8130 0.36434 -0.027460	1.313 3.9341 -1.1851 0.16375 -0.0074627
Weighted sum of squares of residuals, cm^2	L.H.S.	0.10258	0.29321	0.02745
	R.H.S.	0.87755	0.07130	0.07869
Tungsten pool volumes, cm^3	L.H.S.	403.05	435.14	371.83
	R.H.S.	453.58	426.22	506.82
Excess pool volumes, cm^3	L.H.S.	0.0	478.0	69.4
	R.H.S.	0.0	440.0	48.0
Total pool volumes, cm^3	L.H.S.	403.05	913.14	441.23
	R.H.S.	453.58	866.22	554.82
Average pool volumes, cm^3		428.31	889.70	498.03

TABLE 5.12

Calculations of Average Final Pool Volumes

Description \ Melt No.		21 (10% CaO)	24 (20% CaO)	25 (5% CaO)
Coefficients of 4th order curve fitted to tungsten pool profile (in ascending order of powers of x)	L.H.S.	0.53459 4.3570 -1.8988 0.42375 -0.03340	0.10840 4.0301 -1.3361 0.23983 -0.016276	0.20718 4.5011 -1.5617 0.27706 -0.017935
	R.H.S.	0.51278 3.2248 -1.0574 0.18678 -0.011738	0.027601 4.6745 -1.5588 0.26497 -0.017030	2.3674 1.8509 -0.38173 0.046745 -0.0016943
Weighted sum of squares of residuals, cm^2	L.H.S.	0.61746	0.09933	0.02290
	R.H.S.	0.53978	0.03134	0.07823
Tungsten pool volumes, cm^3	L.H.S.	425.53	515.30	421.58
	R.H.S.	501.90	583.05	484.35
Excess pool volumes, cm^3	L.H.S.	16.0	150.0	91.2
	R.H.S.	236.6	150.0	115.2
Total pool volumes, cm^3	L.H.S.	441.53	665.3	512.78
	R.H.S.	738.50	733.05	599.55
Average pool volumes, cm^3		590.02	699.18	566.17

TABLE 5.13

Drop Sulphur, $[S]_D$, as a Function of Time, Melt 21

Time, s	Sulphur in Drop $[S]_D$, wt.%		Regressional Estimate of $[S]_D$, wt.%	95% Confidence Interval wt.% × 10^3
	Sample 1	Sample 2		
140	0.016	0.016	0.0144	± 8.01
248	0.016	0.017	0.0232	± 6.13
315	0.020	0.021	0.0286	± 5.15
385	0.040	0.041	0.0342	± 4.40
450	0.040	0.041	0.0395	± 4.06
518	0.053	0.053	0.0450	± 4.21
584	0.063	-----	0.0503	± 4.80
640	0.063	0.057	0.0548	± 5.52
687	0.061	0.059	0.0586	± 6.25
732	0.053	0.0415	0.0623	± 7.01

TABLE 5.14

Ingot Sulphur, $[S]_I$, as a Function of Time, Melt 21

Time, s	Ingot Sulphur $[S]_I$, wt.%	Regressional Estimate of $[S]_I$, wt.%	95% Confidence Interval wt.% x 10^3
61	0.011	0.0113	± 3.65
204	0.015	0.0135	± 2.77
340	0.012	0.0155	± 2.16
462	0.0195	0.0173	± 1.97
585	0.020	0.0192	± 2.22
707	0.021	0.0210	± 2.80
816	0.022	0.0227	± 3.45

TABLE 5.15

Pool Sulphur, $[S]_p$, as a Function of Time, Melt 21

Time, s	Pool Sulphur $[S]_p$, wt.%	Regressional Estimate of $[S]_p$, wt.%	95% Confidence Interval wt.% x 10^3
115	0.033	0.0360	± 6.38
162	0.039	0.0374	± 5.80
233	0.045	0.0397	± 5.00
373	0.044	0.0440	± 3.97
471	0.044	0.0471	± 3.91
574	0.048	0.0503	± 4.48
720	0.050	0.0549	± 6.02
808	0.064	0.0576	± 7.16

TABLE 5.16

Slag Sulphur, $(S)_S$, as a Function of Time, Melt 21

Time, s	Slag Sulphur $(S)_S$, wt.%	Regressional Estimate of $(S)_S$ wt.%	95% Confidence Interval wt.% × 10^2
98	0.31	0.271	± 3.69
182	0.25	0.298	± 3.12
322	0.34	0.341	± 2.35
340	0.33	0.347	± 2.28
414	0.38	0.370	± 2.08
499	0.42	0.397	± 2.08
668	0.45	0.449	± 2.73
748	0.47	0.474	± 3.23
838	0.50	0.502	± 3.85

TABLE 5.17

Results of Least Square Fit $y = A+Bx$ to all Sulphur Concentration-Time Data,* Melt 21

	Intercept, (A) wt.%	Slope, (B) wt.%/s	Variance $(wt.\%)^2$	Correlation Coefficient	Critical Correlation Coefficient
Drop Sulphur	3.110×10^{-3}	8.083×10^{-5}	7.0×10^{-5}	0.8888	0.4555
Ingot Sulphur	1.038×10^{-2}	1.507×10^{-5}	4.103×10^{-6}	0.9112	0.7545
Pool Sulphur	3.237×10^{-2}	3.125×10^{-5}	1.986×10^{-5}	0.8896	0.7067
Slag Sulphur	2.409×10^{-1}	3.120×10^{-4}	6.742×10^{-4}	0.9560	0.6664

TABLE 5.18

Drop Sulphur, $[S]_D$, as a Function of Time, Melt 24

Time, s	Drop Sulphur, $[S]_D$ wt.%		Regressional Estimate of $[S]_D$ wt.%	95% Confidence Interval wt.% x 10^3
	Sample 1	Sample 2		
96	0.013	-----	0.0140	± 6.11
170	0.018	0.016	0.0158	± 4.77
278	0.018	0.015	0.0185	± 3.39
387	0.025	0.018	0.0213	± 3.51
456	0.032	-----	0.0230	± 4.38
513	0.023	0.019	0.0244	± 5.35

TABLE 5.19

Ingot Sulphur, $[S]_I$, as a Function of Time, Melt 24

Time, s	Ingot Sulphur, $[S]_I$ wt.%	Regressional Estimate of $[S]_I$ wt.%	95% Confidence Interval wt.% x 10^3
12	0.008	0.0078	± 4.00
74	0.011	0.0094	± 3.40
141	0.010	0.0110	± 2.83
207	0.013	0.0127	± 2.39
273	0.015	0.0143	± 2.15
335	0.015	0.0159	± 2.17
406	0.017	0.0177	± 2.46
468	0.0167	0.0192	± 2.90
517	0.0164	0.0204	± 3.32
567	0.0280	0.0217	± 3.79

TABLE 5.20

Pool Sulphur, $[S]_P$, as a Function of Time, Melt 24

Time, s	Pool Sulphur, $[S]_P$ wt.%	Regressional Estimate of $[S]_P$ wt.%	95% Confidence Interval wt.% × 10^3
83	0.014	0.0129	± 8.51
110	0.010	0.0141	± 7.83
164	0.0135	0.0165	± 6.56
247	0.0226	0.0202	± 4.99
272	0.0214	0.0213	± 4.66
308	0.0226	0.0228	± 4.38
342	0.0214	0.0243	± 4.33
375	0.035	0.0258	± 4.51
399	0.042	0.0268	± 4.76
451	0.0227	0.0291	± 5.58
478	0.018	0.0303	± 6.12
525	0.032	0.0324	± 7.17
553	0.035	0.0336	± 7.84

TABLE 5.21

Slag Sulphur, $(S)_S$, as a Function of Time, Melt 24

Time, s	Slag Sulphur $(S)_S$ wt.%	Regressional Estimate of $(S)_S$ wt.%	95% Confidence Interval wt.% x 10^2
12	0.47	0.465	± 3.28
90	0.48	0.494	± 2.63
158	0.48	0.519	± 2.14
210	0.55	0.538	± 1.84
255	0.57	0.555	± 1.69
292	0.61	0.568	± 1.64
336	0.57	0.585	± 1.69
381	0.61	0.601	± 1.86
444	0.63	0.624	± 2.23
485	0.65	0.639	± 2.53
569	0.64	0.670	± 3.22

TABLE 5.22

Results of Least Square Fit y = A+Bx tc Sulphur Concentration-Time Data, Melt 24

	Intercept (A) wt.%	Slope (B) wt.%/s	Variance $(wt.\%)^2$	Correlation Coefficient	Critical Correlation Coefficient
Drop Sulphur	1.161×10^{-2}	2.492×10^{-5}	1.945×10^{-5}	0.6667	0.6319
Ingot Sulphur	7.528×10^{-3}	2.494×10^{-5}	8.502×10^{-6}	0.8659	0.6319
Pool Sulphur	9.290×10^{-3}	4.398×10^{-5}	5.015×10^{-5}	0.7032	0.5529
Slag Sulphur	4.611×10^{-1}	3.676×10^{-4}	5.781×10^{-4}	0.9400	0.6021

TABLE 5.23

Drop Sulphur, $[S]_D$, as a Function of Time, Melt 25

Time, s	Drop Sulphur, $[S]_D$ wt.%		Regressional Estimate of $[S]_D$ wt.%	95% Confidence interval wt.% x 10^3
	Sample 1	Sample 2		
161	0.028	0.026	0.0378	± 9.65
240	0.039	0.045	0.0343	± 7.65
316	0.035	0.028	0.0310	± 6.35
404	0.043	0.028	0.0271	± 6.15
550	0.019	-----	0.0206	± 8.82
643	0.012	0.011	0.0165	± 11.49

TABLE 5.24

Ingot Sulphur, $[S]_I$, as a Function of Time, Melt 25

Time, s	Ingot Sulphur $[S]_I$ wt.%	Regressional Estimate of $[S]_I$ wt.%	95% Confidence Interval wt.% x 10^3
57	0.025	0.0262	± 4.56
149	0.031	0.0284	± 3.53
247	0.027	0.0307	± 2.72
321	0.033	0.0324	± 2.50
401	0.037	0.0343	± 2.75
487	0.037	0.0363	± 3.45
591	0.037	0.0388	± 4.61

TABLE 5.25

Pool Sulphur, $[S]_P$, as a Function of Time, Melt 25

Time, s	Pool Sulphur $[S]_P$ wt.%	Regressional Estimate of $[S]_P$ wt.%	95% Confidence Interval wt.% X 10^3
97	0.052	0.0535	± 4.90
175	0.059	0.0571	± 3.90
256	0.055	0.0608	± 3.03
330	0.067	0.0642	± 2.51
367	0.066	0.0659	± 2.42
390	0.070	0.0670	± 2.43
452	0.071	0.0698	± 2.69
506	0.074	0.0722	± 3.15
563	0.076	0.0748	± 3.77
610	0.072	0.0770	± 4.35

TABLE 5.26

Slag Sulphur, $(S)_S$, as a Function of Time, Melt 25

Time, s	Slag Sulphur $(S)_S$ wt.%	Regressional Estimate of $(S)_S$ wt.%	95% Confidence Interval wt.% X 10^2
35	0.25	0.2527	± 3.23
89	0.26	0.2527	± 2.85
180	0.26	0.2527	± 2.27
250	0.26	0.2527	± 1.92
300	0.26	0.2527	± 1.75
381	0.20	0.2527	± 1.68
450	0.29	0.2528	± 1.84
494	0.23	0.2528	± 2.02
545	0.24	0.2528	± 2.29
583	0.26	0.2528	± 2.51
665	0.27	0.2528	± 3.07

TABLE 5.27

Results of Least Square Fit y = A+Bx to Sulphur Concentration-Time Data, Melt 25

	Intercept (A) wt.%	Slope (B) wt.%/s	Variance $(wt.\%)^2$	Correlation Coefficient	Critical Correlation
Drop Sulphur	4.492×10^{-2}	-4.416×10^{-5}	7.830×10^{-5}	-0.6800	0.6021
Ingot Sulphur	2.487×10^{-2}	2.348×10^{-5}	6.621×10^{-6}	0.8825	0.7545
Pool Sulphur	4.903×10^{-2}	4.583×10^{-5}	1.098×10^{-5}	0.9249	0.6319
Slag Sulphur	2.526×10^{-1}	2.491×10^{-7}	6.020×10^{-4}	0.0022	0.6021

TABLE 5.28

Electrode Sulphur Analysis

Description	Melt No.	Electrode 21	Electrode 24, 25
Sample Number	1	0.135	0.153
	2	0.138	0.151
	3	0.136	0.157
	4	0.135	0.156
Average Electrode Sulphur $[S]_E$, wt.%		0.136	0.154
Variance of $[S]_E$, $S^2_{[S]_E}$ $(\text{wt.}\%)^2$		2.0×10^{-6}	7.667×10^{-6}

TABLE 5.29

The Three Rates and Their Standard Errors, Melt 21

Time, s	ERATE, gms/sec × 10^2	Standard Error g/s × 10^4	FRATE g/s × 10^3	Standard Error g/s × 10^4	ARATE g/s × 10^3	Standard Error g/s × 10^3
50	1.495	-----	-1.997	-----	1.298	-----
100	1.448	4.283	-1.657	5.491	1.204	1.322
150	1.401	3.700	-1.315	5.019	1.174	1.322
200	1.354	3.117	-0.973	4.581	1.144	1.322
250	1.307	2.536	-0.629	4.187	1.116	1.321
300	1.260	1.958	-0.284	3.851	1.027	1.321
350	1.213	1.387	0.062	3.589	1.001	1.321
400	1.167	0.838	0.409	3.419	0.976	1.321
450	1.120	0.410	0.757	3.353	0.953	1.321
500	1.073	0.566	1.106	3.400	0.868	1.321
550	1.026	1.077	1.457	3.553	0.847	1.321
600	0.979	1.639	1.808	3.800	0.827	1.321
650	0.932	2.214	2.161	4.125	0.807	1.321
700	0.885	2.793	2.515	4.510	0.790	1.322
750	0.838	3.375	2.870	4.942	0.773	1.322
800	0.791	3.958	3.226	5.408	0.757	1.322
850	0.745	4.542	3.583	5.902	0.680	1.322

TABLE 5.30

The Three Rates and Their Standard Errors, Melt 24

Time, s	ERATE, g/s $\times 10^2$	Standard Error g/s $\times 10^4$	PRATE g/s $\times 10^3$	Standard Error g/s $\times 10^4$	ARATE g/s $\times 10^3$	Standard Error g/s $\times 10^3$
100	1.917	3.262	-1.593	8.527	5.478	1.563
150	1.900	2.646	-1.493	8.249	5.491	1.563
200	1.882	2.068	-1.397	8.035	5.572	1.563
250	1.865	1.568	-1.307	7.893	5.649	1.563
300	1.848	1.245	-1.220	7.824	5.722	1.563
350	1.831	1.247	-1.139	7.832	5.790	1.563
400	1.814	1.571	-1.062	7.916	5.853	1.563
450	1.797	2.072	-0.989	8.074	5.838	1.563
500	1.780	2.651	-0.922	8.301	5.892	1.563
550	1.763	3.267	-0.859	8.592	5.941	1.563
600	1.746	3.903	-0.800	8.941	5.985	1.564

TABLE 5.31

The Three Rates and Their Standard Errors, Melt 25

Time, s	ERATE, g/s $\times 10^2$	Standard Error g/s $\times 10^4$	PRATE g/s $\times 10^3$	Standard Error g/s $\times 10^4$	ARATE g/s $\times 10^2$	Standard Error g/s $\times 10^3$
100	1.226	4.727	-0.666	6.146	1.174	1.323
150	1.250	3.890	-1.053	5.478	1.159	1.323
200	1.273	3.061	-1.439	4.889	1.144	1.323
250	1.297	2.256	-1.822	4.409	1.130	1.322
300	1.321	1.509	-2.205	4.079	1.115	1.322
350	1.345	0.965	-2.587	3.935	1.101	1.322
400	1.369	1.028	-2.968	3.998	1.087	1.322
450	1.393	1.629	-3.348	4.258	1.073	1.322
500	1.417	2.391	-3.726	4.684	1.059	1.323
550	1.440	3.202	-4.108	5.234	1.045	1.323
600	1.464	4.032	-4.480	5.874	1.031	1.323
650	1.488	4.871	-4.855	6.578	1.017	1.323

TABLE 5.32

The Three Rates and Their Confidence Intervals as a Function of Weight of Electrode Melted, Melt 21

Time, s	Weight Melted kg	ERATE g/s × 10^3	Confidence Interval, g/s × 10^3	PRATE g/s × 10^3	Confidence Interval, g/s × 10^3	ARATE g/s × 10^3	Confidence Interval, g/s × 10^3
400	0.429	11.665	± 0.168	0.409	± 0.684	0.976	±2.64
450	1.009	11.196	± 0.082	0.757	± 0.670	0.953	±2.64
500	1.589	10.727	± 0.113	1.106	± 0.680	0.868	±2.64
550	2.169	10.258	± 0.216	1.457	± 0.710	0.847	±2.64
600	2.749	9.790	± 0.328	1.808	± 0.760	0.827	±2.64
650	3.329	9.321	± 0.442	2.161	± 0.824	0.808	±2.64
700	3.909	8.852	± 0.558	2.515	± 0.902	0.790	±2.64
750	4.489	8.383	± 0.676	2.870	± 0.988	0.773	±2.64

Slag Composition - 10% CaO (Melt 21)

$T_{15\ kg}$ = 363 sec, $T_{20\ kg}$ = 794 sec, $\dot{m}$ = 11.6 g/s

$[S]_E$ = 0.136%

TABLE 5.33

The Three Rates and Their Confidence Intervals, as a Function of Weight of Electrode Melted, Melt 24

Time, s	Weight Melted kg	ERATE g/s × 10^3	Confidence Interval g/s × 10^3	PRATE g/s × 10^3	Confidence Interval g/s × 10^3	ARATE g/s × 10^3	Confidence Interval g/s × 10^3
200	0.068	18.825	± 0.41	-1.397	± 1.61	5.572	± 3.12
250	0.784	18.654	± 0.31	-1.307	± 1.58	5.649	± 3.12
300	1.434	18.483	± 0.25	-1.220	± 1.56	5.722	± 3.12
350	2.124	18.313	± 0.25	-1.139	± 1.57	5.790	± 3.12
400	2.809	18.142	± 0.31	-1.062	± 1.58	5.853	± 3.12
450	3.494	17.971	± 0.41	-0.989	± 1.61	5.838	± 3.12
500	4.179	17.800	± 0.53	-0.922	± 1.66	5.892	± 3.12
550	4.864	17.630	± 0.65	-0.859	± 1.72	5.941	± 3.12

Slag Composition = 20% CaO (Melt 24)

$T_{15\ kg}$ = 195 sec, $T_{20\ kg}$ = 560 sec

$\dot{m}$ = 13.7 g/sec

$[S]_E$ = 0.154%

TABLE 5.34

The Three Rates and Their Confidence Intervals, as a Function of Weight of Electrode Melted, Melt 25

Time, s	Weight Melted kg	ERATE g/s × 10^3	Confidence Interval g/s × 10^3	PRATE g/s × 10^3	Confidence Interval g/s × 10^3	ARATE g/s × 10^3	Confidence Interval g/s × 10^2
100	0.011	12.258	± 0.95	-0.667	± 1.23	11.738	± 0.26
150	0.551	12.496	± 0.78	-1.053	± 1.10	11.590	± 0.26
200	1.091	12.734	± 0.61	-1.438	± 0.98	11.443	± 0.26
250	1.631	12.973	± 0.45	-1.822	± 0.88	11.298	± 0.26
300	2.171	13.211	± 0.30	-2.205	± 0.81	11.153	± 0.26
350	2.711	13.450	± 0.19	-2.587	± 0.79	11.010	± 0.26
400	3.251	13.688	± 0.21	-2.968	± 0.80	10.867	± 0.26
450	3.791	13.927	± 0.33	-3.348	± 0.85	10.726	± 0.26
500	4.331	14.165	± 0.48	-3.726	± 0.94	10.586	± 0.26
550	4.871	14.404	± 0.64	-4.104	± 1.05	10.447	± 0.26

Slag Composition = 5% CaO (Melt 25)

$T_{15\ kg}$ = 99 sec, $T_{20\ kg}$ = 562 sec, $\dot{m}$ = 10.8 g/s

$[S]_E$ = 0.154%

TABLE 5.35

Calculations of Rate of Sulphur Transfer at Ingot-Pool Interface

% CaO in Slag		Time, s	$[S]_P$, wt.%	$[S]_l$, wt.%	$\Delta[S]$, wt.%	Instantaneous Freezing Rate $\hat{f}$, g/s	Rate at Ingot-Pool Interface g/s × 10^3
20% (M24)	T_{15}	195	0.0179	0.0124	0.0055	12.19	0.67
	T_{20}	560	0.0339	0.0215	0.0124	13.55	1.68
10% (M21)	T_{15}	363	0.0437	0.0159	0.0278	12.36	3.44
	T_{20}	794	0.0572	0.0224	0.0348	11.71	4.08
5% (M25)	T_{15}	99	0.0535	0.0272	0.0263	11.41	3.00
	T_{20}	562	0.0748	0.0381	0.0367	10.91	4.00

TABLE 5.36

Electrode and Ingot Oxygen Analysis

Description		Oxygen Content, wt.%			Average Oxygen in Whole Ingot wt.%
		Sample 1	Sample 2	Average	
Ingot 21 (10% CaO)	Top	0.0103	0.0115	0.0109	0.0108
	Middle	0.0125	0.0115	0.0120	
	Bottom	0.0114	0.0077	0.0095	
Ingot 24 (20% CaO)	Top	0.0121	0.0096	0.01085	0.0116
	Middle	0.0107	0.0113	0.0110	
	Bottom	0.0116	0.0141	0.01285	
Electrode 21		0.0338	0.0359	0.0349	0.0349
Electrodes 24,25		0.0377	0.0361	0.0369	0.0369

<u>TABLE 5.37</u>

Comparison of Equilibrium and Actual Pool Sulphur Concentration

Temperature °K	CaO in Slag wt.%	C'_S	$C^*_S = \frac{C'_S}{K}$	Slag Sulphur Concentration wt.%	Ingot Oxygen Concentration wt.%	Equilibrium Pool Sulphur Concentration wt.%	Actual Pool Sulphur Concentration wt.%
1773°K	10% (M21)	1.23×10^{-2}	0.911×10^{-1}	0.377	0.0108	0.0447	0.0465
	20% (M24)	3.04×10^{-2}	2.252×10^{-1}	0.571	0.0116	0.0294	0.0225
1973°K	10% (M21)	2.23×10^{-2}	1.232×10^{-1}	0.377	0.0108	0.0331	0.0465
	20% (M24)	5.50×10^{-2}	3.039×10^{-1}	0.571	0.0116	0.0218	0.0225

TABLE 5.38

Overall Sulphur Balance and Average Rates

% CaO in Slag Description			20% (M24)	10% (M21)	5% (M25)
Sulphur Input, g (from Electrode Only)			31.60	28.40	32.52
SULPHUR OUTPUT, g	Ingot	Total Sulphur, g	4.68	4.71	7.05
		% of Input	14.81	16.58	21.69
	Slag Cap	Total Sulphur, g	20.76	17.13	9.29
		% of Input	65.70	60.32	28.57
	Slag Skin	Total Sulphur, g	0.44	0.40	0.20
		% of Input	1.39	1.41	0.62
Sulphur Lost to Atmosphere		Total Sulphur, g	5.72	6.16	15.98
		% of Input	18.10	21.69	49.14
Average ARATE from Sulphur balance $g/s \times 10^3$			3.81	3.42	8.17
Average rate of Metal Desulphurization Average ERATE + PRATE, g/s			17.95	13.16	13.03

TABLE 5.39

Different Rates as Percentage of Rate of Sulphur Input

Description \ % CaO in Slag		20% (M24)		10% (M21)		5% (M25)	
		T_{15}	T_{20}	T_{15}	T_{20}	T_{15}	T_{20}
Rate of sulphur input, g of sulphur/s x 10^3 $\dot{m}$. $[S]_E/100$		21.10	21.10	15.776	15.776	16.63	16.63
ERATE	Actual value g/s x 10^3	18.84	17.60	12.01	7.97	12.26	14.46
	% of sulphur input	89.29	83.41	76.12	50.52	73.72	86.95
PRATE	Actual value g/s x 10^3	- 1.407	- 0.847	0.152	3.183	- 0.666	- 4.197
	% of sulphur input	- 6.67	- 4.01	0.96	20.18	- 4.03	-25.26
Rate of metal desulphurization (= ERATE+PRATE)	Actual value g/s x 10^3	17.43	16.75	12.162	11.153	11.59	10.26
	% of sulphur input	82.62	79.40	77.08	70.70	68.69	61.69
ARATE	Actual value g/s x 10^3	5.564	5.950	0.994	0.759	11.74	10.42
	% of sulphur input	26.37	28.20	6.30	4.81	70.60	62.66
S transfer rate at ingot-pool interface	Actual value g/s x 10^3	0.67	1.68	3.44	4.08	3.00	4.00
	% of sulphur input	3.17	7.96	21.81	25.86	18.04	24.05

TABLE 5.40

Effective Sulphur Distribution Coefficients Calculated from Pool and Ingot Sulphur Concentrations

Time, s	20% CaO (M24)			10% CaO (M21)			5% CaO (M25)		
	$[S]_l$, wt.%	$[S]_p$, wt.%	$K_S = \frac{[S]_l}{[S]_p}$	$[S]_l$, wt.%	$[S]_p$, wt.%	$K_S = \frac{[S]_l}{[S]_p}$	$[S]_l$, wt.%	$[S]_p$, wt.%	$K_S = \frac{[S]_l}{[S]_p}$
100	0.010	0.014	0.71	0.012	0.0355	0.34	0.0275	0.0537	0.51
200	0.0125	0.018	0.69	0.0134	0.0385	0.35	0.0298	0.058	0.51
300	0.0150	0.0225	0.67	0.015	0.042	0.36	0.032	0.063	0.51
400	0.0175	0.027	0.65	0.0164	0.045	0.365	0.0344	0.0675	0.51
500	0.020	0.0315	0.63	0.018	0.048	0.375	0.037	0.072	0.51
600	0.0225	0.036	0.625	0.0194	0.051	0.38	0.0388	0.0765	0.51
700				0.0210	0.0545	0.385			
800				0.023	0.0575	0.40			
Average Effective Distribution Coeff.	0.663			0.370			0.510		
Solidification Rate, cm/s	1.21×10^{-2}			5.75×10^{-3}			8.72×10^{-3}		

TABLE 5.41

Electrode Tip Profiles

Melt 21 (10% CaO)				Melt 24 (20% CaO)				Melt 25 (5% CaO)			
L.H.S.		R.H.S.		L.H.S.		R.H.S.		L.H.S.		R.H.S.	
X, cm	Y, cm	X, cm	Y, cm	X, cm	Y, cm	X, cm	Y, cm	X, cm	Y, cm	X, cm	Y, cm
0.0	0.0	0.0	0.0	0.0	0.0	0.0	0.0	0.0	0.0	0.0	0.0
0.2	1.0	0.2	0.85	0.2	0.65	0.2	0.6	0.2	1.5	0.2	1.35
0.4	1.6	0.4	1.70	0.4	1.40	0.4	1.2	0.4	2.50	0.4	1.95
0.6	2.05	0.6	2.35	0.6	1.90	0.6	1.75	0.6	3.05	0.6	2.45
0.8	2.45	0.8	2.85	0.8	2.55	0.8	2.30	0.8	3.45	0.8	2.80
1.0	2.85	1.0	3.30	1.0	3.10	1.0	2.85	1.0	3.65	1.0	3.20
1.2	3.20	1.2	3.60	1.2	3.60	1.2	3.25	1.2	3.80	1.2	3.50
1.4	3.55	1.4	3.80	1.3	3.80	1.4	3.65			1.5	3.80
1.6	3.80					1.5	3.80				

TABLE 5.42

Electrode Tip Surface Areas

Description \ Melt No.		21 (10% CaO)	24 (20% CaO)	25 (5% CaO)
Order of the Curve Fitted (by Least Square)	L.H.S.	3	2	3
	R.H.S.	3	2	3
Area of the Curved Surface cm^2	L.H.S.	51.82	55.84	51.96
	R.H.S.	50.92	59.98	52.78
Average Area of the Curved Surface, cm^2		51.37	57.91	52.37
Depth of Cylindrical Electrode Immersed, cm		1.04	0.92	0.77
Area of Cylindrical Electrode Immersed, cm^2		24.90	22.02	18.43
Total Surface Area of Electrode Tip, cm^2		76.27	79.93	70.80

TABLE 5.43

Calculations of Slag Conductivities

Description \ % CaO in Slag	20% (M24)	10% (M21)	5% (M25)
Estimated density at 1700°C, g/cm^3	2.38	2.32	2.29
Weight of slag cap, g	3244	3426	3442
Volume of slag, cm^3	1363	1476.7	1503
Height of slag, h_S, cm	7.92	8.58	8.74
Height of cylindrical electrode immersed, h_i, cm	0.92	1.04	0.77
Average height of the curved electrode tip, h_2, cm	1.40	1.50	1.35
Average distance between electrodes, cm $L = h_S - (h_1+h_2)/2$	6.76	7.31	7.68
Resistance of slag bath $R = V/I$, ohms	1.091×10^{-2}	1.20×10^{-2}	1.20×10^{-2}
Average area of electrodes, A, cm^2	119.75	117.95	115.2
Conductivity, $\chi = L/RA$ ohm^{-1} cm^{-1}	5.17	5.17	5.56
Resistivity $\rho = 1/\chi$ ohm - cm	0.193	0.193	0.180
Resistivity at 1700°C ohm-cm	0.188 0.148 (50)	0.150 (52) 0.127 (at 1600°C) (50) 0.136 (49)	0.149 (52)

CHAPTER VI

SUMMARY

Conventional overall sulphur balances are inadequate for the determination of the dominant slag-metal reaction site in ESR. However, in DC ESR an indication of the dominant reaction site can be indirectly obtained by such sulphur balances. A review of the literature shows that no consensus of opinion exists as to which of the three slag-metal interfaces is the most important in DC ESR.

In this investigation, the dominant reaction site in AC remelting is directly determined by separately obtaining the rate of sulphur transfer at the electrode tip/slag and metal pool/slag interfaces. A method of droplet sampling, using a graphite spoon, was developed and, knowing all the pertinent sulphur concentrations, the rates at the two slag-metal interfaces were found. In this analysis it is assumed that virtually no sulphur transfer takes place at the droplet/slag interface during the droplet's quick transition through the slag. Experimental evidence in support of this assumption has been obtained.

The results of melts using CaF_2-based slags with varying CaO contents indicate that in AC ESR the electrode tip/slag interface is the dominant slag-metal reaction site. The sulphur transfer rates at this interface are far in excess of those at the pool/slag interface; in fact, in two melts, resulphurization took place at the pool/slag interface. Equilibrium calculations based on data given in the literature indicate that the sulphur in the pool is close to equilibrium with the slag.

Calculations of the rate of sulphur lost from the slag to the atmosphere indicate the importance of this site in ESR, especially when melting with slags of low lime content. With a 5% CaO slag this rate was found to be as high as 70% of the rate of sulphur input into the system. The total rate of metal desulphurization in this melt is approximately the same as the rate of loss of sulphur to the atmosphere.

Conventional overall sulphur balances have been carried out and the results are consistent with the above analysis. The conductivities of the slags at 60 Hz were calculated from the melt data and they are in quite good agreement with literature values.

The rate of sulphur rejected at the metal pool/ingot interface has been calculated and it is shown that this could be important in melts with low freezing rates.

The melt rate was found to increase with increasing slag lime content which is explained on the basis of variations in slag conductivities. The melt rate calculated from the electrode descent rate was found to be within 10% of the actual value.

REFERENCES

1. B. I. Medovar et al., "Electroslag Remelting", Moscow, 1963; Joint Publications Research Service, U.S. Dept. of Commerce, #22,217, Dec. 10, 1963.
2. United States Patent 2,191,479: Feb. 27, 1940, Manufacture of Alloy Ingots, R.K. Hopkins, assignor to M.W. Kellogg Company.
3. A. C. Williams, Iron and Steel Institute, London, Special Report #77, "Clean Steels", p. 79 (1963).
4. A. C. Williams, J.I.S.I., 202 (7), p. 581 (1964).
5. N. Robinson and J. A. Grainger, Metallurgia, 67 (4), p. 161 (1963).
6. Anon., Journal of Metals, 18 (2), p. 165 (1966).
7. G. Hoyle et al., "Electro-Slag Refining Technology", BISRA Open Report, MG/A/416/66, (1966).
8. B. I. Medovar et al., Stal in English, No. 2, p. 114 (1966).
9. W. A. McKeen et al., Metal Progress, 82 (9), 116, 118, 120, 123 (1962).
10. A. C. Williams, BISRA Report, MG/A/74/64, (1964).
11. W. Holzgruber et al., Trans. Vac. Met. Conf., 1968, p. 499, (R.B. Barrow and A. Simkovich, Ed.).
12. W. Holzgruber et al., Trans. Vac. Met. Conf., 1969, p. 415 (D.T. Bourgette and A. Simkovich, Ed.).
13. W. E. Duckworth and G. Hoyle, "Electro-Slag Refining", Chapman & Hall, Pub., London, 1969.
14. W. E. Duckworth and P. J. Wooding, Trans. Vac. Met. Conf., 1968, p. 479 (Barrow et al., Ed.).
15. H. Yuan-Sun et al., Acta Met. Sinica, 7, p. 24 (1964).

16. G. J. W. Kor and F. D. Richardson, Trans. Met. Soc. AIME, 245 (2), p. 319 (1969).

17. D. M. Edmunds and J. Taylor, J.I.S.I., 210 (4), p. 280 (1972).

18. J. Hlineny et al., Sb. Ved. Praci Vysoke Skoly Banske Ostrave, 11, (3), p. 499 (1965).

19. D. A. Whittaker, Ph.D. Thesis, McMaster University, Hamilton (1967).

20. H. Kusamichi et al., as quoted in reference (12).

21. D. A. R. Kay, A. Mitchell and M. Ram, J.I.S.I., 208, (2), p. 141 (1970).

22. M. W. Davies et al., BISRA Open Report, C/63/68 (1968).

23. I. D. Sommerville and D. A. R. Kay, Met. Trans., 2, (6), p. 1727 (1971).

24. A. Mitchell, J. Vac. Sci. Technol., 7, (6), p. S63 (1970).

25. A. Mitchell and M. Bell, J.I.S.I., 209, (8), p. 658 (1971).

26. Yu. V. Latash and B. I. Medovar, Tsvetnye Met., No. 12, p. 75 (1966).

27. M. W. Davies, "The Chemical and Physical Properties of Fluoride-Based Slags", BISRA Report No. MG/A/35/67 (1967).

28. M. W. Davies, "The Chemistry of CaF_2-Based Slags", paper presented at Int. Symposium on Met. Chem. Applications in Ferrous Met., July, 1971.

29. T. Baak, Acta Chem. Scand., 8 (9), p. 1727 (1954).

30. V. N. Kolisnyk, Automatic Welding, (4), p. 9 (1964).

31. B. E. Lopaev et al., Automatic Welding, (1), p. 31, (1966).

32. R. Kammel and H. Winterhager, Erzmetall., 21, p. 399 (1968).

33. P. P. Evseev, Automatic Welding, 11, p. 42 (1967).

34. G. I. Zmoidin, Izv. A N SSSR Metal., 3, p. 69 (1970).

35. I. Chmelar et al., Sbornik VSB Ostrave Rada Hutnicka, 13, p. 75 (1967); (BISITS 7712, Dec. 1969).

36. A. Mitchell and J. Cameron, Met. Trans., 2, p. 3361 (1971).

37. P. N. Smith and M. W. Davies, Trans. Inst. Min. Met. (Section C), 80, p. C87 (1971).

38. M. W. Davies and F. A. Wright, Chem. Ind., p. 359 (1970).

39. L. A. Gerasimenko, Avt. Svarka, 16, p. 77 (1963).

40. V. V. Stepanov et al., ibid, p. 1128 (1965).

41. P. P. Evseev and A. F. Filippov, Izv. VUZ Chern. Met., 8 (3), p. 70 (1965).

42. V. K. Kulifeev et al., Izv. VUZ Tsvet. Met., 11 (2), p. 116 (1968).

43. G. I. Zhmoidin, Izv. A N SSSR, Metal., (6), p. 9 (1969).

44. G. I. Zhmoidin, ibid., (1), p. 70 (1970).

45. J. Mukerji, Mem. Sci. Rev. Met., 60, p. 785 (1963); J. Amer. Ceram. Soc., 48, p. 210 (1965).

46. P. P. Budnikov and S. G. Tresvyatskii, Dokl. A N SSSR, 89, p. 479 (1953).

47. D. A. R. Kay and R. J. Pomfret, J.I.S.I., 209, p. 362 (1971).

48. Y. P. Nikitin et al., Dokl. A N SSSR, 148, p. 160 (1963).

49. V. I. Nizhenko et al., Poroshkovaya Met., A N U SSSR, 5, (6), p. 36 (1965).

50. V. I. Nizhenko et al., Poverkh Yavleniya Rasphavakh Vaznikayushchikh nikh Tverd. Fazakh, Nalchik 1965, p. 211.

51. V. K. Kulifeev et al., Izv. V U Z, Tsvet. Met., 12 (1), p. 80 (1969).

52. S. B. Yakabashvili, Avt. Svarka, 23 (6), p. 22 (1970).

53. S. M. Pupynina et al., Sb. Tr. Tsent. Nauch-Issled. Inst., Chern. Met., No. 70, p. 47 (1969).

54. P. P. Evseev, Automatic Welding, 20 (11), p. 42 (1967).

55. R. J. Hawkins et al., J.I.S.I., 209, p. 646 (1971).

56. W. Eitel, Zement, 27 (30), p. 455; (31), p. 469 (1938).

57. B. Porter and E. A. Brown, J. Am. Ceram. Soc., 45 (1), p. 49 (1962).

58. K. K. Kelley, "Contributions to Data on Theoretical Metallurgy:XIII", U.S. Bur. Mines Bull., No. 584 (1960).

59. B. F. Naylor, J. Am. Chem. Soc., 67, p. 150 (1945).

60. T. Baak and A. Olander, Acta Chem. Scand., 9 (8), p. 1350 (1955).

61. W. Gutt and J. Osborne, Trans. Brit. Ceram. Soc., 69, p. 125 (1970).

62. H. Kojima, S. G. Whiteway, and C. R. Masson, Can. J. Chem., 46, p. 2968 (1968).

63. Ya. I. Ol'shanskii, Dokl. A N SSSR, 114, p. 1246 (1957).

64. L. Hillert, Acta Chem. Scand., 18, p. 2411 (1964).

65. H. Kojima and C. R. Masson, Can. J . Chem., 47, p. 4221 (1969).

66. W. Oelsen and H. Maetz, Mitt. Kaiser-Wilhelm-Inst. Eisenforsch, 23, p. 195 (1941).

67. M. W. Davies and R. J. Hawkins, J.I.S.I., 209, p. 226 (1971).

68. P. Pascal, Z. Electrochem., 19 (16), p. 610 (1913).

69. C. K. Kuo and T. S. Yen, Acta Chimica Sinica, 30 (4), p. 381 (1964).

70. A. Mitchell and B. Burel, J.I.S.I., 208 (4), p. 407 (1970).

71. Z. P. Ershova and Ya. I. Ol'shanskii, Geokhimiya, 1, p. 214 (1957).

72. L. Hillert, Acta Chem. Scand., 20, p. 290 (1966).

73. T. Baak, "Physical Chemistry of Steelmaking", p. 84, John Wiley and Sons, London, 1958.

74. F. D. Richardson et al., "Physical Chemistry of Process Metallurgy", Part 2, Met. Soc. Conf., 8 (AIME).

75. A. Mitchell and G. Beynon, Met. Trans., 2 (12), p. 3333 (1971).

76. A. Mitchell, Trans. Met. Soc. AIME, 242, p. 2507 (1968).

77. R. Sridhar and J. H. E. Jeffes, Trans. Inst. Mining Met., 77, p. C53 (1968).

78. H. Flood, T. Forland and K. Grjotheim, "The Physical Chemistry of Melts", Inst. Min. Met., p. 46 (1953).

79. W. Holzgruber and E. Plockinger, Stahl Eisen, 88, p. 638 (1968).

80. M. M. Klynev, and B. B. Topilin, Izv. VUZ Chern. Met., (1), p. 78 (1962).

81. Yu. A. Shulte et al., Stal in English, (1), p. 37, (1960).

82. Yu. V. Latash et al., Automatic Welding, 13 (9), p. 197 (1960).

83. G. K. Bhat, First Int. Symposium on ESR and Casting Tech., Pittsburg (1967).

84. P. P. Evseyev and A. F. Filippov, Izv. A N SSSR Metally, (3), p. 41 (1968).

85. A. Sanderlands, post-graduate thesis, University of Sheffield (1966).

86. D. A. R. Kay, 1st Int. Sym. on ESR and Casting Tech., Pittsburg (1967).

87. C. K. Cooper and D. A. R. Kay, J.I.S.I., 208, p. 856 (1970).

88. V.I. Kasin, Freiberger Forschungsh, Reihe B, 126, p. 97 (1967).

89. C. K. Cooper, D. Ghosh, D. A. R. Kay and R. J. Pomfret, "ESR Reaction Sites", Proceedings of 28th Electric Furnace Conference, Pittsburg (1970).

90. J. Hlineny and Z. Buzek, Hutniche Listy (8), p. 524 (1966).

91. D. J. Swinden, "Parameters Affecting the Behaviour of Sulphur During ESR", paper presented at Int. Symposium on Met. Chem. Applications

in Ferrous Met., July, 1971.

92. A. Ghosh and T. B. King, Trans. TMS AIME, 245, p. 145 (1969).

93. P. Delahay, "New Instrumental Methods in Electrochemistry", p. 350, Interscience, N.Y., 1965.

94. Standard Methods of Analysis of Iron, Steel and Ferro-Alloys, United Steel Companies Ltd., Sheffield, 1951.

95. N. L. Johnson and F. C. Leone, "Statistics and Experimental Design in Engineering and the Physical Sciences", Volume I, John Wiley and Sons, N.Y., 1964.

96. A. E. J. Forno et al., J.I.S.I., 209, p. 966 (1971).

97. J. F. Elliott and M. Gleiser, "Thermochemistry for Steelmaking", Volume I, 1960, Addison-Wesley.

98. W-K. Lu and A. E. Hamielec, "The Role of Interfacial Tension in Slag/Metal Reactions", paper presented at the Int. Symposium Met. Chem. and Application in Ferrous Met., July, 1971.

99. M. A. Maulvault and J. F. Elliott, Electric Furnace Proceedings, 28, p. 13, Pittsburgh, 1970.

100. Y. Nakagawa and A. Momose, Tetsu-to-Hagane Overseas, 5 (2), p. 105 (1965).

101. A. W. Fischer, Arch. Eisenhuttenw., 31, p. 365 (1960).

APPENDIX I

GRAVIMETRIC DETERMINATION OF SULPHUR IN CaF_2-BASED SLAGS

The standard Leco technique used for slag sulphur analysis was checked by a gravimetric method described in reference (94). Following is a brief description of the method used:

(i) 0.5 g of slag was fused with 6 g of K_2CO_3 and 0.1 g of KNO_3 in a platinum crucible in an electric furnace.

(ii) The fused mass was extracted in 150 ml of distilled water and digested.

(iii) The solution obtained was filtered on a pulp pad and washed with a hot solution of K_2CO_3 (1%).

(iv) HCl (sp. gr. 1.16) was carefully added to this solution until it was neutral, when an additional 25 ml of excess acid (HCl) was added.

(v) This solution was slowly evaporated to dryness. 25 ml of HCl (Sp. gr. 1.16) was further added to the residue and the solution was again evaporated to dryness.

(vi) Residue was dissolved in 100 ml of HCl (2:98). The solution was filtered and washed before 5 ml of 20% BaCl solution was added.

(vii) It was boiled for 10 - 15 minutes and allowed to stand for 4 hours before filtration. The residue was washed, ignited and weighed as $BaSO_4$ from which the sulphur content of the slag was calculated.

APPENDIX IIA

STATISTICAL TREATMENT OF SULPHUR CONCENTRATION-TIME DATA

Making the assumptions listed by Johnson and Leone(95) (p. 382), a set of n data points (x_i, y_i) can be fitted by regression to the line:

$$y = A + Bx$$

using the method of least squares, where y is a dependent variable and x is an independent (or controlled) variable. In this investigation, the sulphur concentration is taken as the variable y, while time is the independent variable x. Least square analysis(95) gives the value of the slope B and the intercept A as:

$$B = \frac{\Sigma\, x_i y_i - n.\bar{x}.\bar{y}}{\Sigma\, x_i^2 - n(\bar{x})^2}$$

and

$$A = \bar{y} - B\bar{x}$$

where $\bar{x} = (\Sigma\, x_i)/n$ and $\bar{y} = (\Sigma\, y_i)/n$.

The standard deviation, s, about this fitted line is given(95) by:

$$s = \sqrt{\sum_{i=1}^{n} (y_i - A - Bx_i)^2/(n-2)}$$

a preferable form of which is:

$$s = \sqrt{\frac{\Sigma y_i^{\,2} - A\Sigma\, y_i - B\Sigma\, x_i y_i}{n-2}}$$

The statistic s^2 is an estimator of the variance about the regression line.

A 100(1-γ) percent confidence interval about the regression line for any given value of x (say x_o) can be shown(95) to be:

$$\text{C.I.} = \underline{+}\, s \cdot t_{n-2,1-\gamma/2}\, [1/n + \frac{(x_o-\bar{x})^2}{\Sigma\,(x_i - \bar{x})^2}\,]^{1/2}$$

where $t_{n-2,1-\gamma/2}$ is the "students" t-distribution with n-2 degress of freedom.

The correlation coefficient is a measure of the linear relationship between the two variables x and y. When it is equal to ± 1, there is a perfect correlation, i.e., x and y can be related absolutely by a linear mathematical equation. The maximum likelihood estimator of the correlation coefficient is given by:

$$r = \frac{\Sigma(x_i-\bar{x})(y_i-\bar{y})}{\{[\Sigma(x_i-\bar{x})^2][\Sigma(y_i-\bar{y})^2]\}^{1/2}}$$

which can be simplified as:

$$r = \frac{n\Sigma x_i y_i - (\Sigma x_i)(\Sigma y_i)}{\{[n\Sigma x_i^2 - (\Sigma x_i)^2][n\Sigma y_i^2 - (\Sigma y_i)^2]\}^{1/2}}$$

A test of significance can be obtained for the correlation coefficient by comparison with critical values of the correlation coefficient given in Table 12.10 (reference 95). This table gives critical values of r for different sample sizes and different values of γ. If the value of the correlation coefficient obtained is equal to or greater than the critical value given in this table, then the regression line can be considered to be significant at the $100(1-\gamma)$ confidence level.

APPENDIX IIB

STANDARD ERROR AND CONFIDENCE INTERVAL CALCULATIONS OF THE RATES

As rate expressions involve mathematical operations with different regression data, the standard error of each rate has to be independently derived. The following relationships are very useful in the derivation of the standard errors of the rates:

(i) If y is given by a linear combination such as:

$$y = a\, x_1 + b\, x_2 \qquad (1)$$

then the variance of y is given by:

$$\sigma_y^2 = a^2 \sigma_{x_1}^2 + b^2 \sigma_{x_2}^2 \qquad (2)$$

where $\sigma_{x_1}^2$, $\sigma_{x_2}^2$ are the variances of x_1 and x_2 respectively, and a,b are constants.

(ii) If the variance about the regression line $y = A + Bx$ is given by σ^2, the variance of the slope B is given by:

$$\sigma_B^2 = \frac{\sigma^2}{\Sigma(x_i-\bar{x})^2} \qquad (3)$$

and the variance of A is:

$$\sigma_A^2 = [\frac{1}{n} + \frac{\bar{x}^2}{\Sigma(x_i-\bar{x})^2}]\,\sigma^2 \tag{4}$$

ERATE is given by equation (3.25) as

$$\text{ERATE} = \frac{\dot{m}}{100}\,(\,[S]_E - [S]_D) \tag{5}$$

where $[S]_E$ is the average sulphur content of the electrode with variance s_E^2. $[S]_D = A + Bt$ with the variance about the line given by s_D^2. Hence:

$$\text{ERATE} = y = \frac{\dot{m}}{100}\,([S]_E - \{A+Bt\}) \tag{6}$$

also

$$\bar{y} = \frac{\dot{m}}{100}\,([S]_E - \{A+B\bar{t}\}) \tag{7}$$

Therefore:

$$y = \bar{y} - \frac{\dot{m}}{100}\,(t-\bar{t})B \tag{8}$$

Hence, from equation (2):

$$s_y^2 = s_{\bar{y}}^2 + (\frac{\dot{m}}{100})^2\,(t-\bar{t})^2\,s_B^2 \tag{9}$$

Now, $s_{\bar{y}}^2$ and s_B^2 must be obtained before the standard error of ERATE, s_y, can be calculated. From equation (3), s_B^2 is simply given by:

$$s_B^2 = \frac{s_D^2}{\Sigma(t-\bar{t})^2} \tag{10}$$

Now,

$$\bar{y} = \frac{\dot{m}}{100}([S]_E - \overline{[S]}_D) \qquad (11)$$

Therefore:

$$s^2_{\bar{y}} = \left(\frac{\dot{m}}{100}\right)^2 [s^2_E + s^2_{\overline{[S]}_D}] \qquad (12)$$

and since:

$$s^2_{\overline{[S]}_D} = s^2_D / n_D$$

the square of standard error of ERATE is given by:

$$s^2_{ER} = s^2_y = \left(\frac{\dot{m}}{100}\right) [s^2_E + s^2_D \{\frac{1}{n_D} + \frac{(t-\bar{t})^2}{\Sigma(t-\bar{t})^2_D}\}] \qquad (13)$$

Similarly the square of the standard errors of PRATE and ARATE can be derived and are given by:

$$\begin{aligned} s^2_{PR} = 10^{-4} \{\dot{m}^2 [s^2_D (\frac{1}{n_D} &+ \frac{(t-\bar{t})^2}{\Sigma(t-\bar{t})_D}) + s^2_I (\frac{1}{n_I} + \frac{(t-\bar{t})^2}{\Sigma(t-\bar{t})^2_I})] \\ &+ VOLINC^2 . s^2_P (\frac{1}{n_P} + \frac{(t-\bar{t})^2}{\Sigma(t-\bar{t})^2_P}) \qquad (14) \\ &+ VOL^2 . \frac{s^2_P}{\Sigma(t-\bar{t})^2_P} \} \end{aligned}$$

$$s_{AR}^2 = 10^{-4} \left[s_{PR}^2 + s_{ER}^2 + \frac{WSLAG^2 \, s_{SI}^2}{\Sigma(t-\bar{t})_{SI}^2} + SKINRT^2 \, . \, s_{SI}^2 \left(\frac{1}{n_{SI}} + \frac{(t-\bar{t})^2}{\Sigma(t-\bar{t})_{SI}^2} \right) \right] \quad (15)$$

The $100(1-\gamma)$ confidence intervals can be obtained from the standard errors of the rates by multiplying by $t_{n-2,1-\gamma/2}$. Th unknown value of the number of degrees of freedom, n, does not allow the accurate determination of the confidence intervals for the three rates. However, Table F in reference (95) indicates that the t-distribtion varies very little with n. In fact, for a 95% confidence level, "t" varies from 2.571 to 1.960 for n = 5 to ∞ . It was decided, therefore, to use 2 as an approximate value of $t_{n-2,0.975}$ for the 90 to 95% confidence interval calculations.

APPENDIX III

CALCULATIONS OF HENRIAN ACTIVITY COEFFICIENTS FOR OXYGEN AND SULPHUR IN AISI C1117 STEEL

The nominal composition of AISI C1117 grade steel is: 0.14 - 0.20% C, 1.00 - 1.30% Mn, 0.04% max. P, 0.08 - 0.13% S. Hence, an average composition for the metal pool:

0.17% C
1.2% Mn
0.04% S
0.04% P
0.011% O

may be assumed. The Henrian activity coefficient, f_x, for any element x can be obtained from:

$$\log f_x = (\%x)\, e_x^x + (\%y)\, e_x^y + (\%z)\, e_x^z + \ldots \qquad (1)$$

where the interaction coefficients e_x^x, e_x^y, . . . are given in the literature. Using the interaction coefficients given in reference (97), f_0 and f_S can be calculated as follows:

$$\log f_0 = (\%0)\ e_0^0 + (\%S)\ e_0^S + (\%P)\ e_0^P + (\%Mn)\ e_0^{Mn} + (\%C)\ e_0^C$$

$$= 0.011\ (-0.20) + 0.04\ (-0.091) + 0.04\ (+0.07) + 0 + 0.17\ (-0.13)$$

$$= -\ 0.02514 = \bar{1}.97486$$

Therefore, $f_0 = 0.9437$

Similarly for sulphur:

$$\log f_S = e_S^S\ (\%S) + e_S^C\ (\%C) + e_S^{Mn}\ (\%Mn) + e_S^P\ (\%P) + e_S^0\ (\%0)$$

$$= 0.0095$$

Therefore, $f_S = 1.046$

Thus, within 6% error, both f_0 and f_S may be taken as unity.

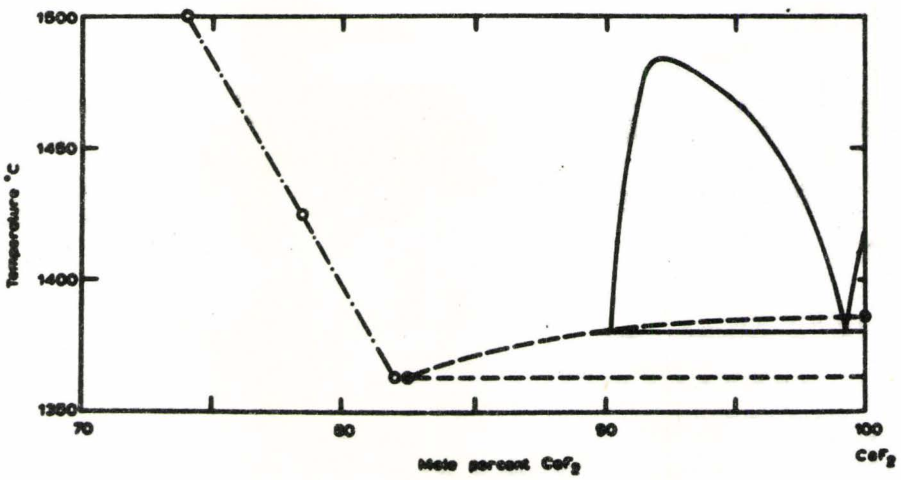

Figure 2.1 CaO-CaF$_2$ phase diagram. Full line, liquidus of Baak[29]; broken line, liquidus and eutectic of Eitel[56]; dash-dot line, liquidus proposed by Kor and Richardson[16].

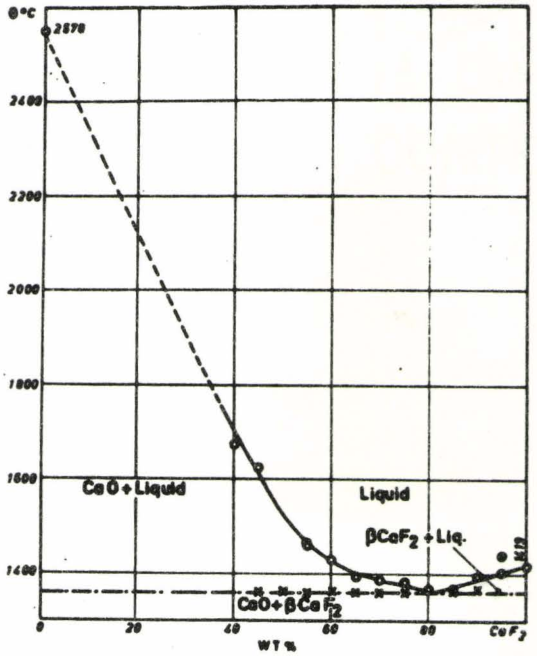

Figure 2.2 CaO-CaF$_2$ phase diagram proposed by Mukerji[45].

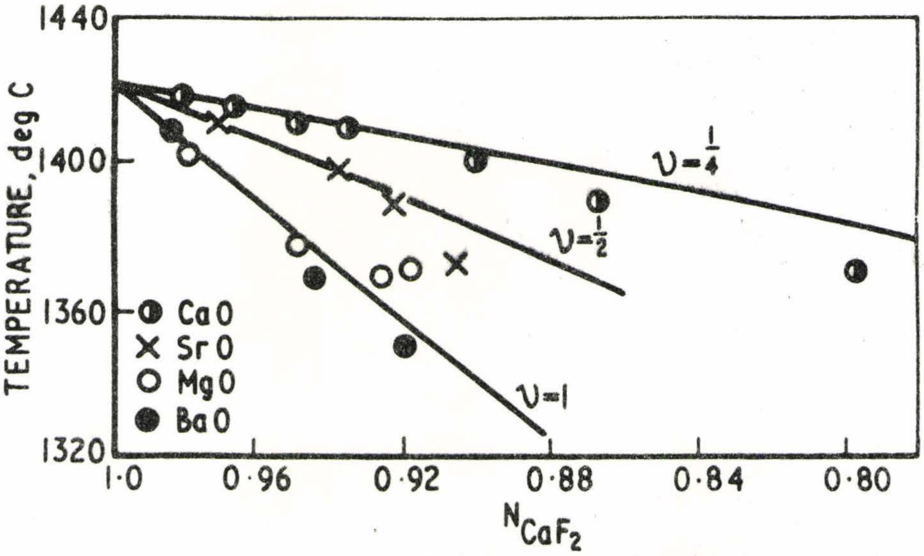

Figure 2.3 Depression of freezing point curves for CaO, SrO, MgO and BaO in CaF_2 (65). Theoretical lines are calculated from the Clausius-Clapeyron equation assuming values for ν (65).

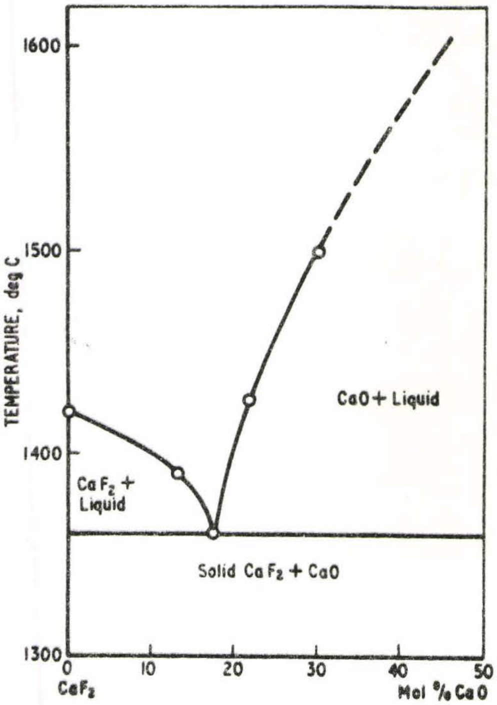

Figure 2.4 CaF_2-CaO phase diagram constructed by by Davies (28).

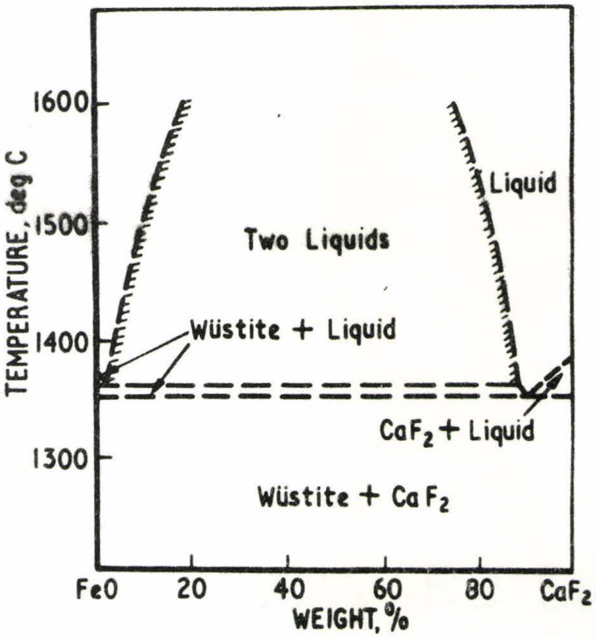

Figure 2.5 FeO-CaF_2 phase diagram$^{(66)}$.

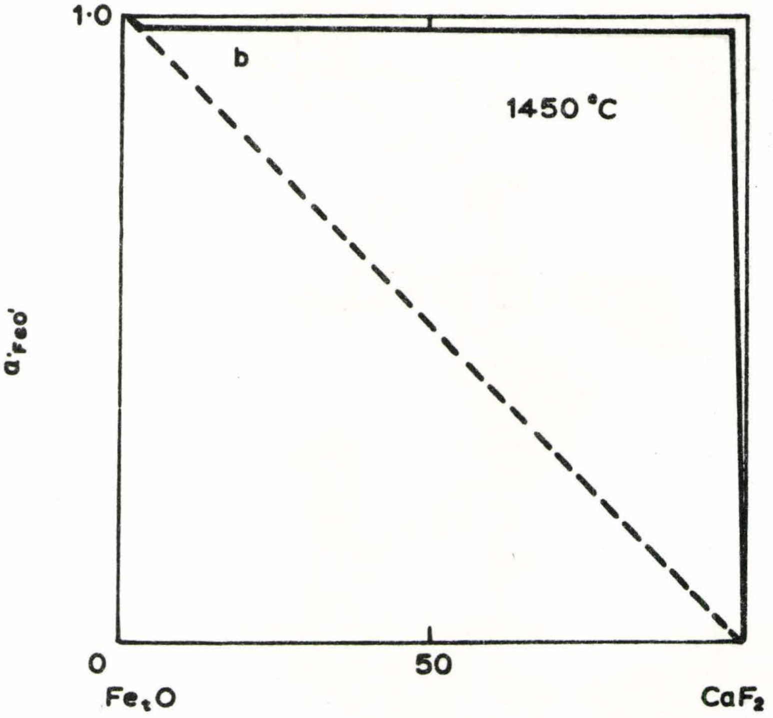

Figure 2.6 a_{FeO} as a function of wt.% Fe_tO at 1450°C$^{(21)}$.

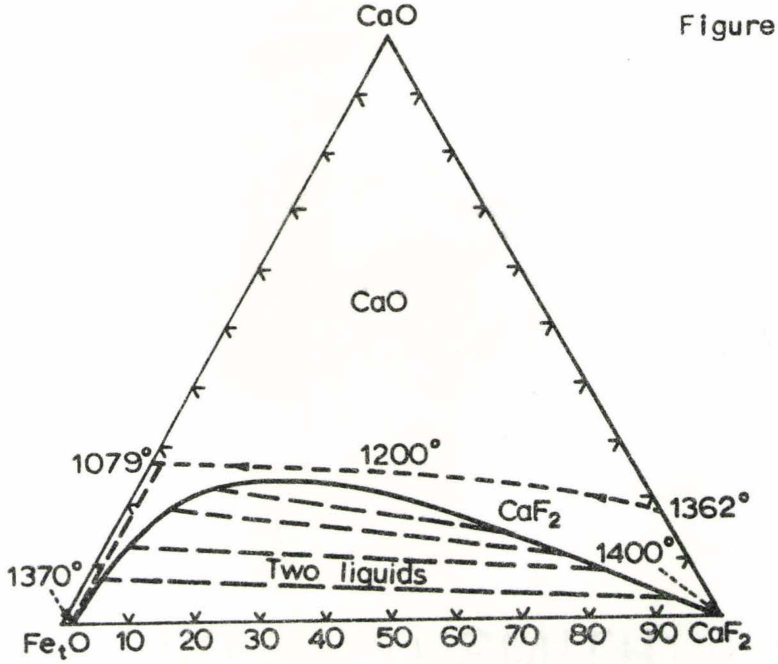

Figure 2.7 CaF$_2$-CaO-FeO phase diagram(66).

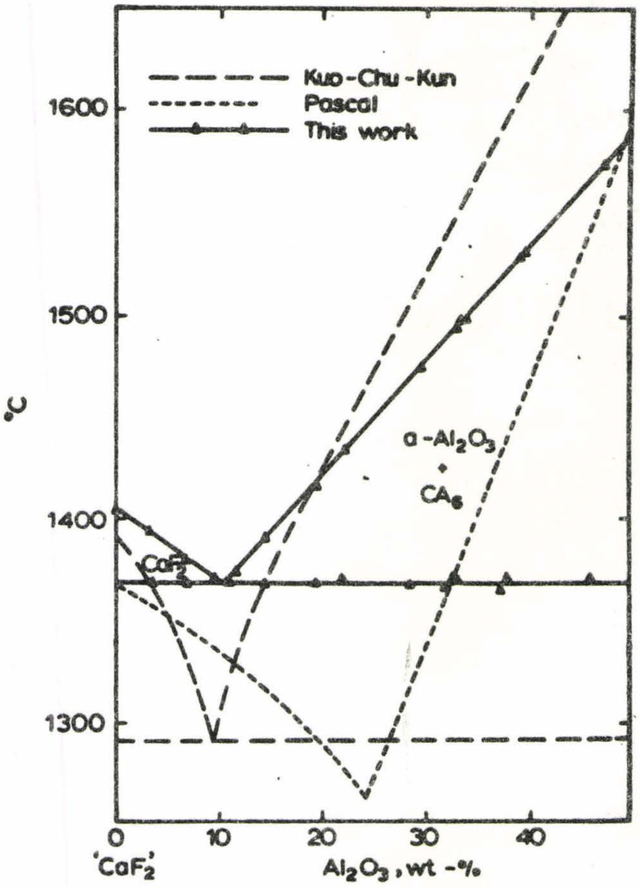

Figure 2.8 CaF$_2$-Al$_2$O$_3$ phase diagram.(70)

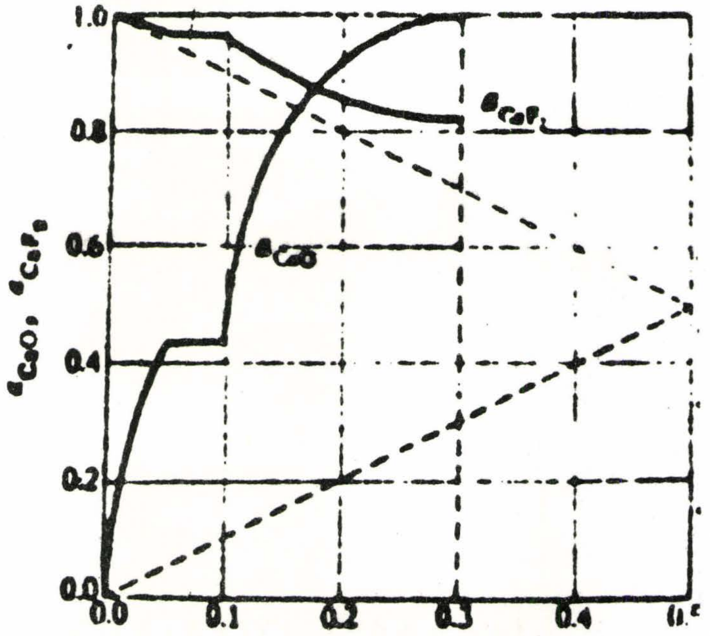

Figure 2.9 Activities of CaO and CaF_2 in the CaF_2-CaO system(15).

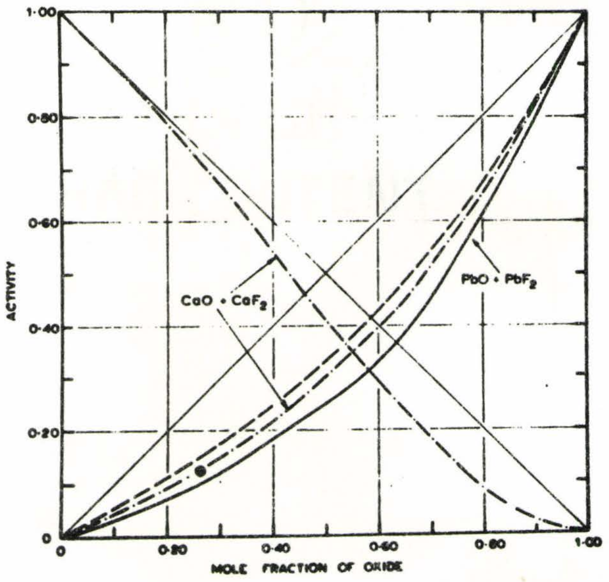

Figure 2.10 Activities of components in CaF_2-CaO system at 1500°C relative to pure liquids, as calculated by Kor and Richardson(16). Broken line, ideal Temkin value for CaO.

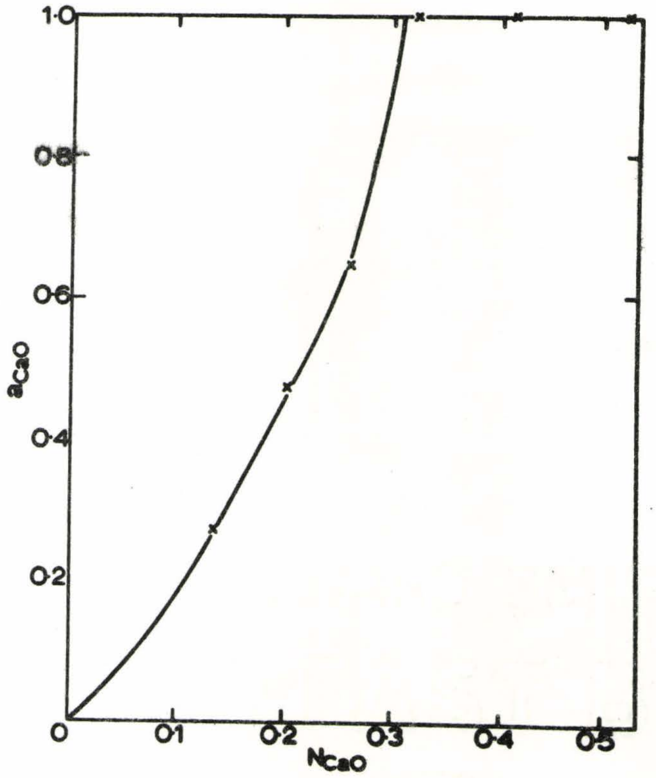

Figure 2.11 Activity of lime in CaF_2-CaO melts at 1500°C (17).

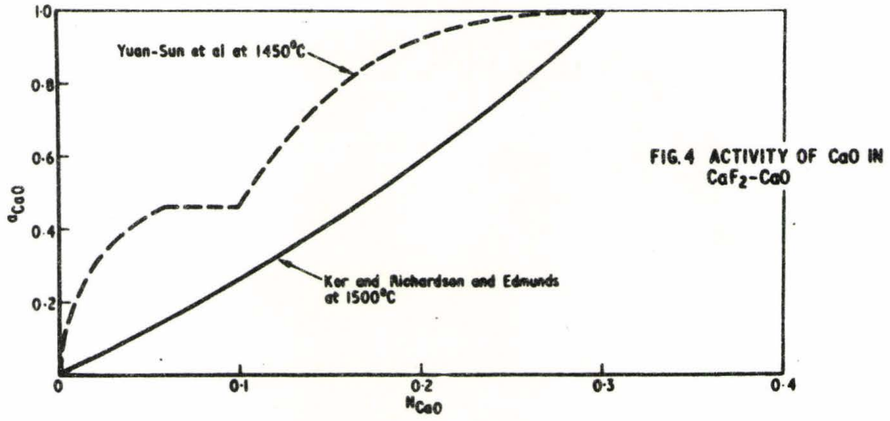

Figure 2.12 Comparison of CaO activities obtained by different authors in the system CaF_2-CaO(28).

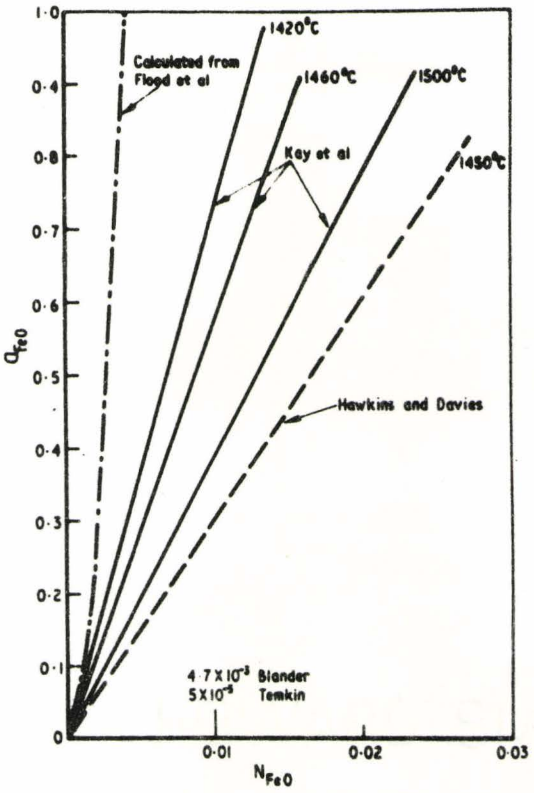

Figure 2.13 Activity of FeO in CaF_2-FeO system.

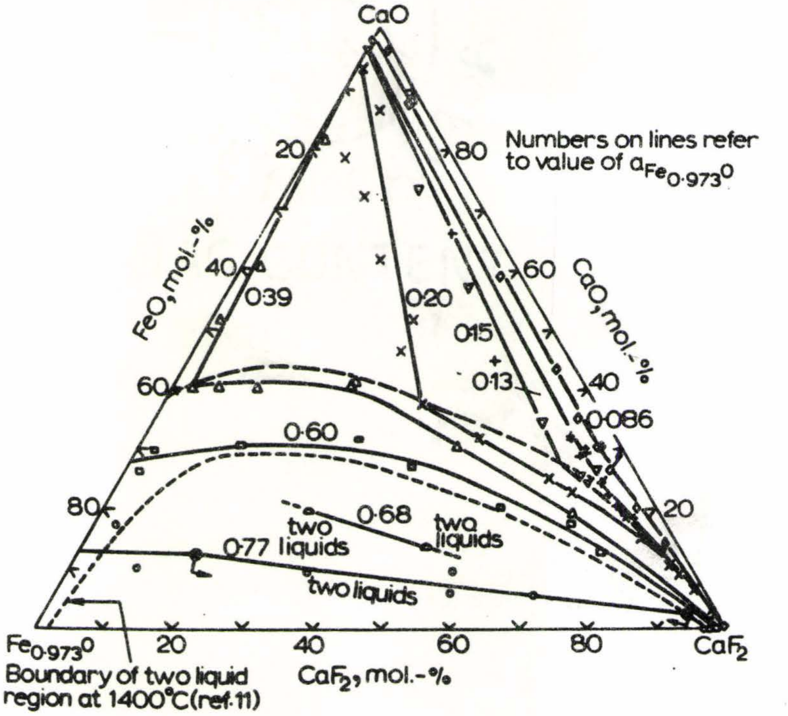

Figure 2.14 "FeO" activities in CaF_2-CaO-"FeO" system$^{(67)}$.

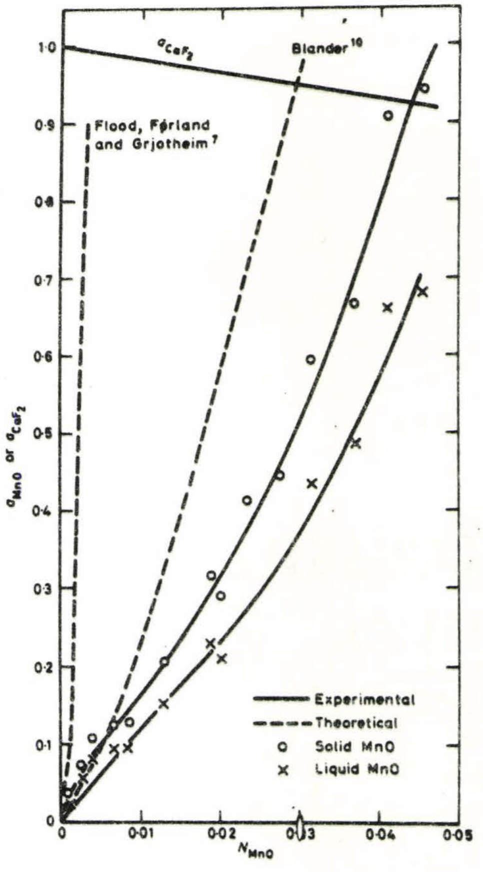

Figure 2.15 MnO activity in CaF_2-MnO system at 1600°C (37).

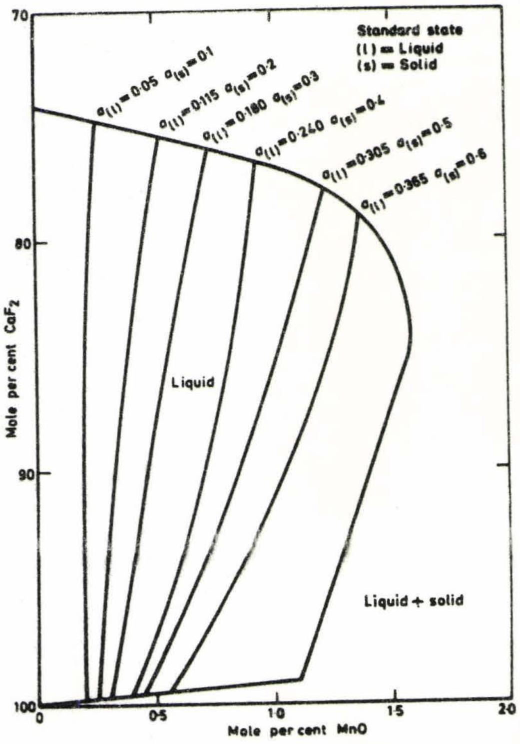

Figure 2.16 Orthogonal plot of the ternary CaF_2-CaO-MnO showing liquidus and a_{MnO} values.

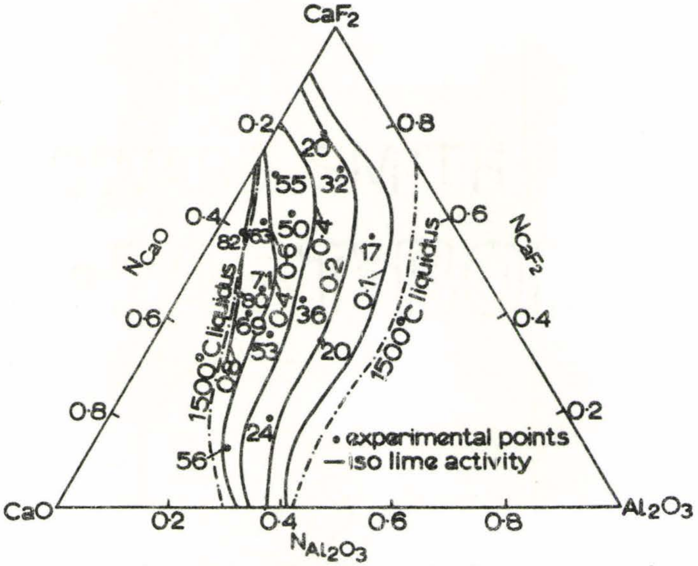

for the sake of clarity the experimental point values have been expressed as whole numbers instead of decimals (e.g. 20=0·20)

Figure 2.17 Activity of lime in CaO-Al_2O_3-CaF_2 system at 1500°C(17).

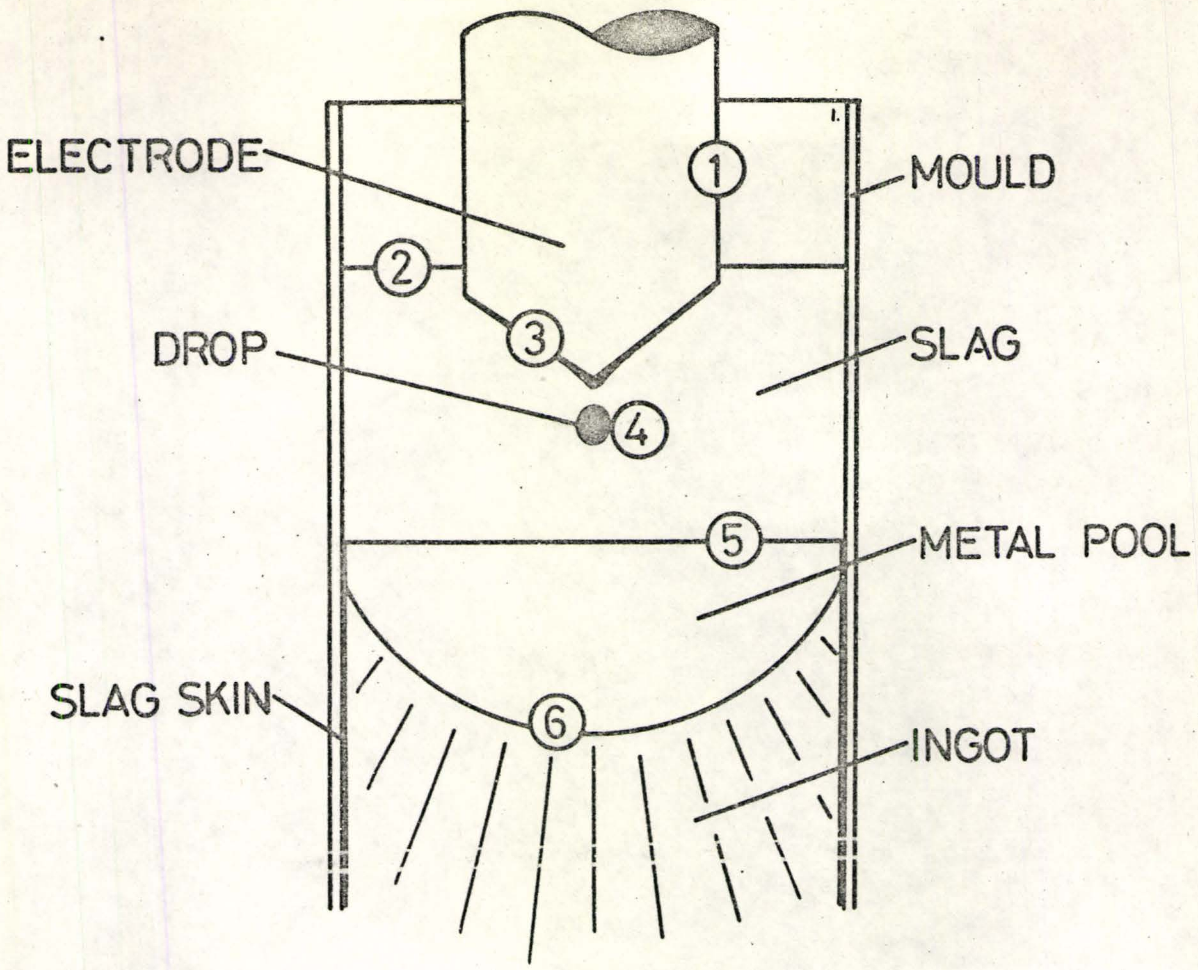

① ELECTRODE/ATMOSPHERE
② SLAG/ATMOSPHERE
③ ELECTRODE TIP/SLAG
④ DROPLET/SLAG
⑤ METAL POOL/SLAG
⑥ METAL POOL/INGOT

Figure 3.1 ESR Reaction Sites.

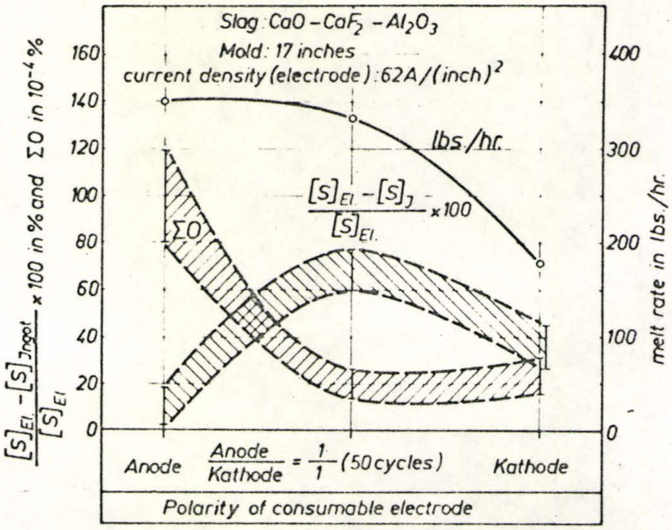

Figure 3.2 Melt rate and behaviour of oxygen and sulphur in AC and DC ESR for a 17" diameter mould(12).

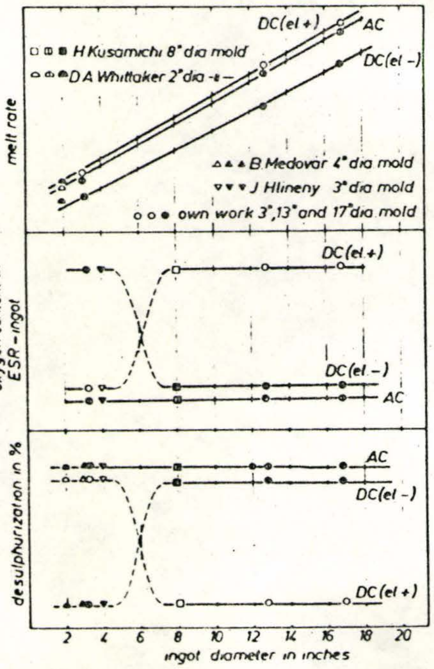

Figure 3.3 Melt rate, oxygen content and desulphurization vs. ingot diameter in AC and DC ESR (schematically)(12).

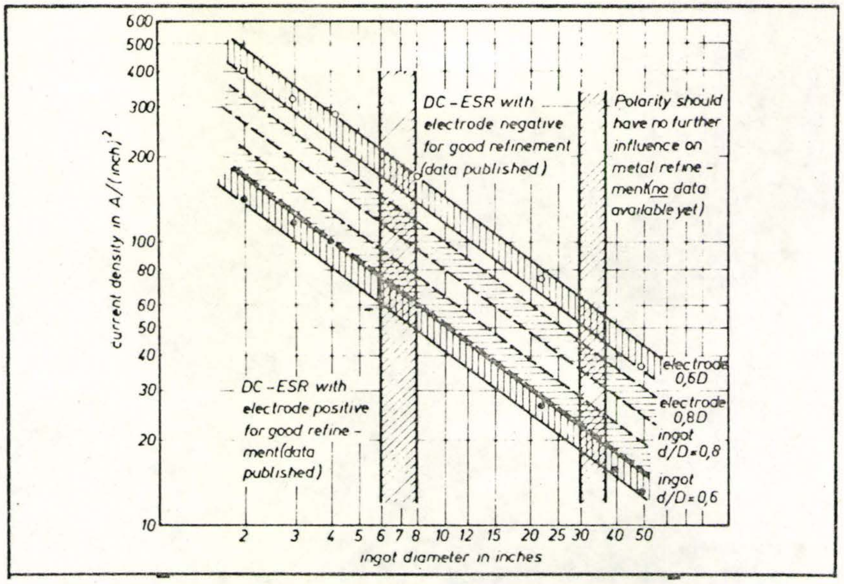

Figure 3.4 Current density at the electrode tip and ingot pool vs. ingot diameter for 0.6 and 0.8 electrode-ingot diameter ratio.

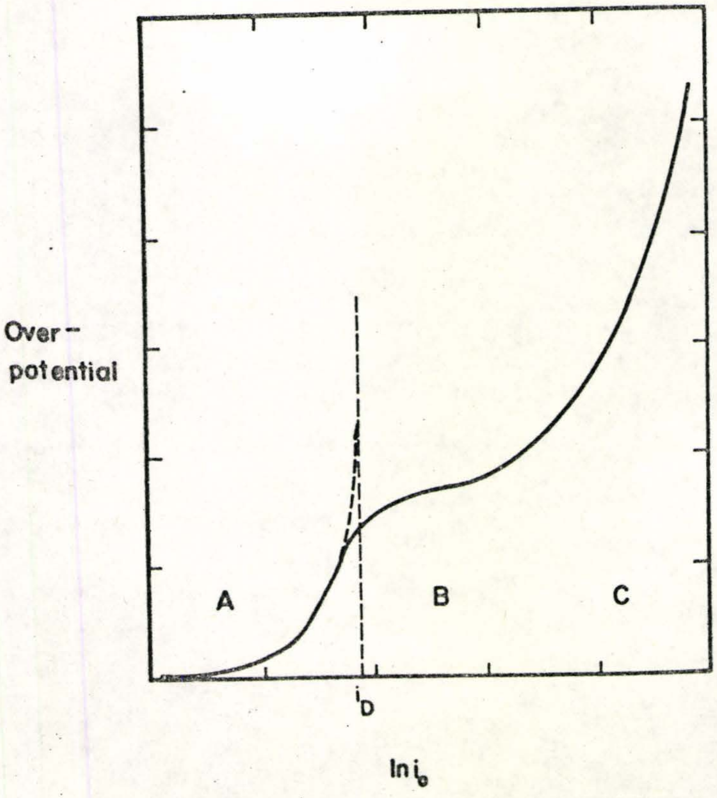

Figure 3.6 Schematic representation of the anodic polarization curves.

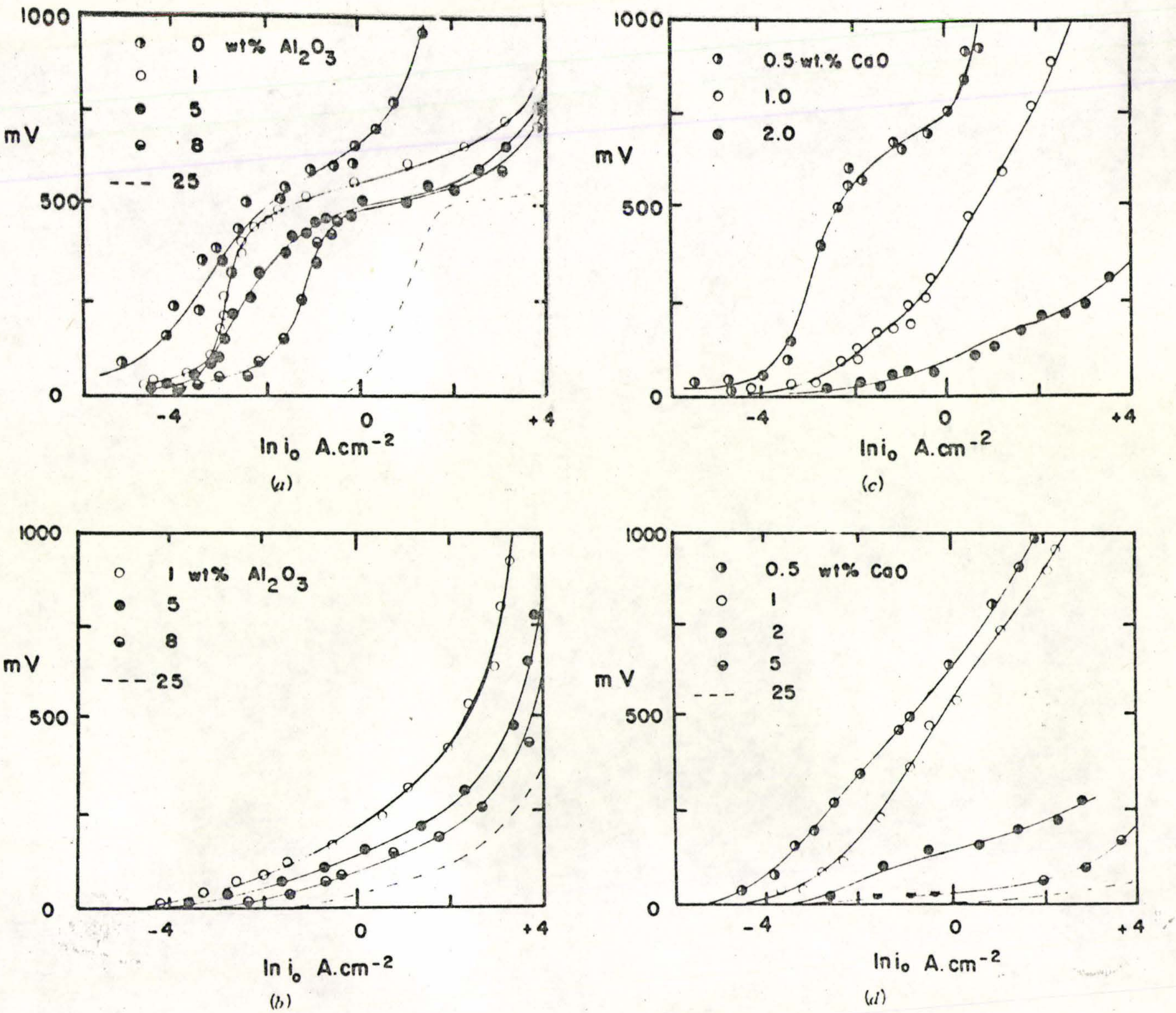

Figure 3.5 (a), (b) Anodic and cathodic polarization curves for CaF_2-Al_2O_3 system; (c), (d) Anodic and cathodic polarization curves for CaF_2-CaO system(75).

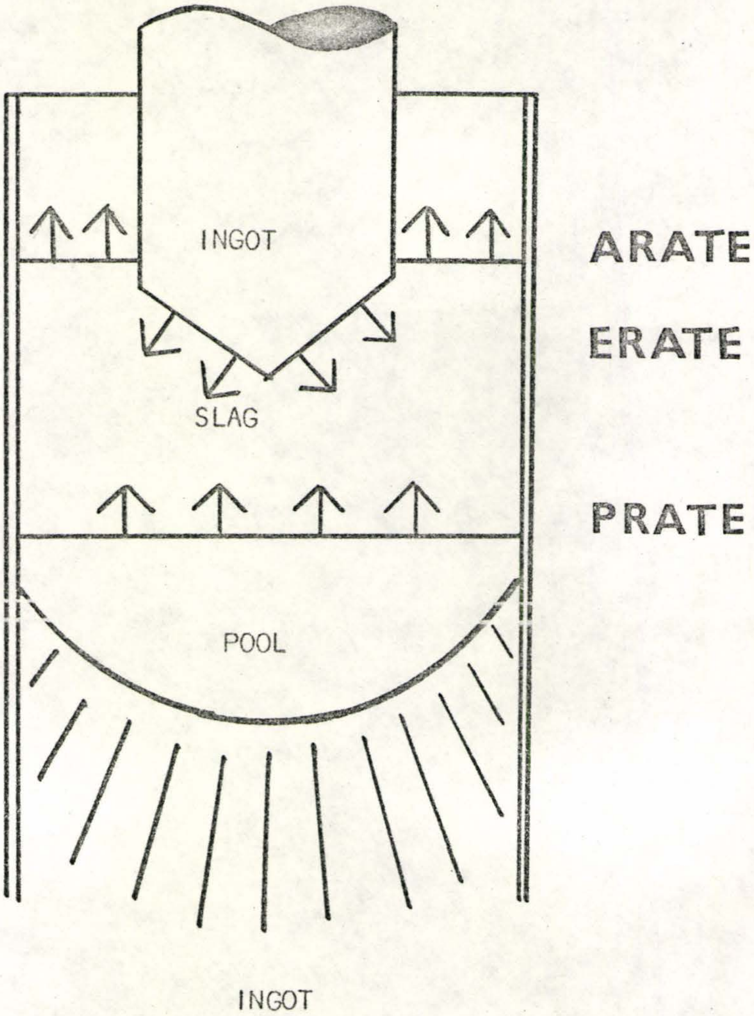

Figure 3.7 Schematic representation of the three rates. The direction of the arrows show the positive direction of each rate.

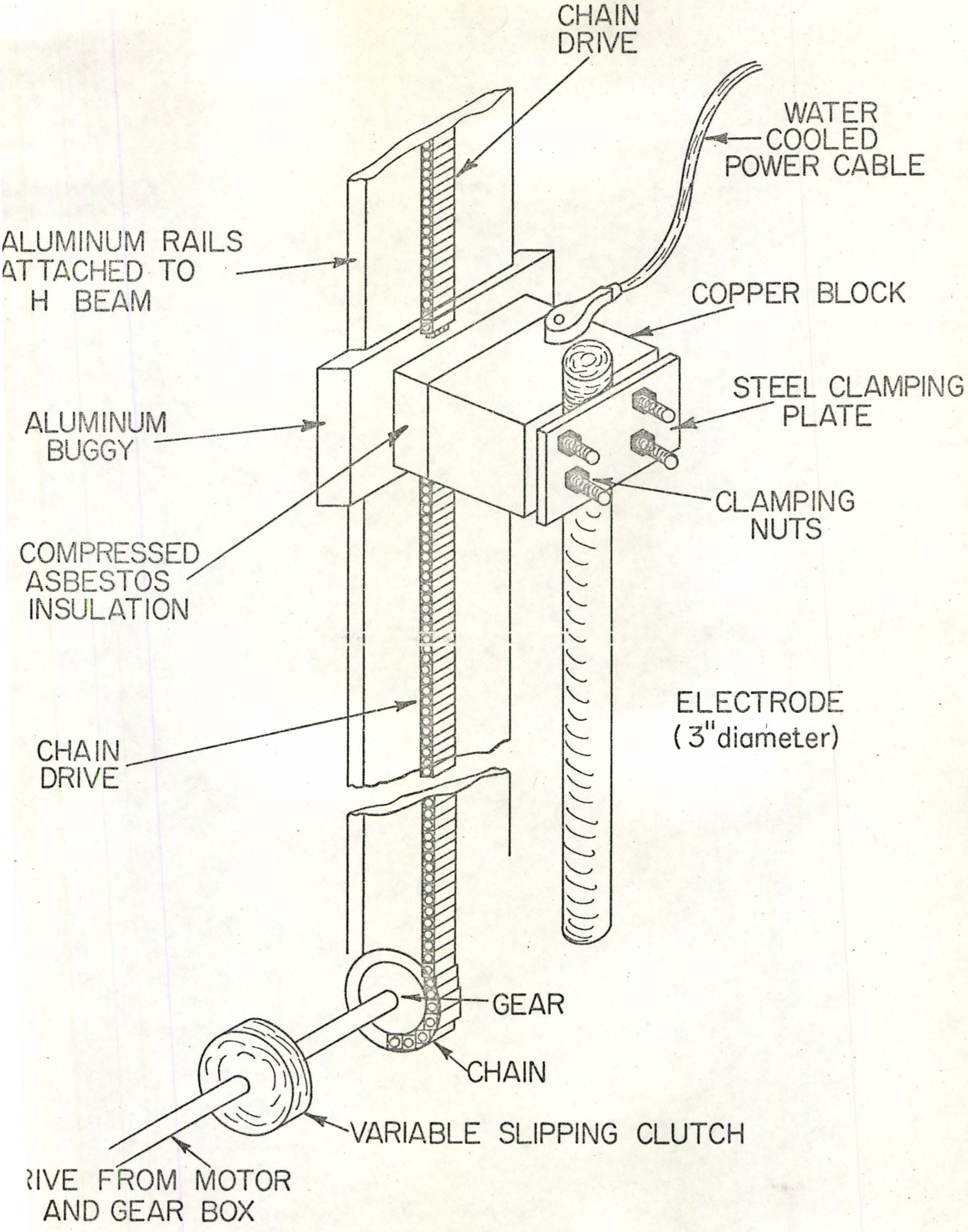

Figure 4.1 Electrode travel and drive mechanism.

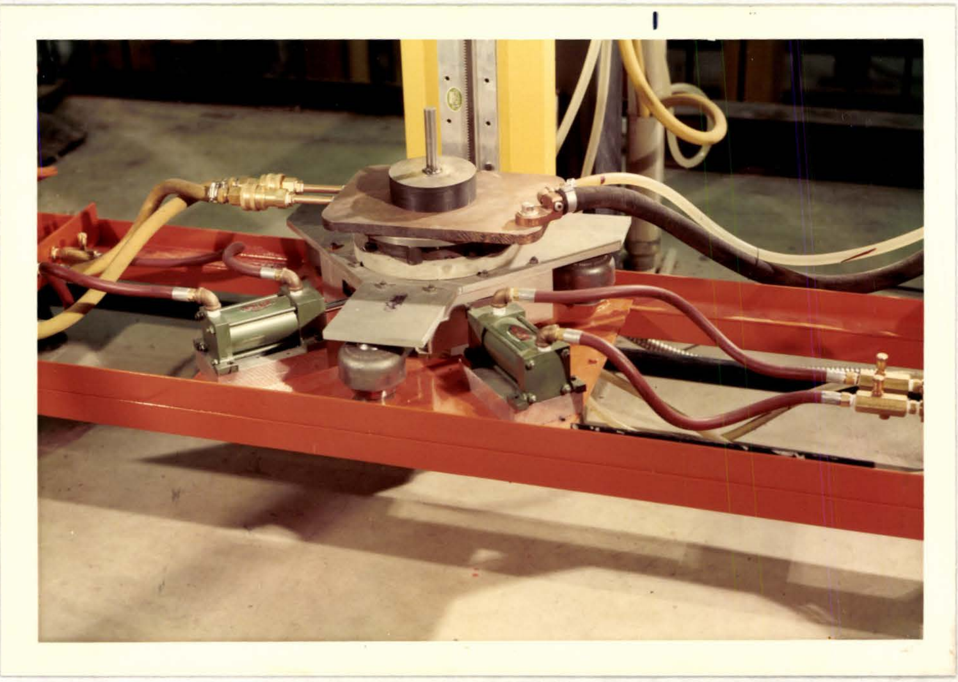

Figure 4.2 Base-plate assembly.

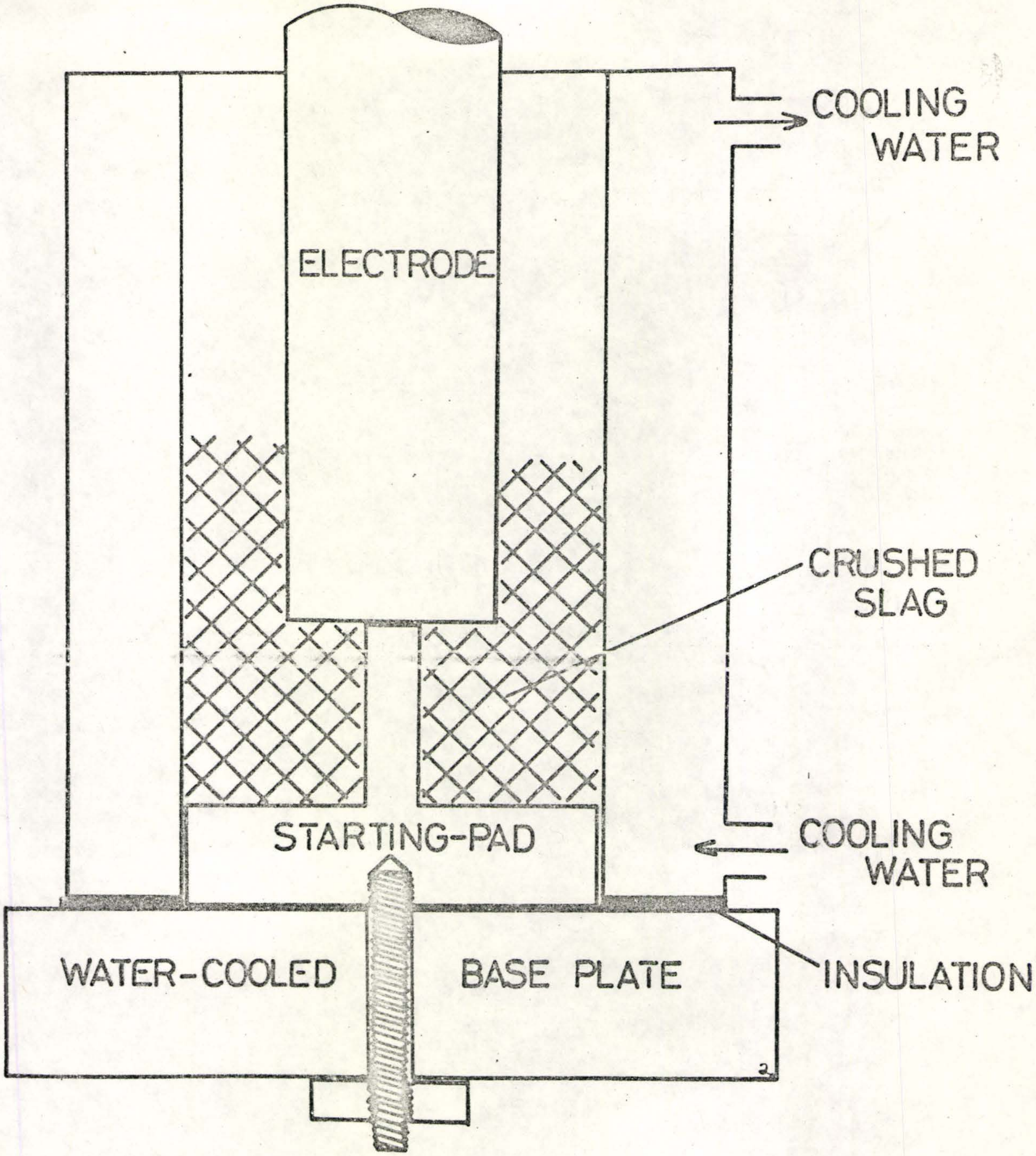

Figure 4.3 Cold start procedure.

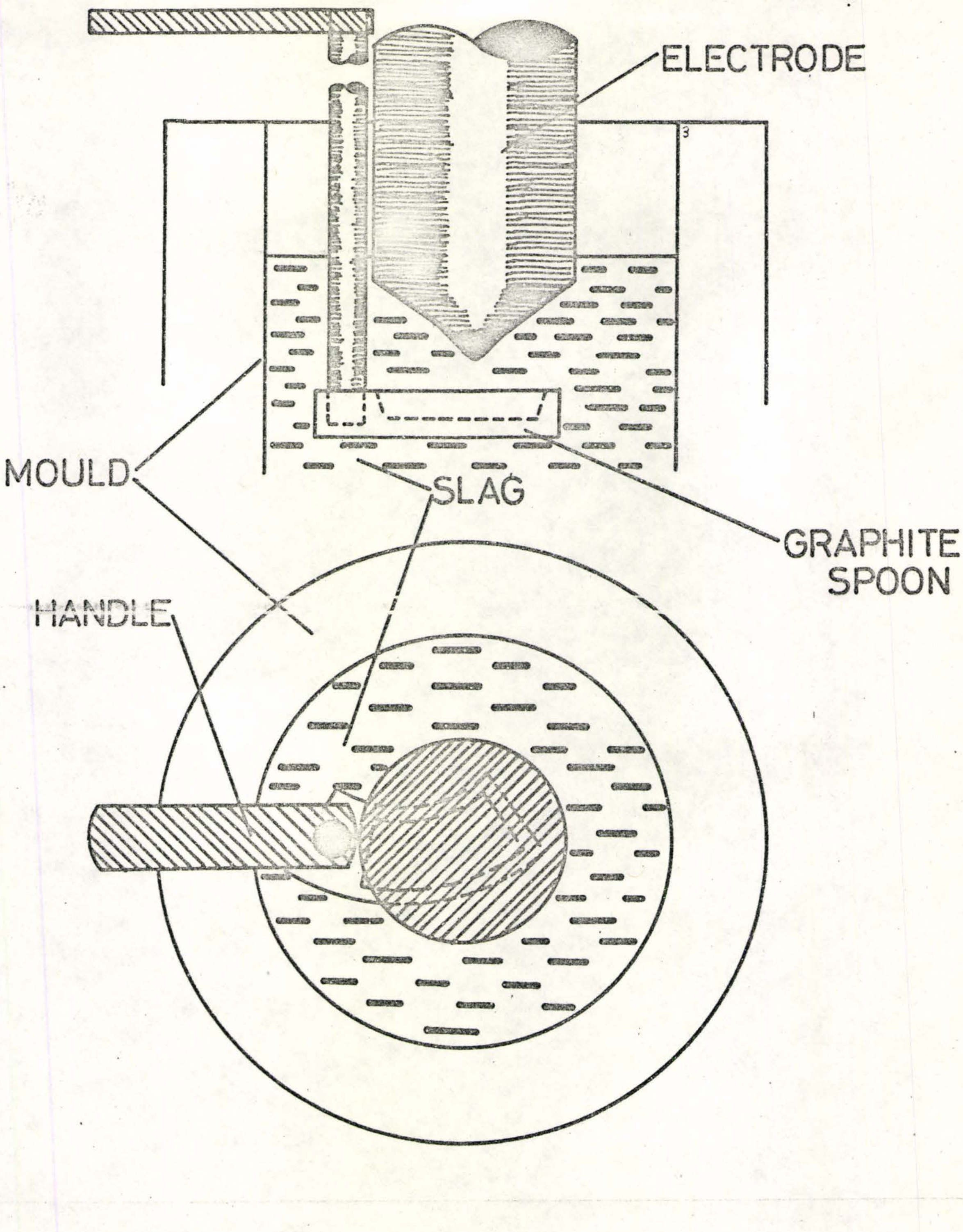

Figure 4.4 Droplet sampling.

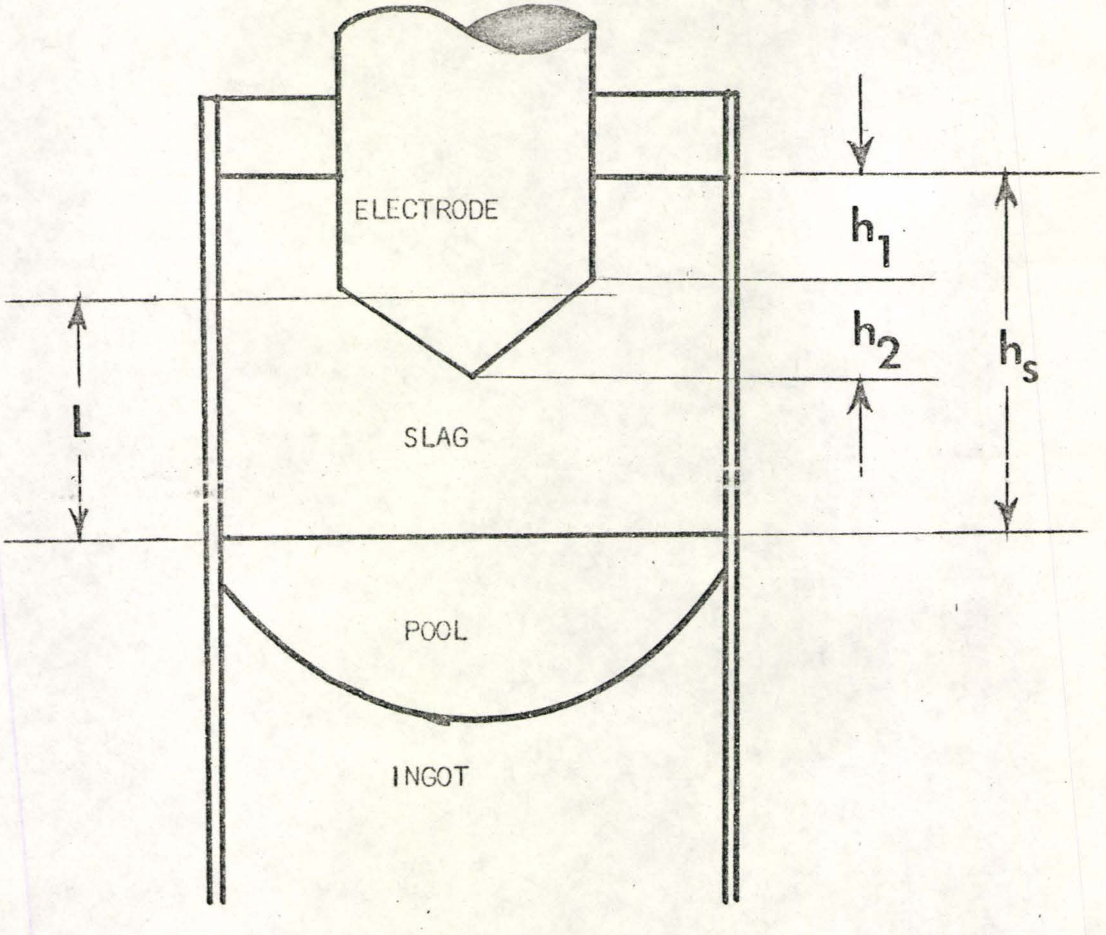

Figure 4.5 Electrode geometry used in slag conductivity calculation.

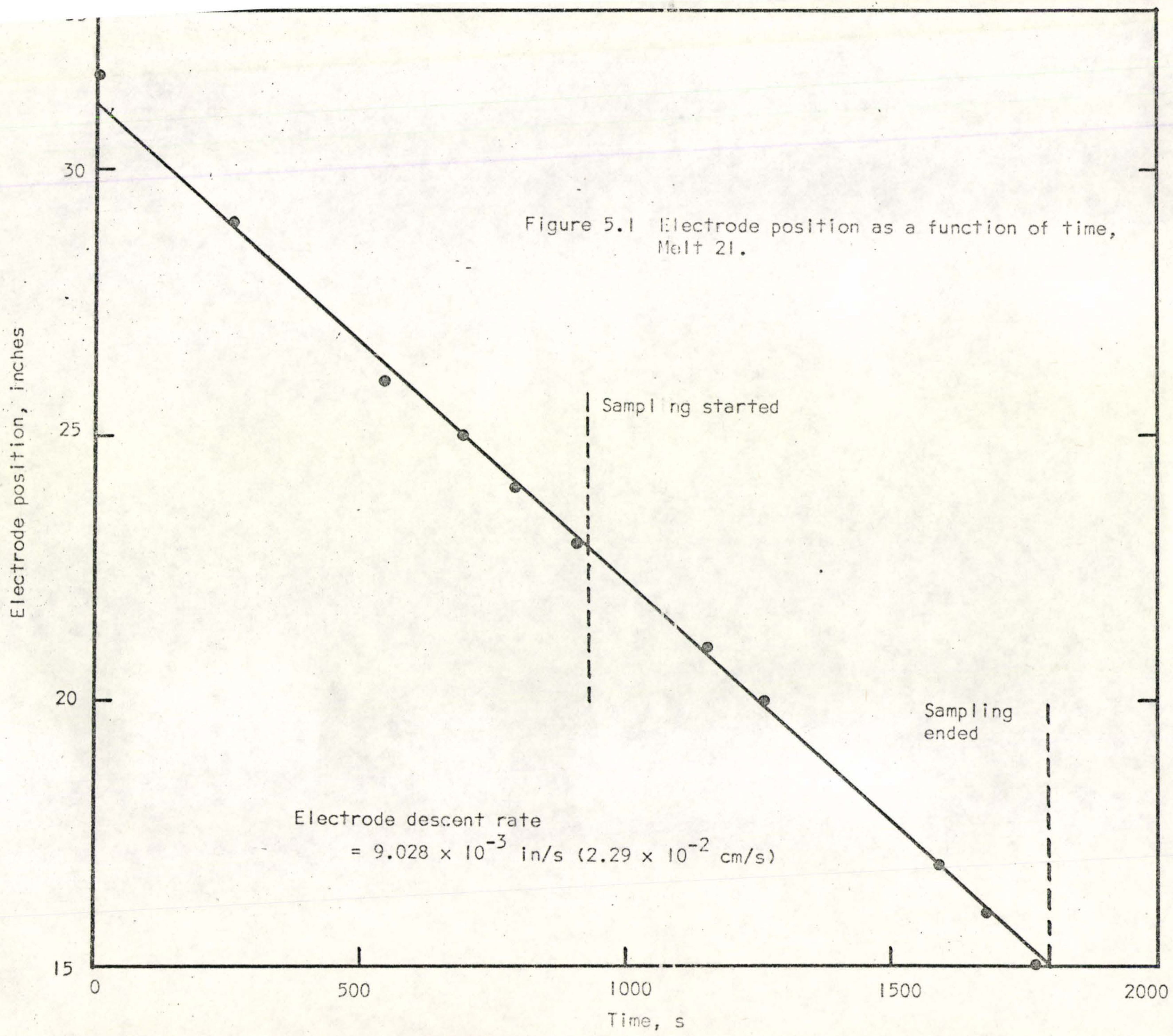

Figure 5.1 Electrode position as a function of time, Melt 21.

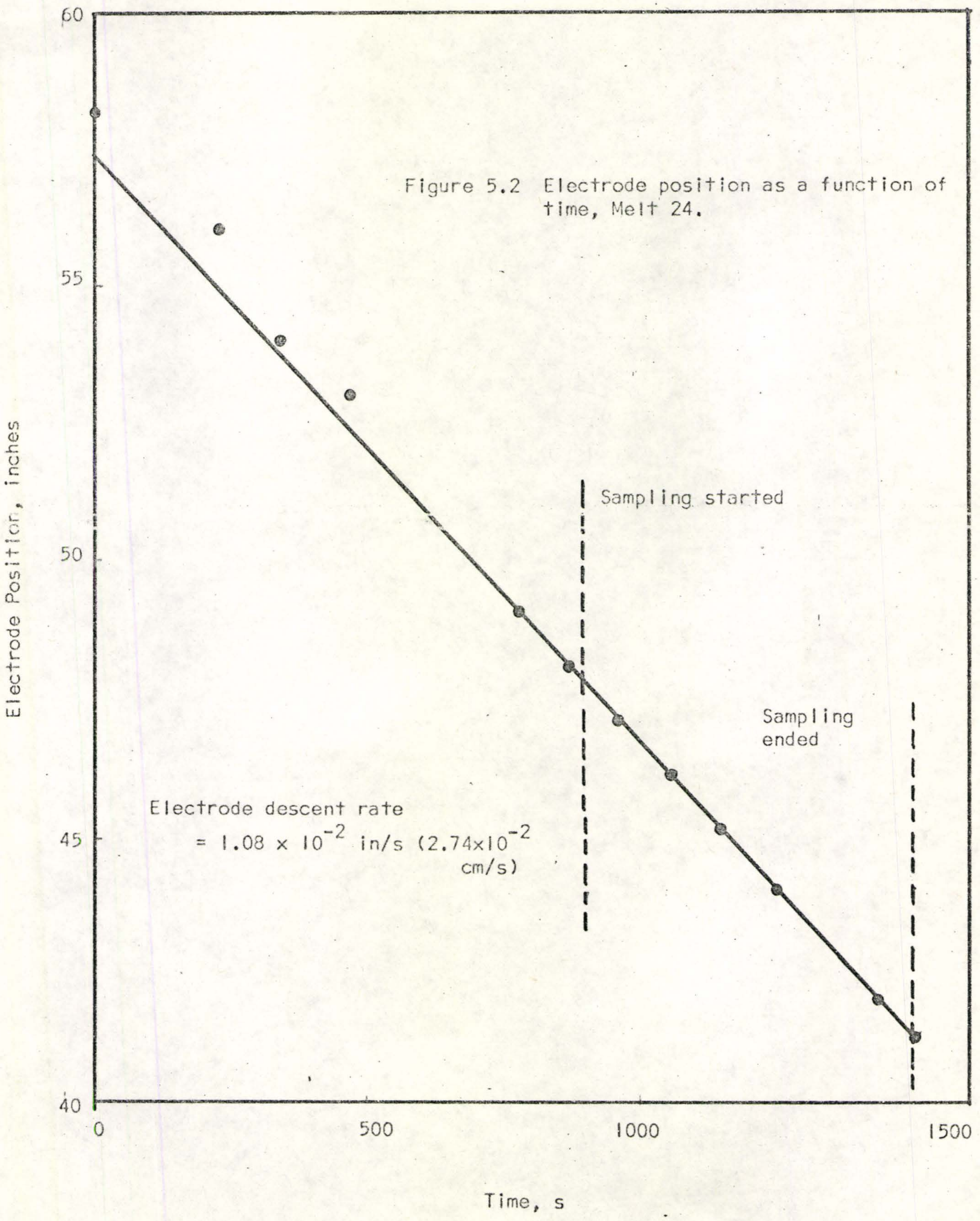

Figure 5.2 Electrode position as a function of time, Melt 24.

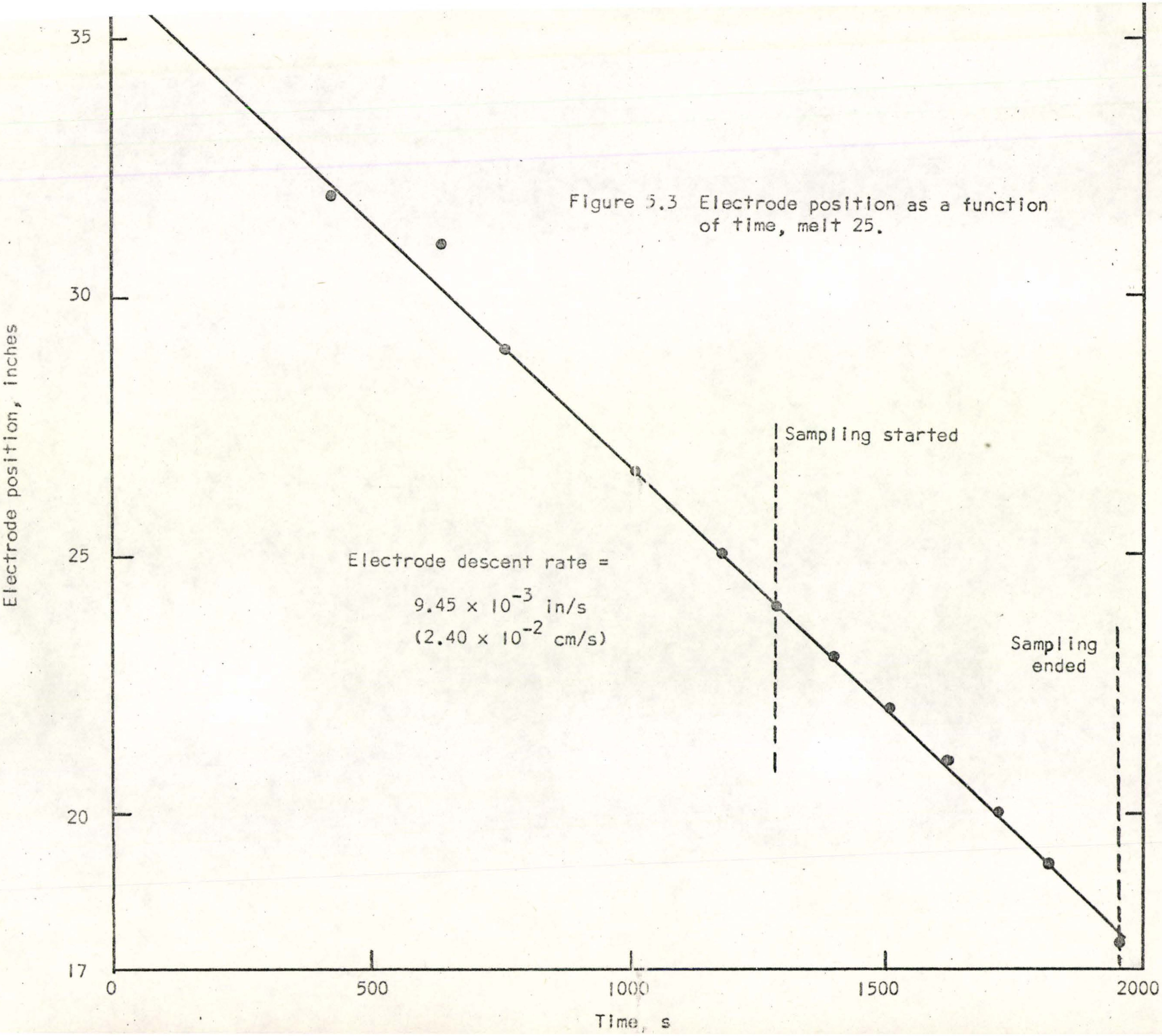

Figure 5.3 Electrode position as a function of time, melt 25.

Electrode descent rate = 9.45×10^{-3} in/s (2.40×10^{-2} cm/s)

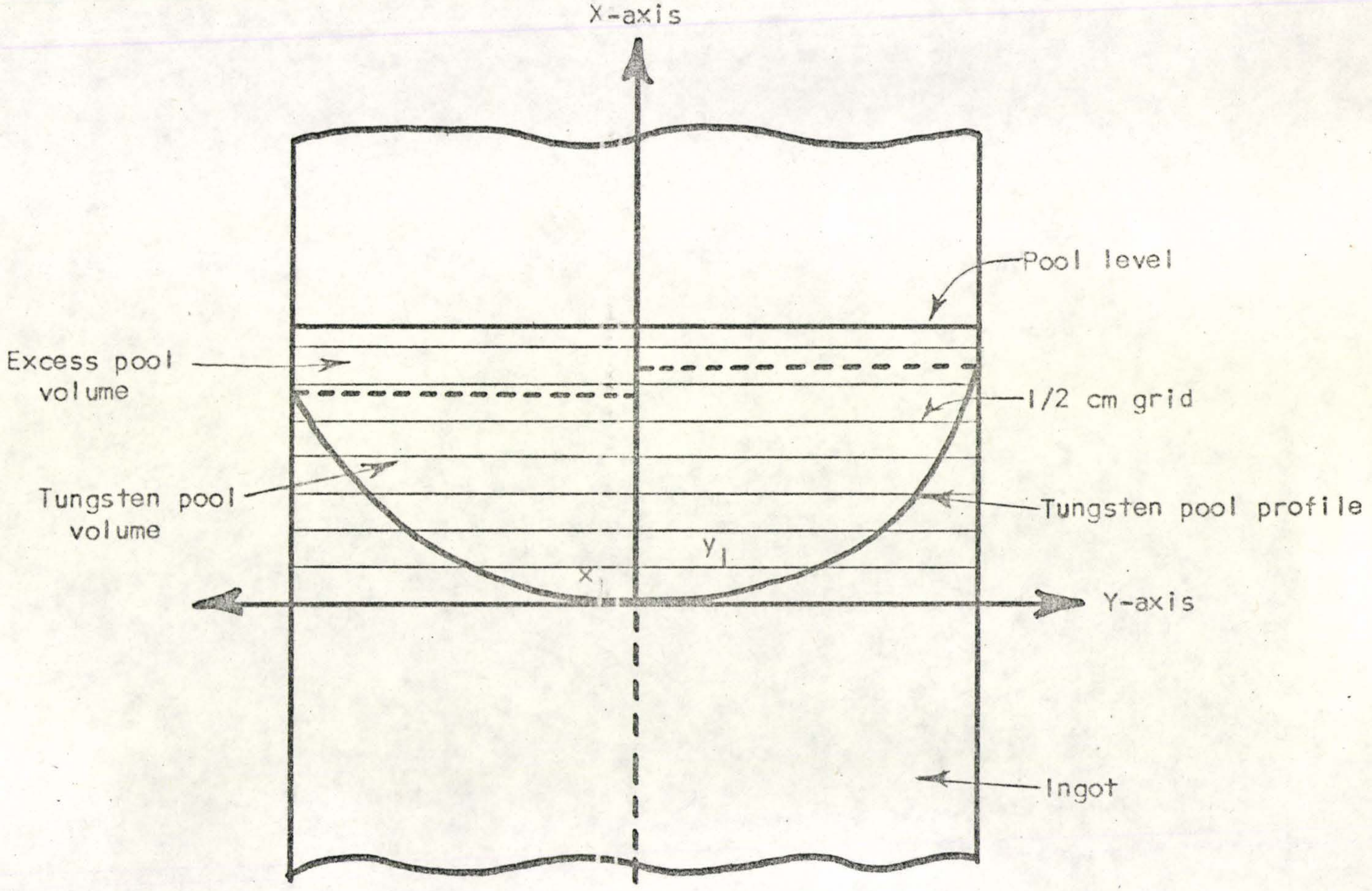

Figure 5.4 Mapping of tungsten pool profile.

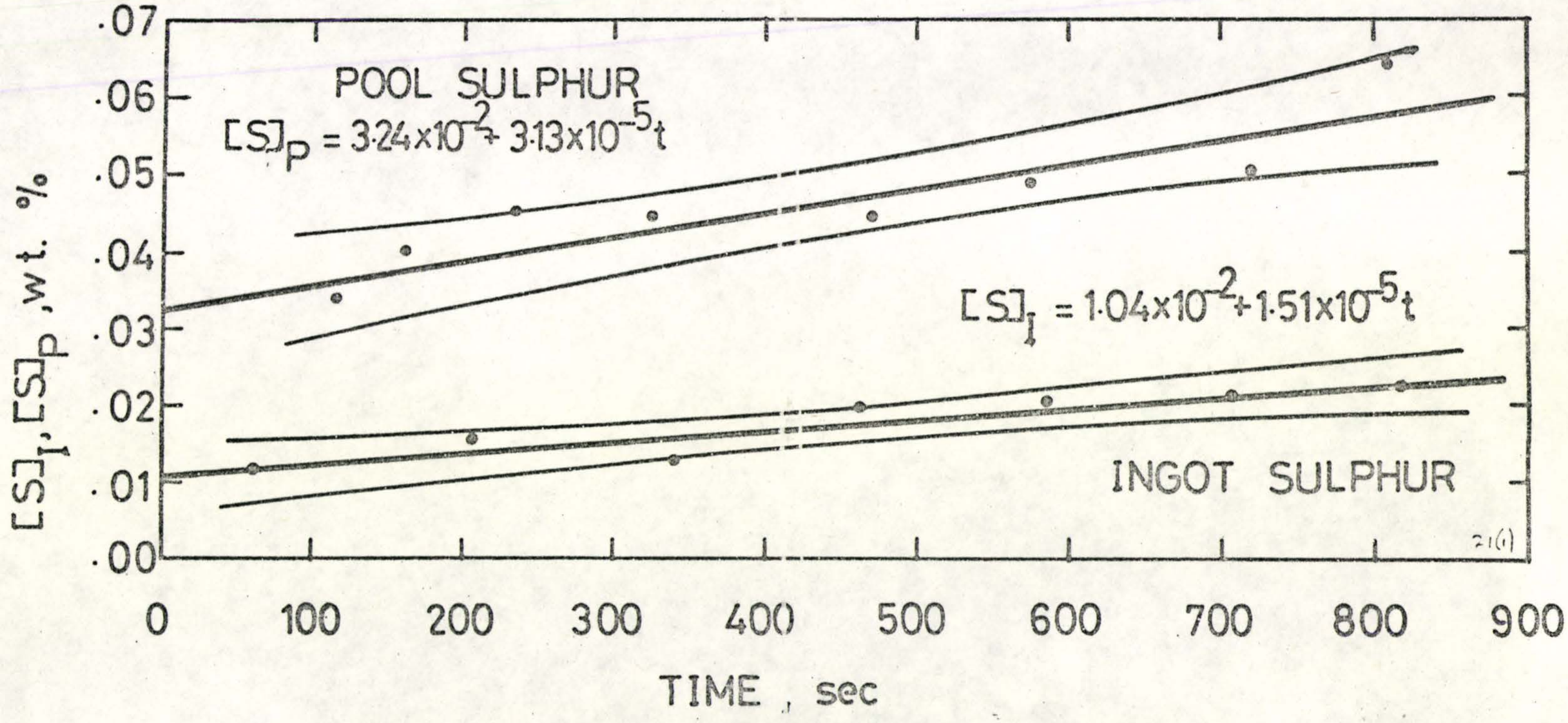

Figure 5.5 Pool and ingot sulphur content as a function of time, Melt 21.

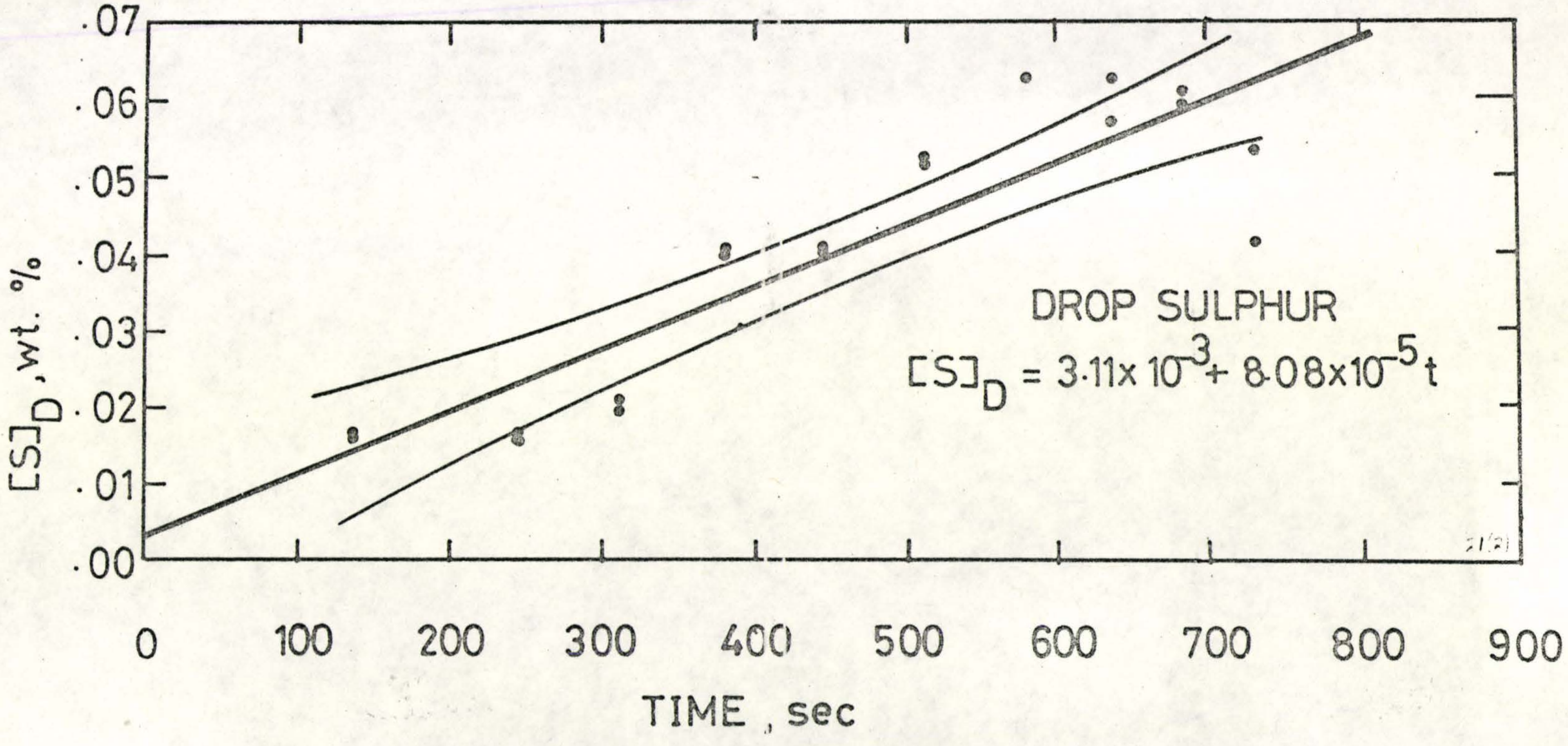

Figure 5.6 Droplet sulphur content as a function of time, Melt 21.

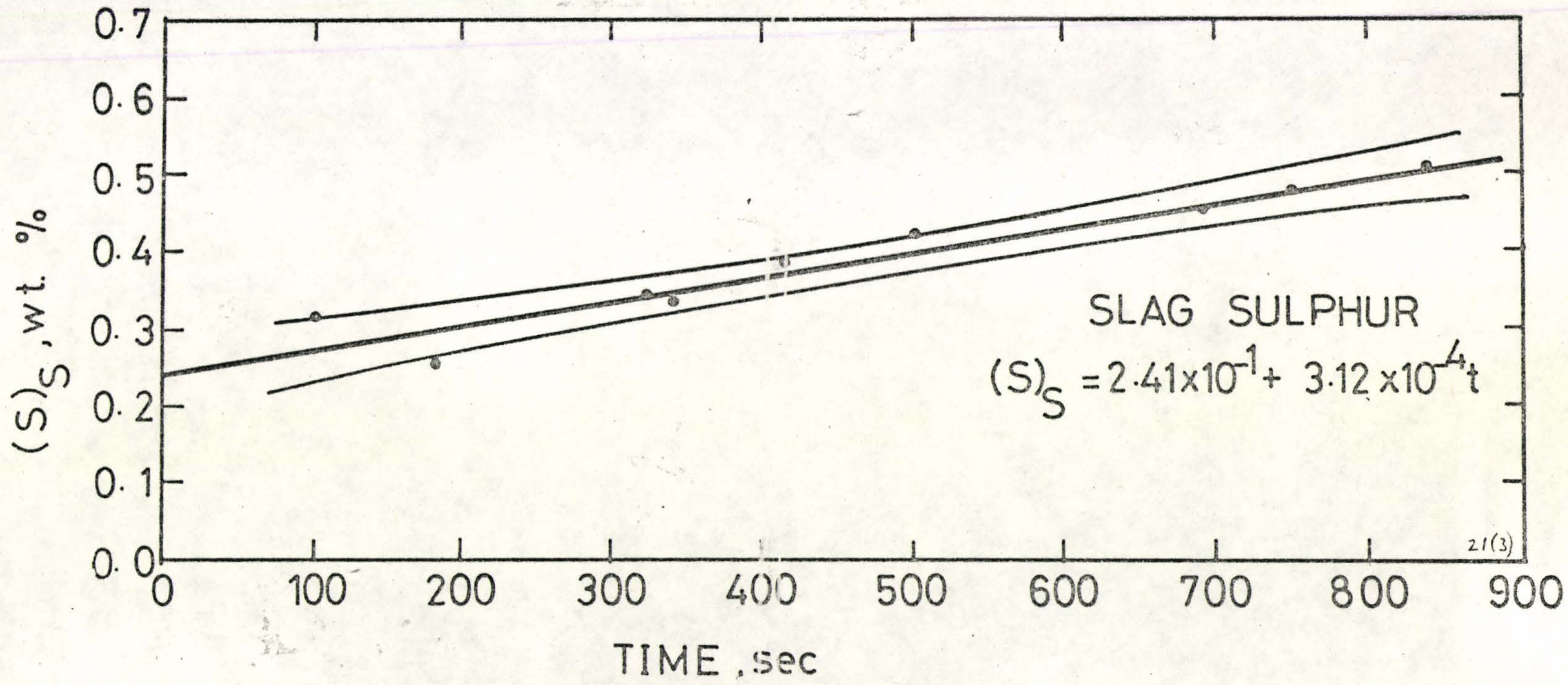

Figure 5.7 Slag sulphur content as a function of time, Melt 21.

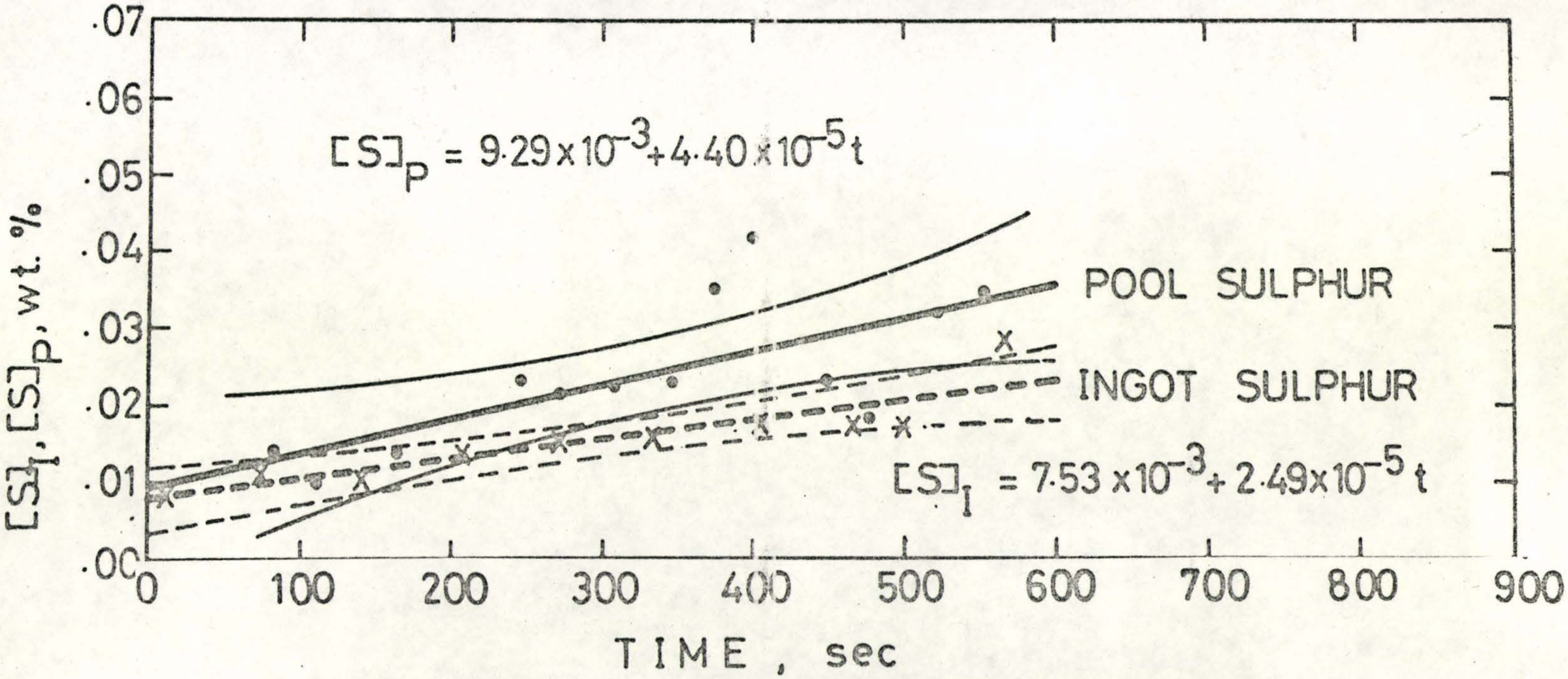

Figure 5.8 Pool and ingot sulphur content as a function of time, Melt 24.

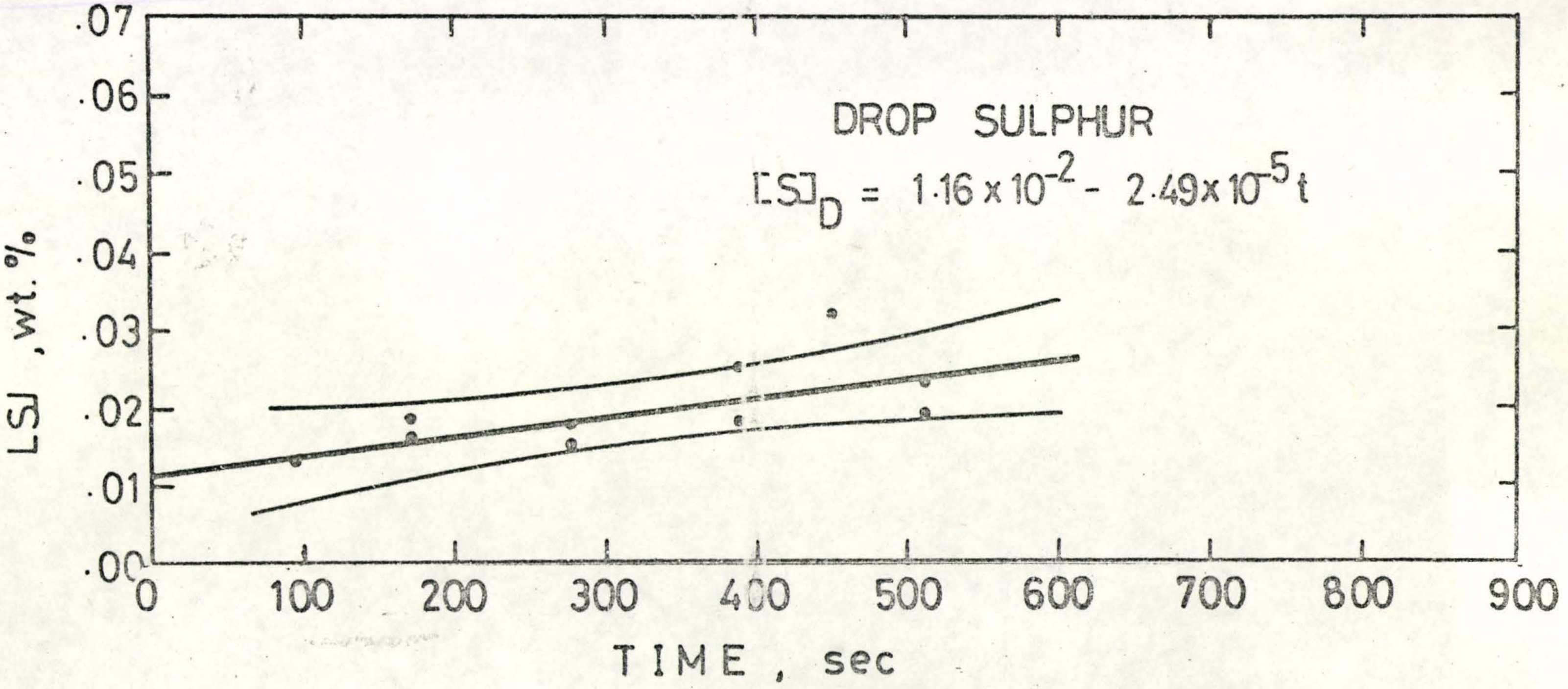

Figure 5.9 Droplet sulphur content as a function of time, Melt 24.

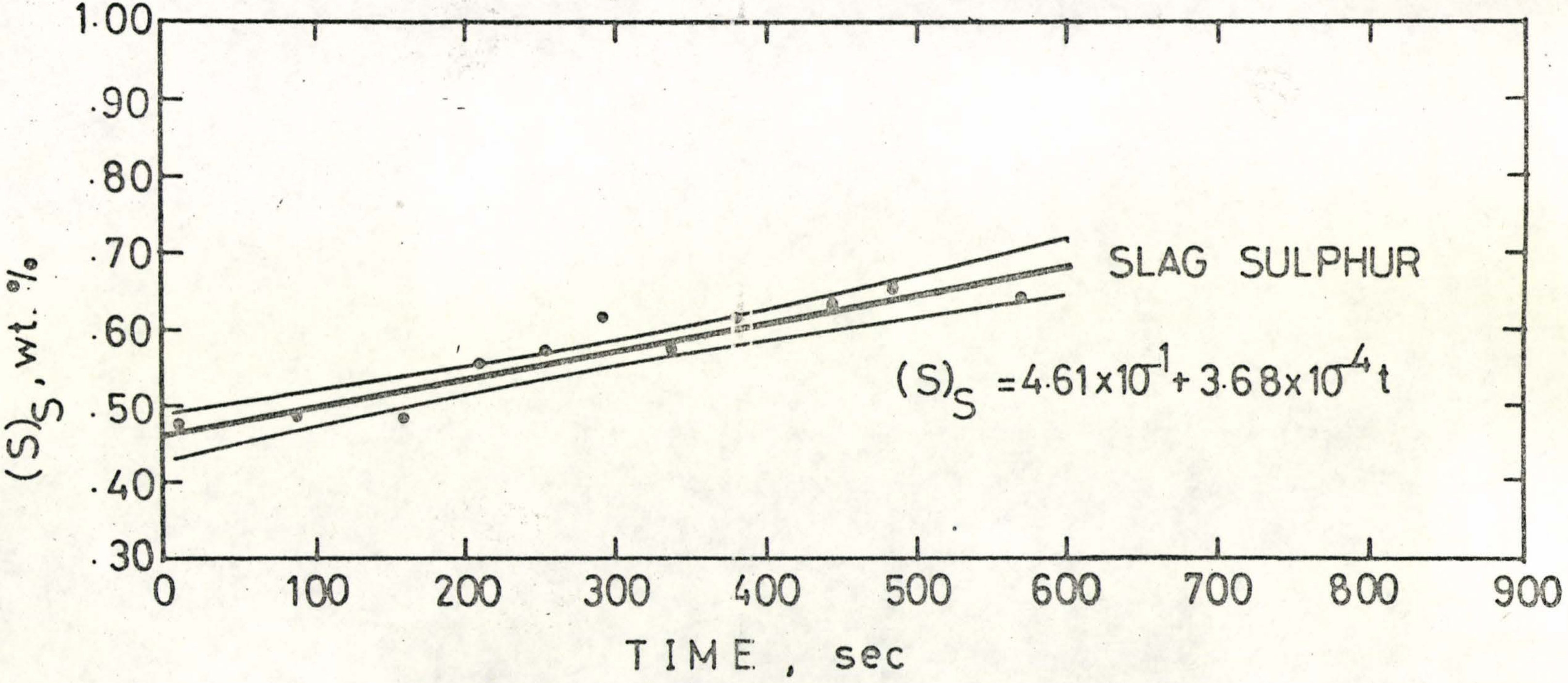

Figure 5.10 Slag sulphur content as a function of time, Melt 24.

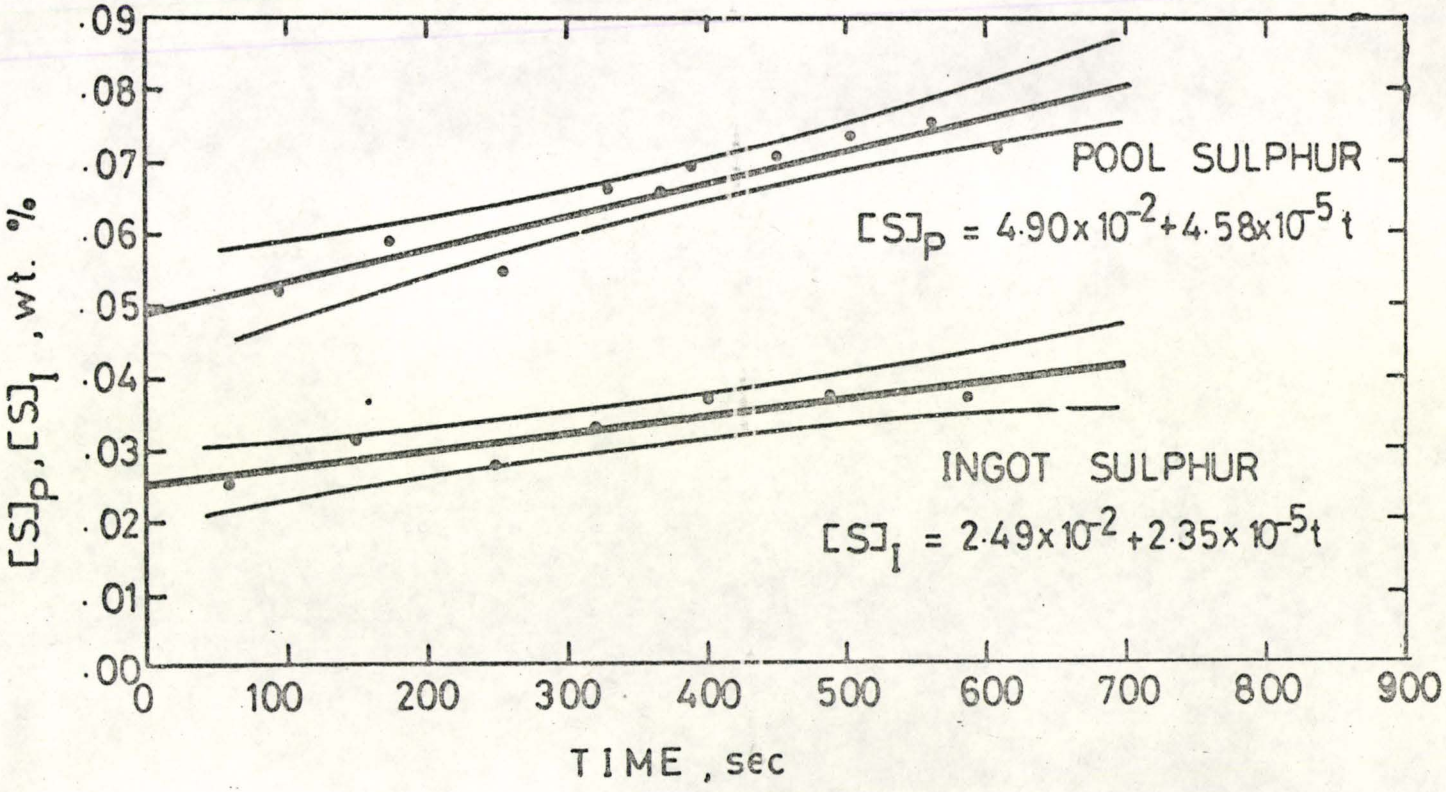

Figure 5.11 Pool and ingot sulphur content as a function of time, Melt 25.

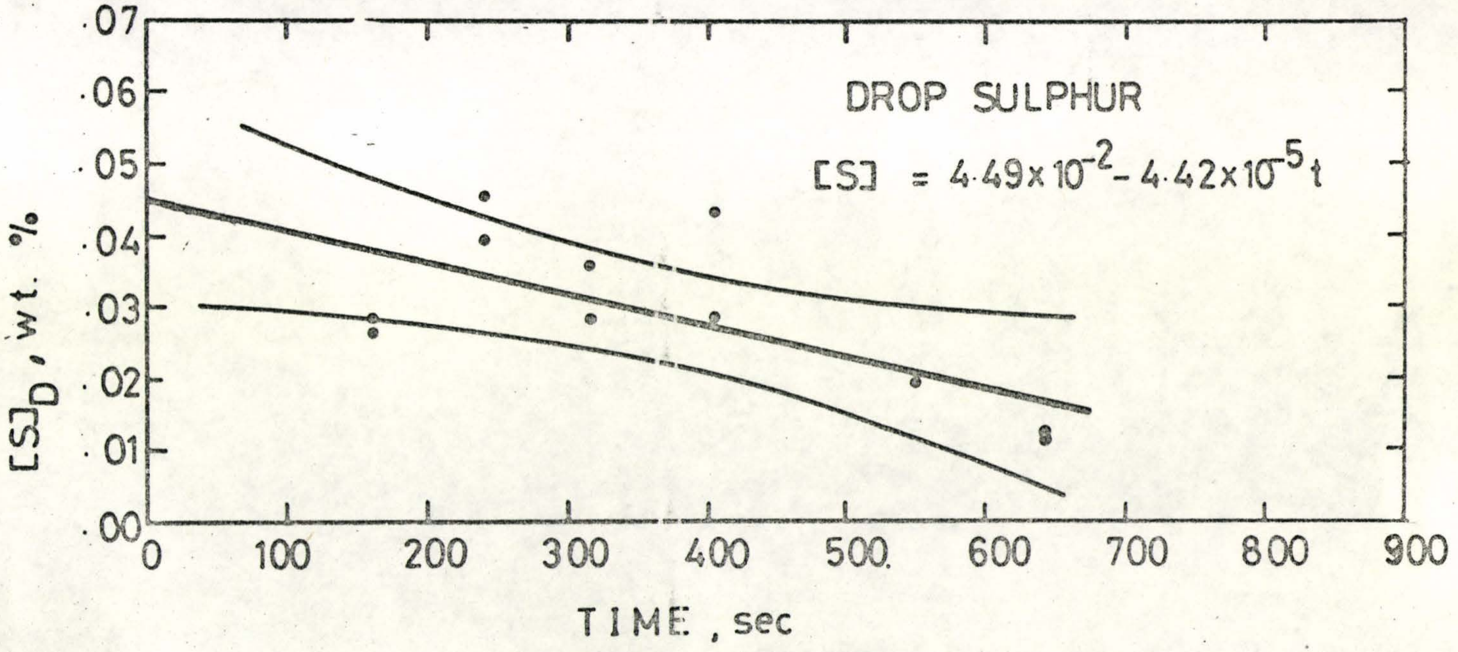

Figure 5.12 Drop sulphur content as a function of time, Melt 25.

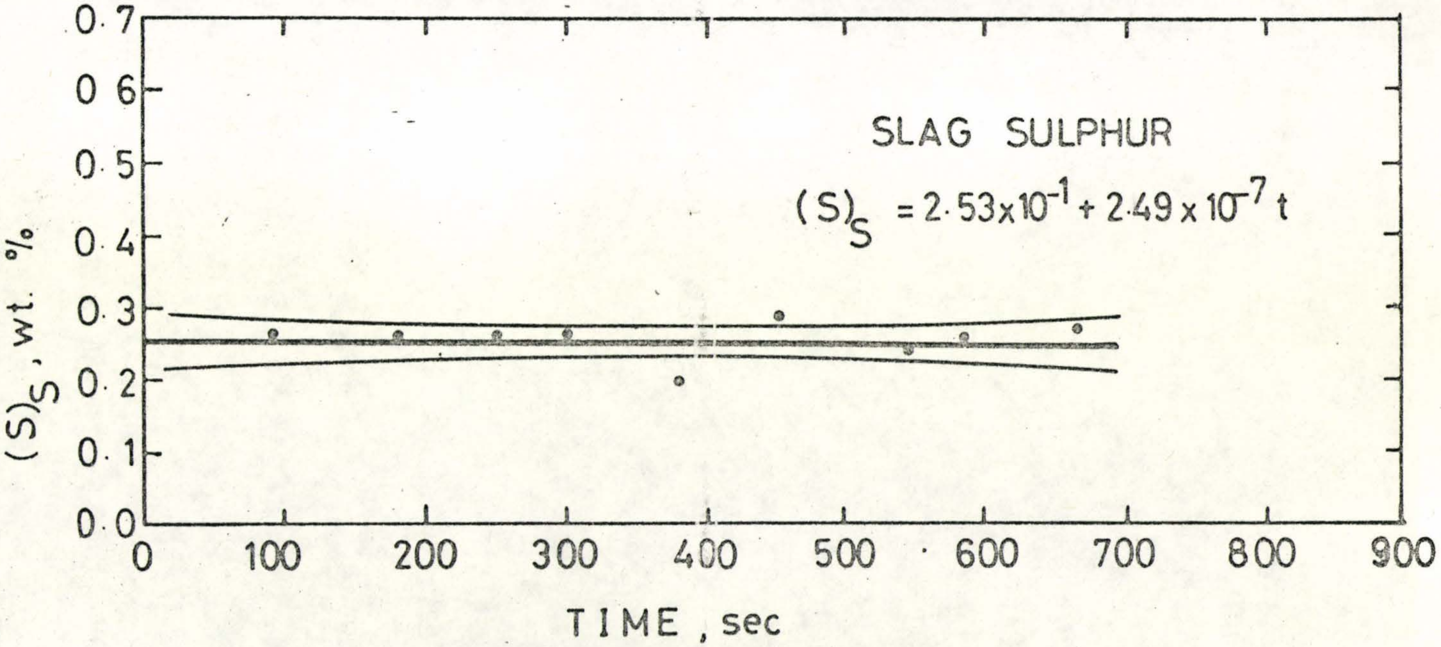

Figure 5.13 Slag sulphur content as a function of time, Melt 25.

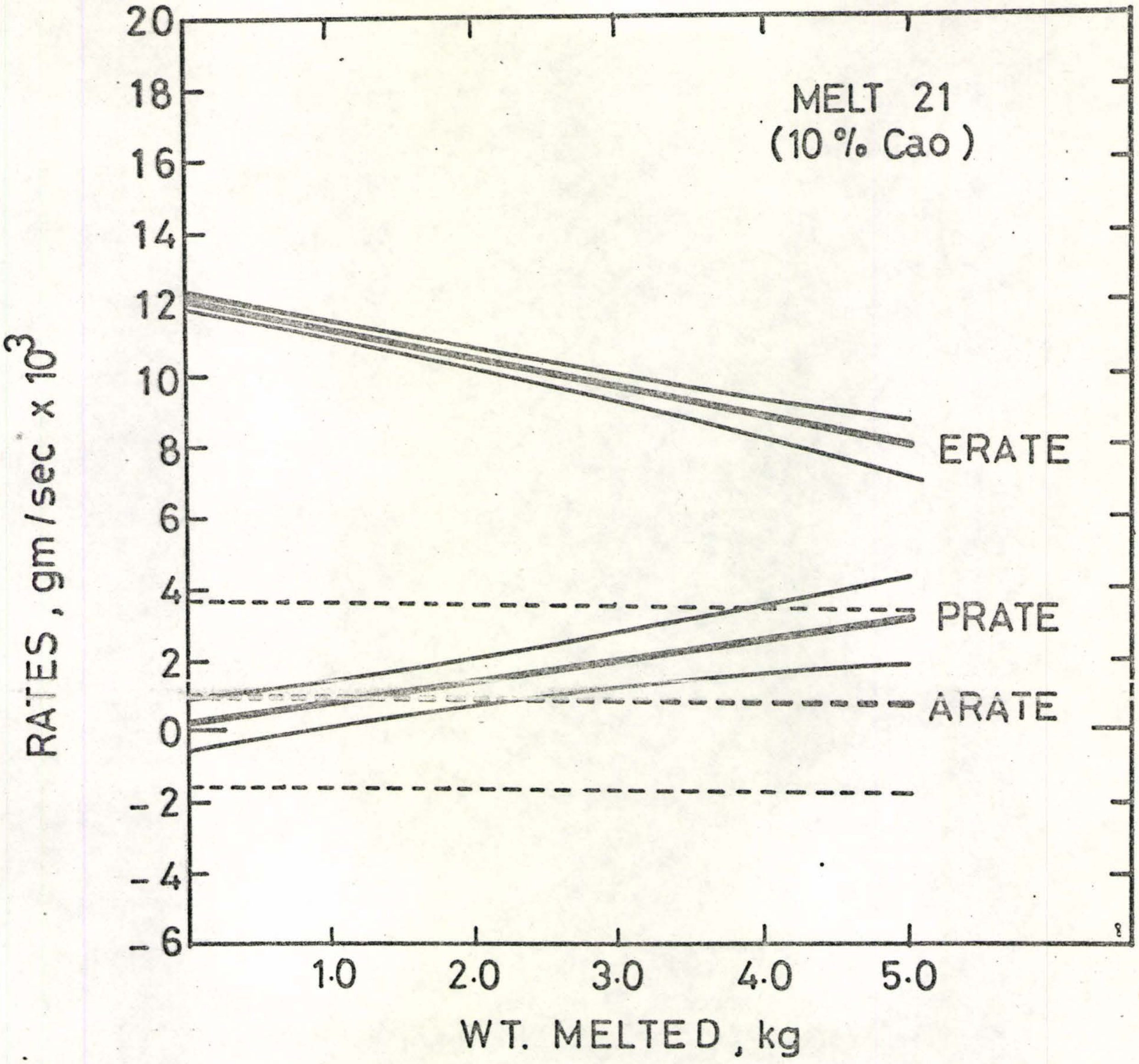

Figure 5.14 The three rates and their approximate 95% confidence intervals as a function of weight of electrode melted, Melt 21.

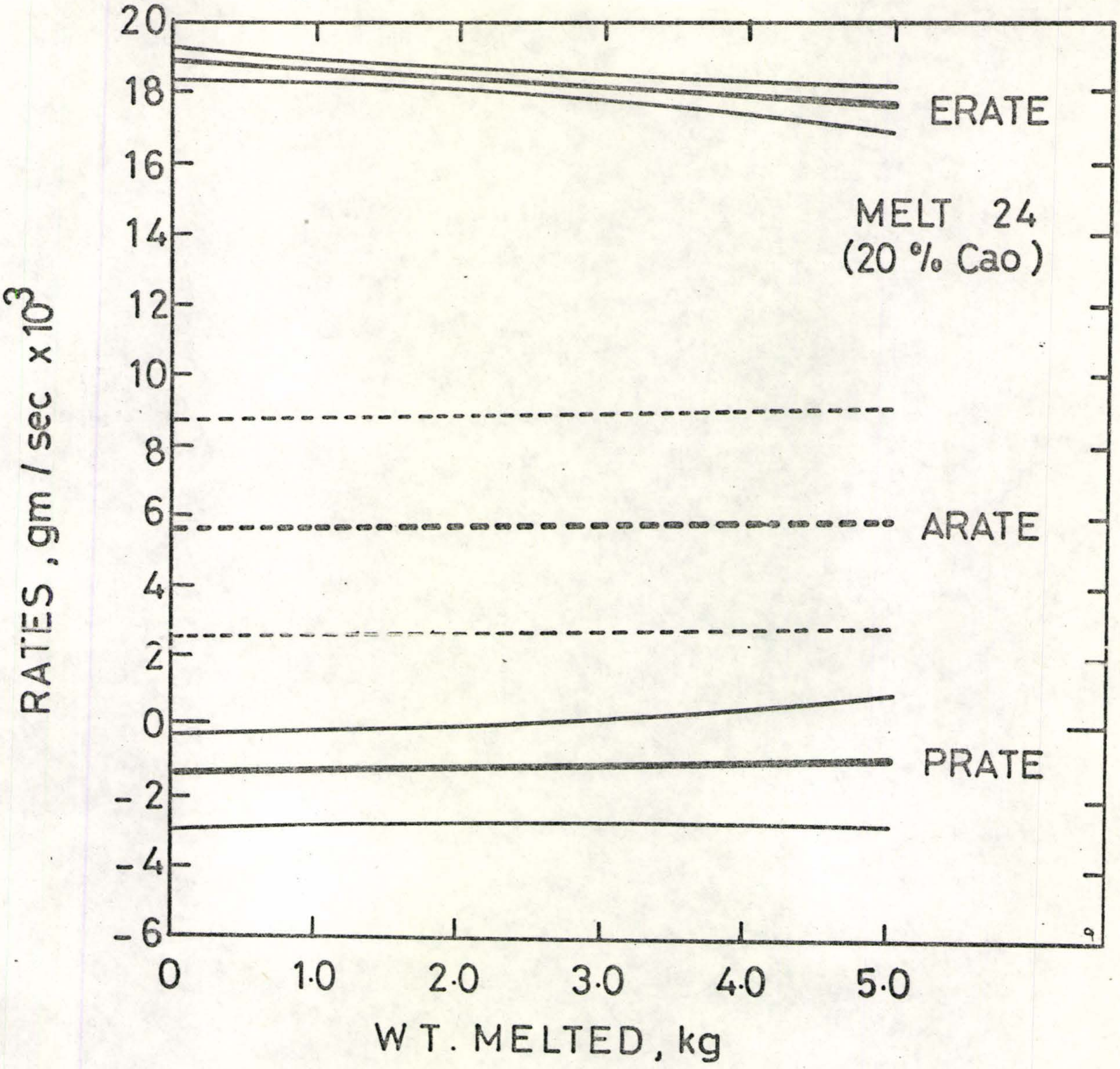

Figure 5.15 The three rates and their approximate 95% confidence intervals as a function of weight of electrode melted, Melt 24.

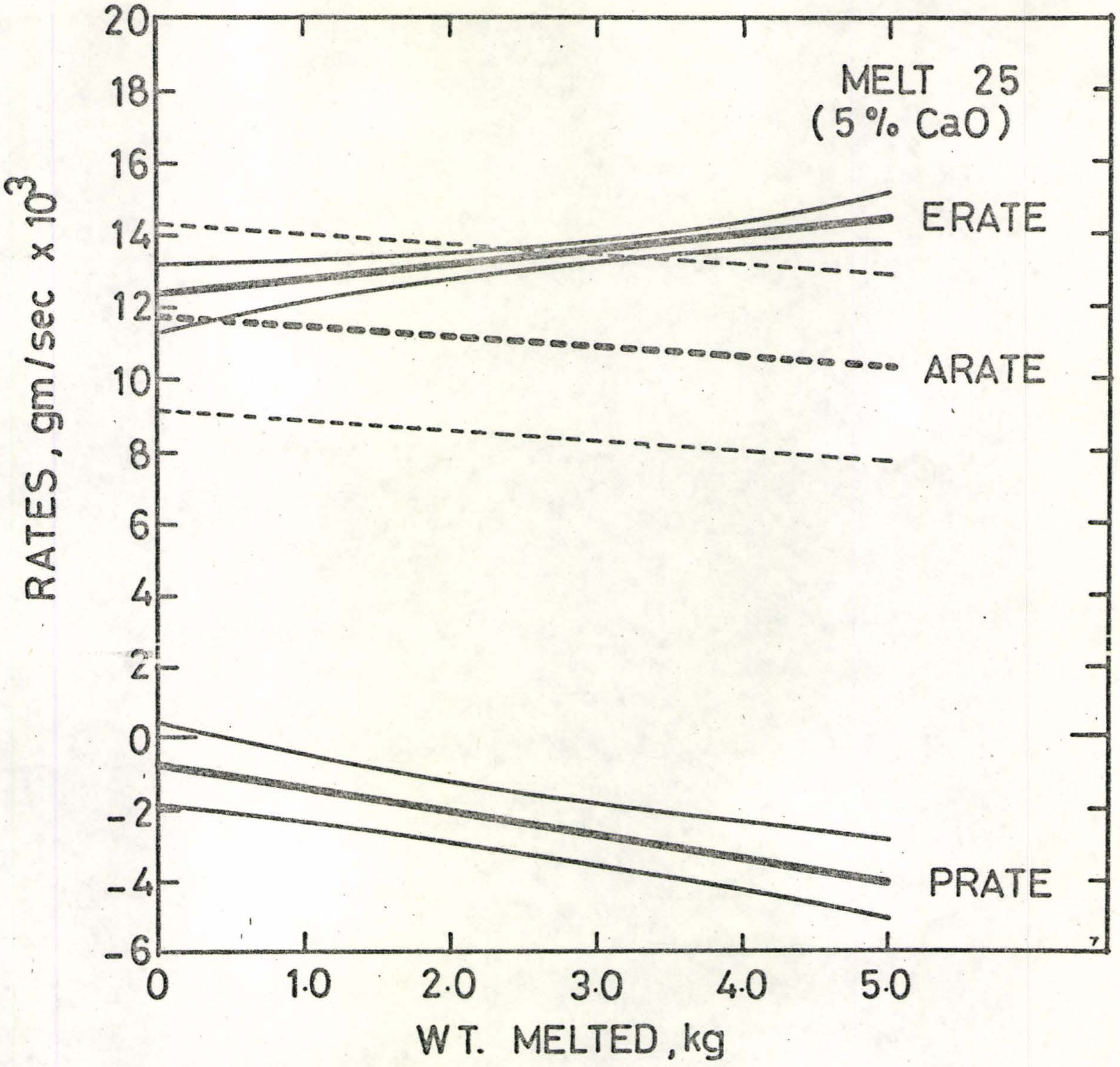

Figure 5.16 The three rates and their approximate 95% confidence intervals as a function of weight of electrode melted, Melt 25.

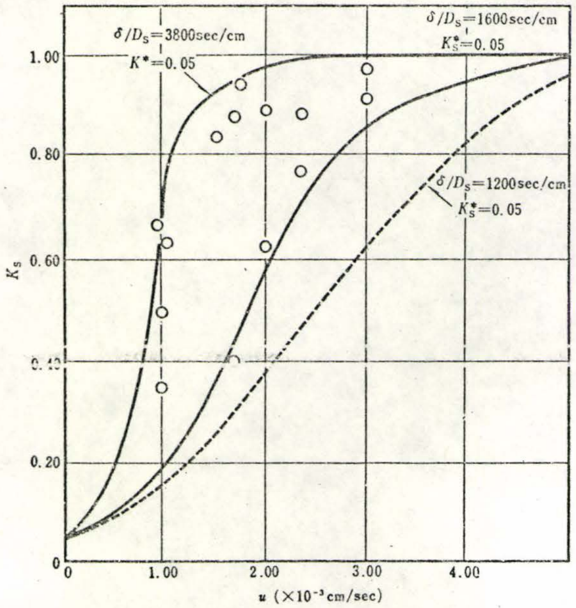

Figure 5.17 Relation between the effective distribution coefficient of sulphur and solidification rate (100).

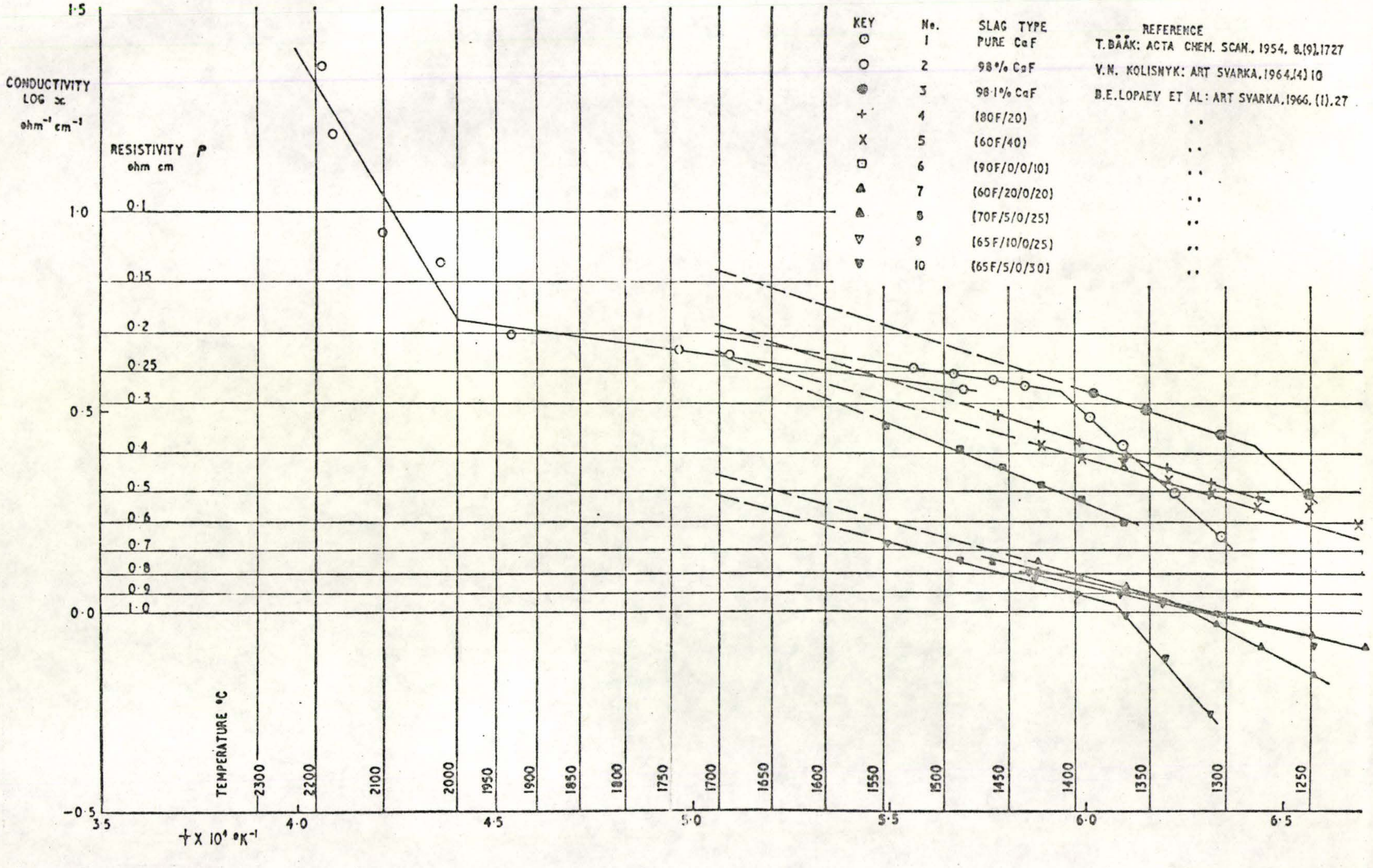

Figure 5.18 The electrical conductivity as a function of temperature of some CaF_2-based slags (13).